Ore Geology Reviews 57 (2014) 322–350

Contents lists available at ScienceDirect

Ore Geology Reviews

journal homepage: www.elsevier.com/locate/oregeorev

Petrography and geochemistry of the Shilu Fe–Co–Cu ore district, South China: Implications for the origin of a Neoproterozoic BIF system

D.R. Xu [a,*], Z.L. Wang [b], H.Y. Chen [a], Pete Hollings [c], Nicholas H. Jansen [d], Z.C. Zhang [e], C.J. Wu [a]

[a] Key Laboratory of Mineralogy and Metallogeny, Guangzhou Institute of Geochemistry, Chinese Academy of Sciences, Guangzhou 510301, China
[b] Key Laboratory of Metallogenic Prediction of Nonferrous Metals, Ministry of Education, School of Geosciences and Info-Physics, Central South University, Changsha 410083, China
[c] Department of Geology, Lakehead University, 955 Oliver Road, Thunder Bay, Ontario P7B 5E1, Canada
[d] ARC Centre of Excellence in Ore Deposit Research (CODES), University of Tasmania, TAS 7001, Australia
[e] State Key Laboratory of Geological Process and Mineral Resources, China University of Geosciences, Beijing 100083, China

ARTICLE INFO

Article history:
Received 27 March 2013
Received in revised form 16 August 2013
Accepted 16 August 2013
Available online 24 August 2013

Keywords:
Metamorphosed Neoproterozoic BIFs
Source areas
Restricted or sheltered marine basin near the rifted continental margin
Shilu Fe–Co–Cu ore district
Hainan Province
South China

ABSTRACT

The Shilu Fe–Co–Cu ore district is situated in the western Hainan Province of south China. This district consists of the upper Fe-rich layers and the lower Co–Cu ores, which are mainly hosted within the Neoproterozoic Shilu Group, a dominantly submarine siliciclastic and carbonate sedimentary succession that generally has been metamorphosed to greenschist facies. Three facies of metamorphosed BIFs, the oxide, the silicate–oxide and the sulfide–carbonate–silicate, have been identified within the Shilu Group. The oxide banded iron formation (BIF) facies (quartz itabirites or Fe-rich ores) consists of alternating hematite-rich and quartz-rich microbands. The silicate–oxide BIF facies (amphibolitic itabirites or Fe-poor ores) comprises alternating millimeter to tens of meter scale, magnetite–hematite-rich bands with calc-silicate-rich macro- to microbands. The sulfide–carbonate–silicate BIF facies (Co–Cu ores) contain alternating cobaltiferous pyrite, cobaltiferous pyrrhotite and chalcopyrite macrobands to microbands mainly with dolomite–calcite, but also with minor sericite–quartz bands. Blasto-oolitic, pelletoidal, colloidal, psammitic, and cryptocrystalline to microcrystalline textures, and blasto-bedding structures, which likely represent primary sedimentation, are often observed in the Shilu BIF facies.

The Shilu BIFs and interbedded host rocks are generally characterized by relatively low but variable $\sum$REE concentrations, LREE depletion and/or MREE enrichment relative to HREE, and no Ce, Gd and Eu anomalies to strongly positive Ce, Gd and Eu anomalies in the upward-convex PAAS-normalized REY patterns, except for both the banded or impure dolostones with nil Ce anomaly to negative Ce anomalies and negative La anomalies, and the minor sulfide–carbonate–silicate BIF facies with moderately negative Eu anomalies. They also contain relatively low but variable HFSE abundances as Zr, Nb, Hf, Th and Ti, and relatively high but variable abundances of Cu, Co, Ni, Pb, As, Mn and Ba. The consistently negative $\varepsilon_{Nd}(t)$ values range from −4.8 to −8.5, with a T_{DM} age of ca. 2.0 Ga. In line with the covariations between Al_2O_3 and TiO_2, Fe_2O_3 + FeO and SiO_2, Mn and Fe, Zr and Y/Ho and REE, and Sc and LREE, the geochemical and Sm–Nd isotopic features suggest that the precursors to the Shilu BIFs formed from a source dominated by seafloor-derived, high- to low temperature, acidic and reducing hydrothermal fluids but with variable input of detrital components in a seawater environment. Moreover, the involved detrital materials were sourced dominantly from an unknown, Paleoproterozoic or older crust, with lesser involvement from the Paleo- to Mesoproterozoic Baoban Group underlying the Shilu Group.

The Shilu BIFs of various facies are interpreted to have formed in a shallow marine, restricted or sheltered basin near the rifted continental margin most likely associated with the break-up of Rodinia as the result of mantle superplume activity in South China. The seafloor-derived, periodically upwelling metalliferous hydrothermal plume/vent fluids under anoxic but sulfidic to anoxic but Fe^{2+}-rich conditions were removed from the plume/vent and accumulated in the basin, and then variably mixed with terrigenous detrital components, which finally led to rhythmic deposition of the Shilu BIFs.

1. Introduction

Deposition of Precambrian banded iron formations (BIFs) began at 3.8 Ga (Isua, West Greenland), and largely disappeared from the geological record at ca. 1.8 Ga (Huston and Logan, 2004; Klein, 2005). After a billion year hiatus, BIFs reappeared in the Neoproterozoic between 0.85 and 0.6 Ga (Ilyin, 2009; Klein, 2005). The recurrence of the Neoproterozoic BIFs has been proposed to have a genetic link to either the Cryogenian–Ediacaran snowball-type global glaciations (Halverson et al., 2011; Hoffman et al., 1998; Hurtgen et al., 2002; Kirschvink, 1992; Klein, 2005; Le Heron et al., 2013; Stern et al., 2006; Young,

* Corresponding author. Tel.: +86 20 85292713.
E-mail address: xuderu@gig.ac.cn (D.R. Xu).

0169-1368/$ – see front matter © 2013 Elsevier B.V. All rights reserved.
http://dx.doi.org/10.1016/j.oregeorev.2013.08.011

2002) and/or to the ca. ≥825 Ma Rodinia breakup (Bekker et al., 2010; Johnston et al., 2010; Och and Shields-Zhou, 2012; Yeo, 1981). Consequently, the Neoproterozoic BIFs are subdivided into Algoma- and Rapitan types (cf. Basta et al., 2011), in which the former are found in Yangtze of China (Tang et al., 1987; Zhang et al., 2011), Um Anab and Wadi Karim of Egypt (Basta et al., 2011; Khalil and El-Shazly, 2012), and Sawawin of Arabia (Mukherjee, 2008) and are associated with volcanic activity due to the Rodinia break-up and show no direct evidence of forming in response to glaciation. In contrast, the predominant Rapitan type are exemplified by those in Rapitan of Canada (Klein and Beukes, 1993), Urucum of Brazil (Babinski et al., 2013; Klein and Ladeira, 2004), Adelaide of Australia (Lottermoser and Ashley, 2000) and Yerbal of Uruguay (Pecoits et al., 2008), and are typically of glaciogenic association and can be connected with snowball Earth condition (Hoffman and Schrag, 2002; Hoffman et al., 1998; Kirschvink, 1992) or glaciated rift environments (Young, 2002). The distinct differences in abundance, distribution and geochemical and isotopic features among Algoma-, Superior- and Rapitan-type BIFs (Basta et al., 2011; Gross, 1980) result from different genetic processes and sources of their constituents (Beukes and Gutzmer, 2008; Huston and Logan, 2004; James, 1992; Klein, 2005; Klemm, 2000; Pecoits et al., 2009).

BIFs have long been considered as chemical sediments formed by precipitation of Fe and Si from mixing solutions of seawater with hydrothermal fluids (Gross, 1980; James, 1954; Klein, 2005; Trendall, 1983). The origin of Fe and Si in BIFs, however, has been the subject of a long-standing debate. The controversies mainly point to continental or hydrothermal sources or some combination thereof (Adekoya, 1998; Alibert and McCulloch, 1993; Arora et al., 1995; Dymek and Klein, 1988; Frei and Polat, 2007; Hamade et al., 2003; Holland, 1973; Kimberley, 1989; Morris and Horwitz, 1983; Pecoits et al., 2009; Simonson, 1985). Mantle superplume volcanism related to rifting was thought to enhance BIF deposition by increasing the iron flux to the global oceans through continental weathering and/or submarine hydrothermal process (Isley and Abbott, 1999). Trace element and isotopic data (C, O, S, Nd, etc.) especially rare earth element plus yttrium (REE + Y), from marine precipitates, including the Precambrian BIFs, have been proven to be powerful monitors that not only provide valuable insight into the composition of coeval seawater and the evolution of the terrestrial atmosphere–hydrosphere–biosphere–lithosphere system but also offer reliable lines of evidence to reveal the origin, depositional environment, and genesis of the Precambrian BIFs (Anbar, 2008; Bau and Dulski, 1996; Bolhar et al., 2004; Frimmel, 2009; Halverson et al., 2010; Hurtgen et al., 2002; Planavsky et al., 2010), mainly with respect to the input ratios of submarine hydrothermal fluids versus erosional fluxes (Derry and Jacobsen, 1988). This is largely because the different types of BIF-precipitating water masses, such as submarine hydrothermal fluids, seawaters and river waters have systematic differences in the chemical properties of REE + Y (Bolhar and Van Kranendonk, 2007; Bolhar et al., 2004; Derry and Jacobsen, 1990; Elderfield et al., 1990; Nozaki et al., 1997). Minor amounts of crustal material, when incorporated into marine precipitates, will also affect the primary major and trace element, REE and isotopic signatures, as recorded by elevated $\sum$REE contents, elevated and correlated abundances of incompatible elements (Th, Hf, Zr, Sc, etc.), lower $\varepsilon_{Nd}(t)$ values than coeval detritus-free equivalents, depressed seawater-like Y/Ho ratios, and co-variations of Al_2O_3 vs. TiO_2, Zr vs. TiO_2, Zr vs. REE, Th vs. Al_2O_3, Zr vs. Y/Ho, and Y/Ho vs. Ce/Ce* (in modern seawater proxies) (e.g., Alibert and McCulloch, 1993; Arora et al., 1995; Bolhar and Van Kranendonk, 2007; Bolhar et al., 2004; Derry and Jacobsen, 1988, 1990; Dymek and Klein, 1988; Ewers and Morris, 1981; Frimmel, 2009; Jacobsen and Pimentel-Klose, 1988a, 1988b; Manikyamba et al., 1993; Miller and O'Nions, 1985).

The Shilu Fe–Co–Cu ore district, one of the most renowned Fe-ore districts in China, is located in Changjiang County, western Hainan Province

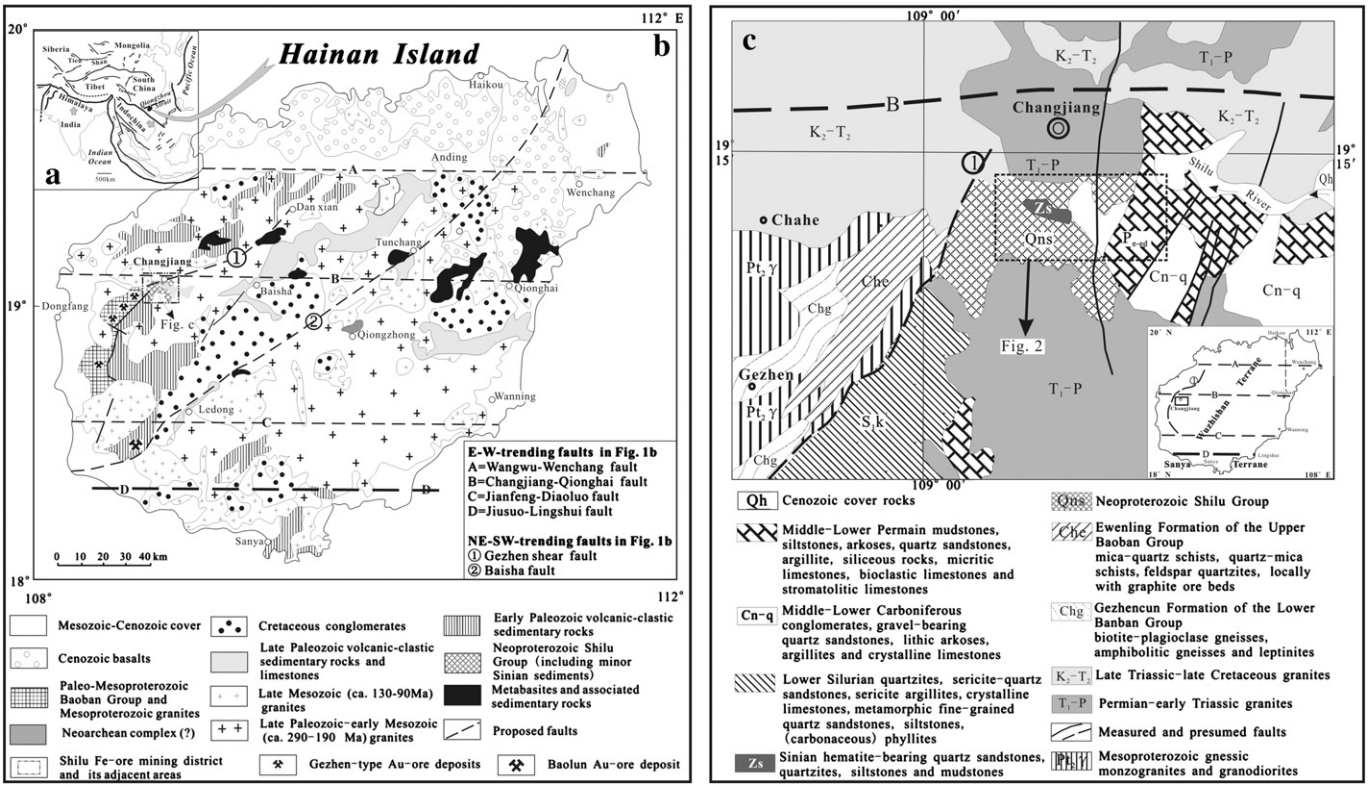

Fig. 1. (a) Location map, (b) simplified map showing the main tectono-stratigraphic and tectono-magmatic units, and ore deposits in Hainan Island, south China, and (c) sketch map showing regional geology of the Shilu Fe–Co–Cu ore district and its peripheral areas in the western Hainan Island, south China. Symbols A, B, C and D, and ① in (c) can be found in (b). The dashed square box inserted in (c) shows the location of the Shilu ore district and its peripheral areas for Fig. 2a.
Panel a is modified from Tapponnier et al. (1990). Panel b is modified from Xu et al. (2009). Panel c is modified from Xu et al. (2013).

(Fig. 1). The Fe- and Co–Cu ores are mainly hosted within a dominantly submarine siliciclastic and carbonate sedimentary succession of the Neoproterozoic Shilu Group that mostly has been metamorphosed to greenschist facies (SCISTCAS, 1986; Xu et al., 2009, 2013; Yao et al., 1999). Besides the main host rocks of the Neoproterozoic Shilu Group, the Shilu ore district is endowed with several characteristic features (Xu et al., 2013), including (1) the largest hematite-rich Fe-ore district in China, with proven Fe-ore reserves of more than 500 Mt, (2) the Fe–Co–Cu metal association with Co–Cu ore layers generally occurring about 30–60 m below the Fe-ore horizons, and (3) the high average grades of 51% for FeO, 0.29% for Co metal, and 1.18% Cu for metal, with 7% of the proven metal Co reserves in China (Feng et al., 2004). Most previous work concentrated on the origin of iron (Fang et al., 1992; Hong et al., 1981; SCISTCAS, 1986; Wang et al., 1978; Yu and Lu, 1983), which finally led to an interpretation of the Shilu district as a sedimentary–metamorphic ore deposit-type, i.e. Lake Superior BIF-type (Xu et al., 2013). However, the origin, lithofacies, primary depositional settings, and genesis of the Shilu BIFs remain unclear. In addition, the earlier genetic models (Hong et al., 1981; SCISTCAS, 1986; Wang, 1985; Xu et al., 2013; Zhao et al., 2008) did not address the Co and Cu mineralization and their relationship to Fe metallogenesis. This is partly the consequence of lack of access to the Co–Cu ores due to the lack of development and mining. In this paper, a petrographic study, and complementary major and trace element (including REE + Y), and Sm–Nd isotope analyses, have been carried out on the Shilu ore district, in order to further identify the facies type of the Shilu BIFs and the source of the ore elements Fe, Si, Co and Cu. Based on these results, we tentatively propose a primary basinal setting for the deposition of such Neoproterozoic BIFs and interbedded host rocks.

2. A summary on regional and ore deposit geologies

The Province of Hainan, an epicontinental island in the north of the South China Sea, is separated from South China mainland by the Qiongzhou Strait (Fig. 1a). It lies at the junction of Eurasian, Pacific and Indian–Australian plates, and thus displays a complex tectonic history with multistage and multiple magmatism, metamorphism and metallogenetic events (Xu et al., 2013). Details of the structural assembly, stratigraphy, magmatism, metamorphism, and metallogeny are found elsewhere (HBGMR, 1997; Li et al., 2002a, 2002b, 2006a, 2008; Ma et al., 1997; Metcalfe et al., 1994; Wang, 1986; Wang et al., 1991, 2013; Xu et al., 2001a, 2007a, 2009, 2013; Zeng et al., 1992; Zhang et al., 1997).

The Shilu Fe–Co–Cu ore district is situated in the western Hainan Province and regionally controlled by both the approximately E-trending Changjiang–Qionghai crustal fault zone and the NE-trending Gezhen brittle–ductile shear zone (Fig. 1b, c). The outcropping strata in the Shilu district chiefly comprise the Neoproterozoic (ca. 1.0–0.83 Ga; Xu et al., 2013) Shilu Group and overlying Sinian (Late Neoproterozoic) Shihuiding Formation (Fig. 2a). The Carboniferous to Permian clastic and carbonate sedimentary rocks that have been metamorphosed to greenschist facies occur in the eastern part of the district (Figs. 1c and 2a). The Fe- and Co–Cu ores are mainly hosted within the Shilu Group, a dominantly submarine siliciclastic and carbonate sedimentary succession, and to a lesser extent in the Shihuiding Formation. The latter unconformably overlies the Shilu Group and includes a suite of low-grade terrigenous clastic sedimentary rocks including quartzose sandstones and siltstones, quartzites and phyllites, locally containing thin Fe–Mn ore beds (Fig. 3). The Shilu Group, which has been affected by

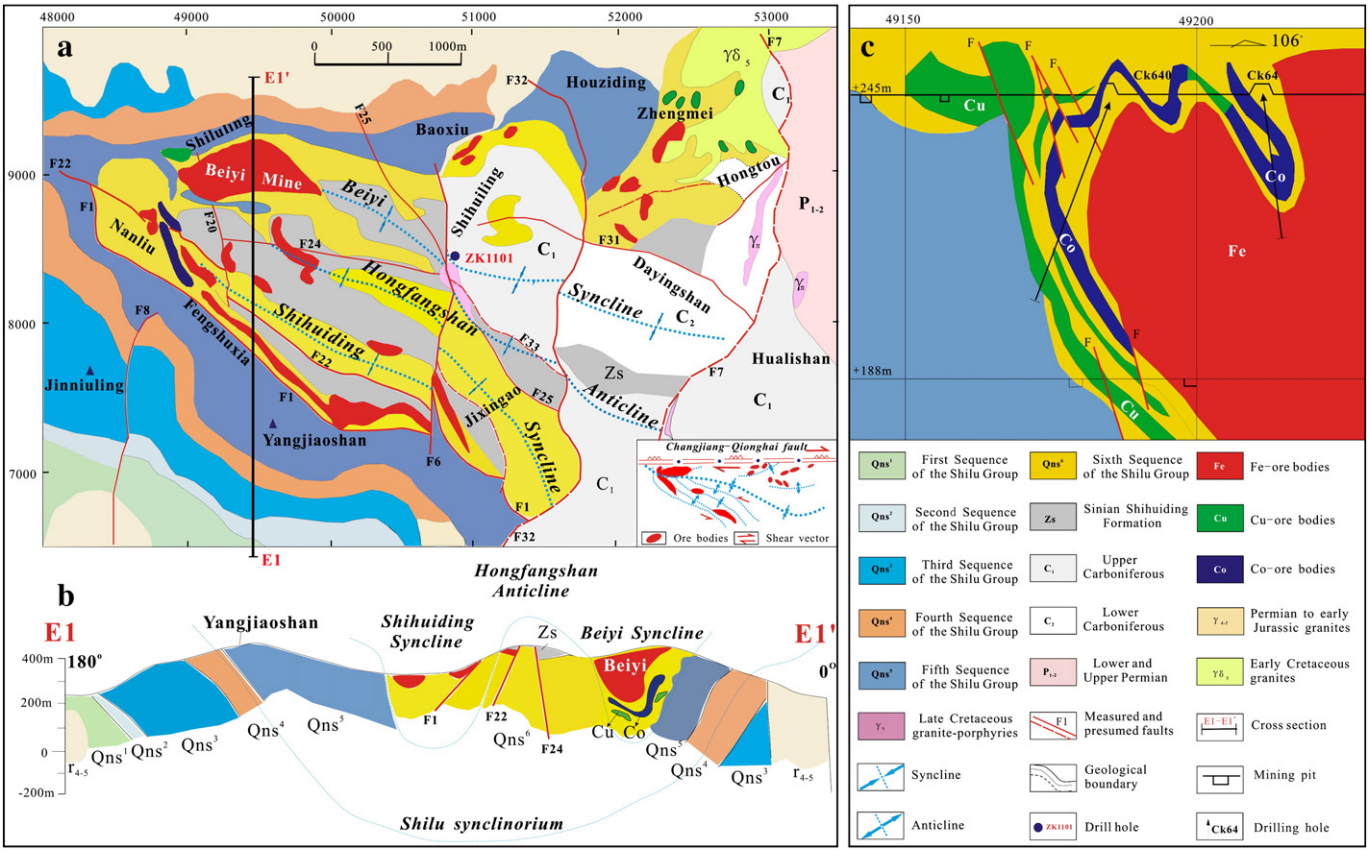

Fig. 2. Sketch map (a), enclosed by the section E1–E1′ (b) across the NW–SE trending synclinorium and the locally vertical section (c) at the Beiyi mine, showing structural styles, ore morphologies and spatial relationship between Fe- and Co–Cu orebodies in the Shilu Fe–Co–Cu ore district. Panel c also indicates that all the Fe-, Co- and Cu orebodies are characterized by strong folding but are parallel to each other.

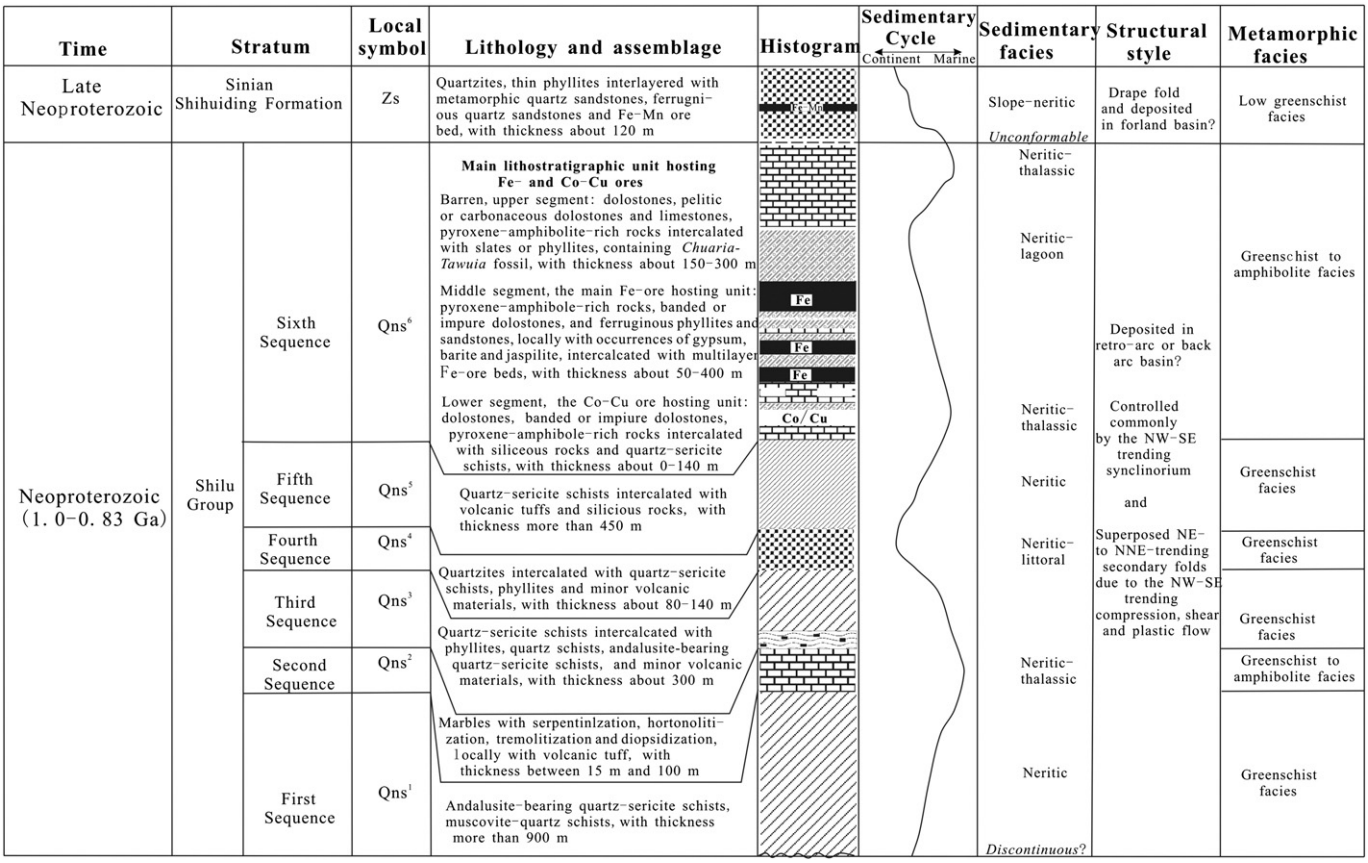

Fig. 3. Synthetically stratigraphical histogram of the Shilu Group in the Fe–Co–Cu ore district, western Hainan Island of South China. Modified from Xu et al. (2013).

greenschist facies (locally up to amphibolite facies) metamorphism, is further divided into six lithostratigraphic sequences from bottom to top, based on lithologies, textures and hosted ore-types (Figs. 2 and 3). The first, third, fourth and fifth sequences consist predominantly of quartz–mica schists, quartzites and phyllites. The second sequence comprises crystallized dolostones locally with skarn mineral assemblages. The sixth sequence is the main Fe-, and Co–Cu-bearing rock system and can be subdivided into three segments. The barren, upper segment consists of dolomitic and argillaceous limestones intercalated with carbonaceous phyllites, dolostones and minor banded or impure dolostones; the middle segment, with at least three Fe-bearing layers, comprises pyroxene–amphibole-rich rocks and banded or impure dolostones, and minor ferruginous phyllites and sandstones. Locally, tuffaceous rocks, barite, anhydrite, and jaspilite also occur in this segment. The lower Co–Cu-bearing segment consists of banded or impure dolostones, dolostones and pyroxene–amphibole-rich rocks intercalated with phyllites. As a result, the Co–Cu ore beds generally are located about 30–60 m below the Fe-ore horizons (Figs. 2b, c and 3).

Structural deformation, including folding and associated ductile to brittle shearing, affects both the Fe- and Co–Cu ores, and the interbedded host rocks. At least two stages of structural deformation and associated metamorphism have been recognized (Xu et al., 2013): D_1-deformation produced a NW-trending synclinorium with associated regional S_1 foliation, whereas the overprinting D_2 deformation resulted in various amounts of folding, faulting and mineral recrystallization. Stratiform Fe- and Co–Cu ores are located on the trough and/or along the transitional section from limbs to troughs of the NW-trending synclinorium (Fig. 2b). Skarnization, propylitization, carbonatization and related sulfide mineralization are also present in the district and most likely are linked to the Permian to Early Jurassic and Cretaceous granites and dikes (Fig. 2). These deformational, metamorphic and hydrothermal alteration events might have reworked or re-enriched the Shilu Fe- and Co–Cu ores (Xu et al., 2013).

3. Petrography and mineralogy of the quartz itabirites and Co–Cu ores

The pyroxene–amphibole-rich rocks and banded or impure dolostones in the sixth sequence of the Shilu Group are the main host rocks to the Fe- and the Co–Cu ores, respectively (Fig. 3). The Fe-ores comprise two types: the quartz itabirites (i.e. the Fe-rich ores) and the amphibolitic itabirites (i.e. the Fe-poor ores). The amphibolitic itabirites and interbedded host rocks, i.e. the pyroxene–amphibole-rich rocks and banded or impure dolostones, previously have been described by Xu et al. (2013). Herein, we will give a detailed description of the petrographical and mineralogical features of the quartz itabirites and Co–Cu ores.

Quartz itabirites are the main type of Fe-ores in the Shilu district. Mineralogically, they are dominated by hematite and quartz with minor magnetite, barite, garnet and anhydrite, and display lepidoblastic, porphyroblastic, blastopsammitic and blastooolitic textures, and banding, laminated or blastobedding, and augen structures. The quartz crystals with blastopsammitic-texture are weakly oriented, subround to subangular, and unequal grains ranging from 5 μm to 0.2 mm, and often comprise alternating bands with Fe oxide (hematite, magnetite)-rich bands (Fig. 4a, b). This type of itabirite is also characterized by colloform texture reflected by colloidal Fe-oxides as adherent coatings on the gelatinous quartz particles (Fig. 4c). Possibly they represent a primary colloidal precipitates with minor involvement of the detrital constituents (Lascelles, 2007). In deformed quartz itabirites, however, the coarser-grained quartz grains ranging from 50 μm to 0.2 mm generally occur as σ-type porphyroblasts or have elongated lentoid shapes which

indicate a sinistral-shear sense, and are surrounded by oriented, microplaty hematite crystals (Fig. 4d). In the stronger deformed quartz itabirites, the crystalloblastic quartz with undulatory extinction presents an elongated lentoid shape and is oriented parallel to the regionally S_1 schistosity (Fig. 4e). As a result, the quartz aggregation generally expresses "W-type" fold, pinch-and-swell

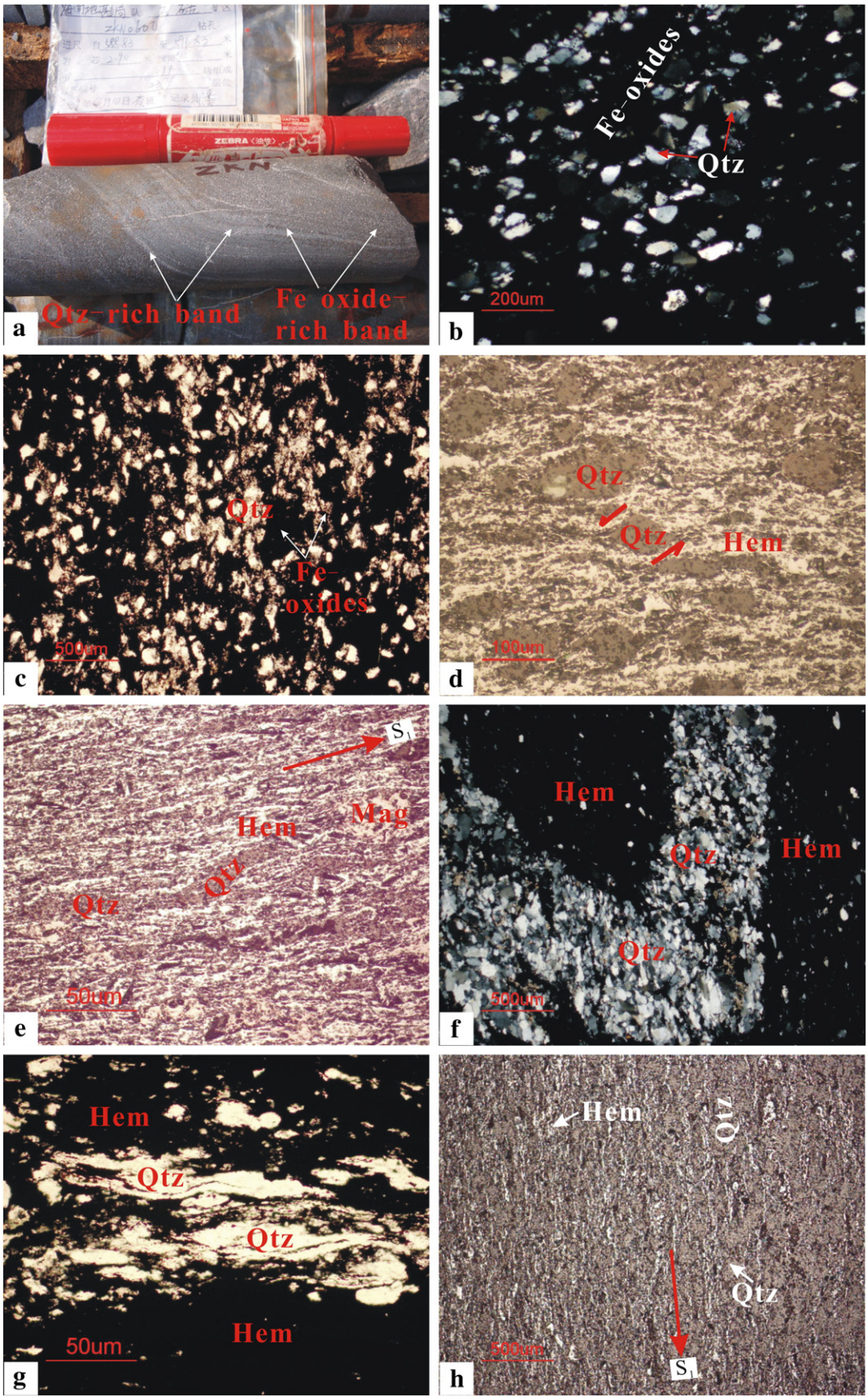

boudinage, rootless hooked-fold, stretching lineation and "fish-like" quartz (Fig. 4f, g). Hematite grains in the quartz itabirites typically occur as microplaty crystals with lengths of ≤1 μm to 0.25 mm and widths of ≤1 μm to 50 μm, and exhibit an obvious orientation to S_1 foliation (Fig. 4h). These microplaty hematite crystals also occur as deformed penniform or pisolitic matrixes surrounding magnetite grains (Fig. 5a, b). Significantly, the magnetite crystals that coexist with hematite grains, generally display oxidized to trellis- or interlocking texture martites (Fig. 5c, d). In turn, these ~0.1–0.7 mm magnetite grains often occur as subrhombic, subround and elliptic σ-type porphyroblasts, and also display sinistral-shear sense (Fig. 5e). These features strongly support magnetite formation prior to hematite. In summary, the quartz itabirites, not only are characterized by microbands defined by alternating micrometer to millimeter-scale hematite-rich bands with the equal-scale quartz-rich bands (Figs. 4a, e and h, and 5f, g), but also generally show strongly shear deformation, mylonitization and oxidation-related alteration (Figs. 4d–h and 5a–f).

The Co–Cu ores are found within the lower segment of the sixth sequence of the Shilu Group (Fig. 3), and to a lesser extent, in the upper Fe ore layers, implying likely there are two stages of mineralization. According to Xu et al. (2013), Co primarily substitutes into pyrite and pyrrhotite, whereas chalcopyrite is the main cupriferous sulfide. Gangue minerals include dolomite and calcite, with subordinate pyroxene, amphibole, quartz, sercite and chlorite. The early stage of Co–Cu mineralization, which is parallel to the host banded or impure dolostones and/or pyroxene–amphibole-rich rocks (Fig. 6a, b), and concordant with the upper Fe ore layers (Fig. 2b, c), generally occurs as stratiform bodies along S_1 foliation planes (Figs. 6 and 7a–e). Consequently, the Cu–Co ores formed at this stage often display banded or massive structures shown by the presence of cobaltiferous pyrite/pyrrhotite + chalcopyrite macro- to microbands alternating mainly with similar scale, off-white dolomite + calcite bands, minor bands of black sericite + quartz (Fig. 7a–e and Xu et al., 2013). Lenticular, pinch-and-swell, irregular and brecciform Cu–Co ores are also observed (Fig. 7f, g and Xu et al., 2013). These textural features in the early stage of Co–Cu mineralization are extremely similar to those of the Mesoproterozoic sediment-hosted Sheep Creek Cu–Co–Ag deposit in the Belt–Purcell basin (Graham et al., 2012), and thus can be considered to be syngenetic and/or diagenetic in origin, but have been strongly reworked by the late-stage shearing and related dynamic metamorphism (Xu et al., 2013). In contrast, the disseminated, stockwork and brecciated sulfide minerals (Xu et al., 2013) likely are attributed to recrystallization due to the late stage of shearing and/or hydrothermal alteration. This interpretation is consistent with the occurrence of late stage metal sulfide (pyrite ± pyrrhotite ± chalcopyrite and/or galena ± sphalerite) stockworks or veinlets precipitated at various scales (ranging from 1 mm to 5 m) of structural foliations or fissures within the itabirites (or Fe ores) and/or interbedded host rocks (Xu et al., 2013). Moreover, the intensive hydrothermal alteration evidenced by the presence of secondary silica, carbonate, K-feldspar, garnet, amphibole, pyroxene (Fig. 7d, e) and barite is closely related to the late stage of sulfide mineralization (Xu et al., 2009). Consequently, the cryptocrystalline to microcrystalline textures dominate the early stage of Co–Cu ores, whereas subordinate colloform and coarse-grained or porphyritic textures distinguish the late stage sulfide minerals.

4. Sample preparations and analytical methods

Ten pyroxene–amphibole-rich rock and three banded or impure dolostone samples were collected from the Beiyi mine of the Shilu Fe–Co–Cu ore district (Fig. 2a). Major, trace and rare earth element (REE) analysis was performed at the SKLIG GIG-CAS (State Key Laboratory of Isotope Geochemistry, Guangzhou Institute of Geochemistry, Chinese Academy of Sciences). Major oxides were analyzed using Rigaku 100e X-ray fluorescence with precision better than 5%. Trace elements (including REE) were analyzed using PE Elan 6000 ICP-MS (inductively coupled plasma mass spectrometry) with precision better than 6%. Analytical details are the same as in Li et al. (2002b, 2002c, 2006b)).

Six quartz itabirite, eight amphibolitic itabirite and nine Co–Cu ore samples from the Beiyi mine of the Shilu ore district were also analyzed for major, trace and rare earth elements (REE). Major element analysis was carried out in the Langfang Laboratory of the Hebei Bureau of Geology and Mineral Resources, China. SiO_2 and LOI were analyzed using the gravimetric method, Al_2O_3, CaO, MgO and FeO using titration method, TiO_2, Fe_2O_3 and P_2O_5 using spectrophotometry, K_2O and Na_2O using flame photometry, and MnO using atomic absorption spectrometry. Trace elements plus REE analyses were carried out in the Baoding Supervision and Testing Center of Mineral Resources belonging to Chinese Ministry of Land and Resources, where GGX-2 atomic absorption spectrophotometer, AFS-2202E atomic fluorescence spectrometer, 7500a ICP-MS, VISTA-MPX plasma spectrometer, MUA trace uranium analyzer and ZSX100e X-ray fluorescence spectrometer, were used. The accuracy for major element determinations was estimated to be between 1 and 3%; for trace- and rare earth elements above 100 ppm, between 5 and 10%; and for lower parts per million, it is more variable.

Sm–Nd isotopic analyses on nine pyroxene–amphibole-rich rock samples and three banded or impure dolostone samples were performed on a Micromass Isoprobe multi-collector ICP-MS (Inductively Coupled Plasma-Mass Spectrometer) at the SKLIG GIG-CAS, following analytical procedures described by Li et al. (2006b). REE was separated using cation columns and Nd fractions were further separated by HDEHP-coated Kef columns. Measured $^{143}Nd/^{144}Nd$ ratios were normalized to $^{146}Nd/^{144}Nd = 0.7219$. The reported $^{143}Nd/^{144}Nd$ ratios was adjusted to the Shin Etsu JNdi-1 standard $^{143}Nd/^{144}Nd = 0.512115$.

5. Analytical results

5.1. Geochemical compositions

The analyses of major- and trace elements (including REE) for thirteen host rock, six quartz itabirite, eight amphibolitic itabirite and nine Co–Cu ore samples are presented in Appendices A1 to A6. For comparison, seventeen analyses of major oxides for the pyroxene–amphibole-rich host rocks from the Shilu ore district as reported by SCISTCAS (1986) are also listed in Appendix A1.

5.1.1. Host rocks

The pyroxene–amphibole-rich rocks exhibit large variation in major element compositions (Appendix A1; *volatile free*). The analyzed samples have a basic to intermediate SiO_2 (50.81 to 67.25 wt.%), associated with a relatively high but variable CaO (3.29 to 22.08 wt.%), MgO (3.56 to 15.26 wt.%) and Al_2O_3 (4.03 to 14.13 wt.%). Both the Fe_{tot} (Fe_2O_3 +

Fig. 4. Field photographs and photomicrographs of the Shilu district, showing texture, structure and mineral assemblage of the quartz itabirites (i.e. the Fe-rich ores or oxide BIF facies). (a) Blastobedding- or blastobanded-structure ores comprising alternating Fe-oxide (Hem, Mag)-rich band with Qtz-rich band. Mark pen show size. (b) Detrital Qtz with unequal sizes and subround to subangular morphologies showing weakly undulatory extinction, doubly polarized light. (c) Colloform ores indicated by colloidal Fe-oxides as adherent coatings on the gelatinous Qtz particles, plane-polarized light. (d) Ores with sinistral-shear Qtz porphyroblast surrounded by microplaty Hem crystals, reflected-light photomicrographs. (e) Microplaty Hem crystals developed along structural foliation S_1 and present as microbands alternating with Qtz-rich microbands, reflected-light photomicrographs. (f) Ores with "W-type" folded, recrystallized Qtz aggregation, doubly polarized light. (g) Ores with "fish-like" Qtz aggregation, doubly polarized light. (h) Mylonited ores showing the development of Hem along structural foliation S1 and the alternating Hem-rich microbands with Qtz-rich microbands, reflected light. Image (a) is from drill-hole ZKN0604, whereas images (b) to (h) from the Beiyi Fe mine at elevation +60 m. Qtz = quartz, Fe oxide(s) including Mag = magnetite and/or Hem = hematite. S_1 represents first schistosity. Arrows in (d) indicate shear sense.

FeO) and K_2O contents range from 2.39 to 8.56 wt.% and from 0.26 to 8.03 wt.%, respectively. There are negative correlations of Al_2O_3 with MgO and CaO (Fig. 8a, b), positive correlations with K_2O, TiO_2 (average content of 0.54 wt.%) and P_2O_5, and lack correlation with Fe_{tot} (Fig. 8c–f). Compositionally, the banded or impure dolostones are predominant in MgO (21.27–22.51 wt.%), CaO (29.17–30.21 wt.%) and

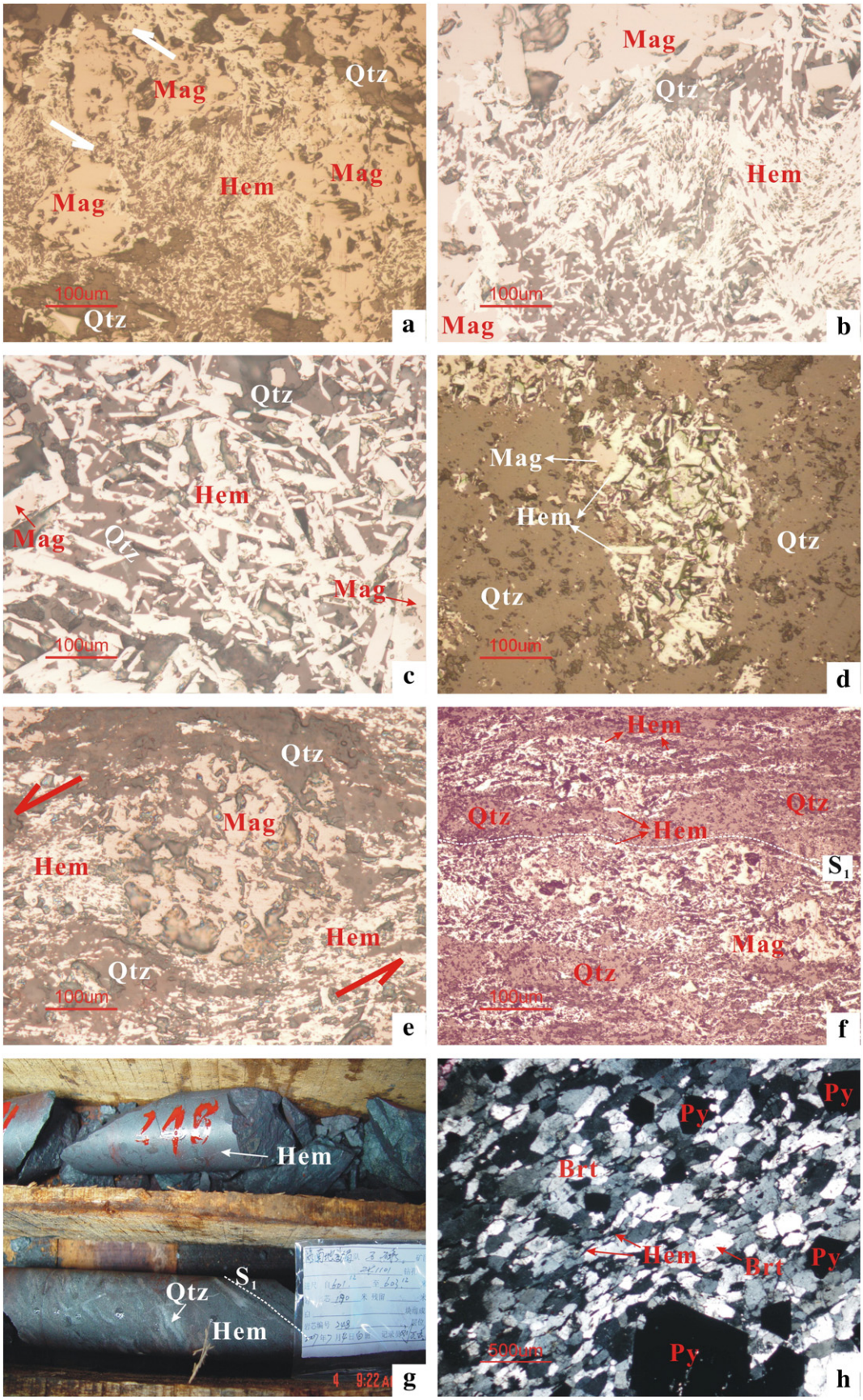

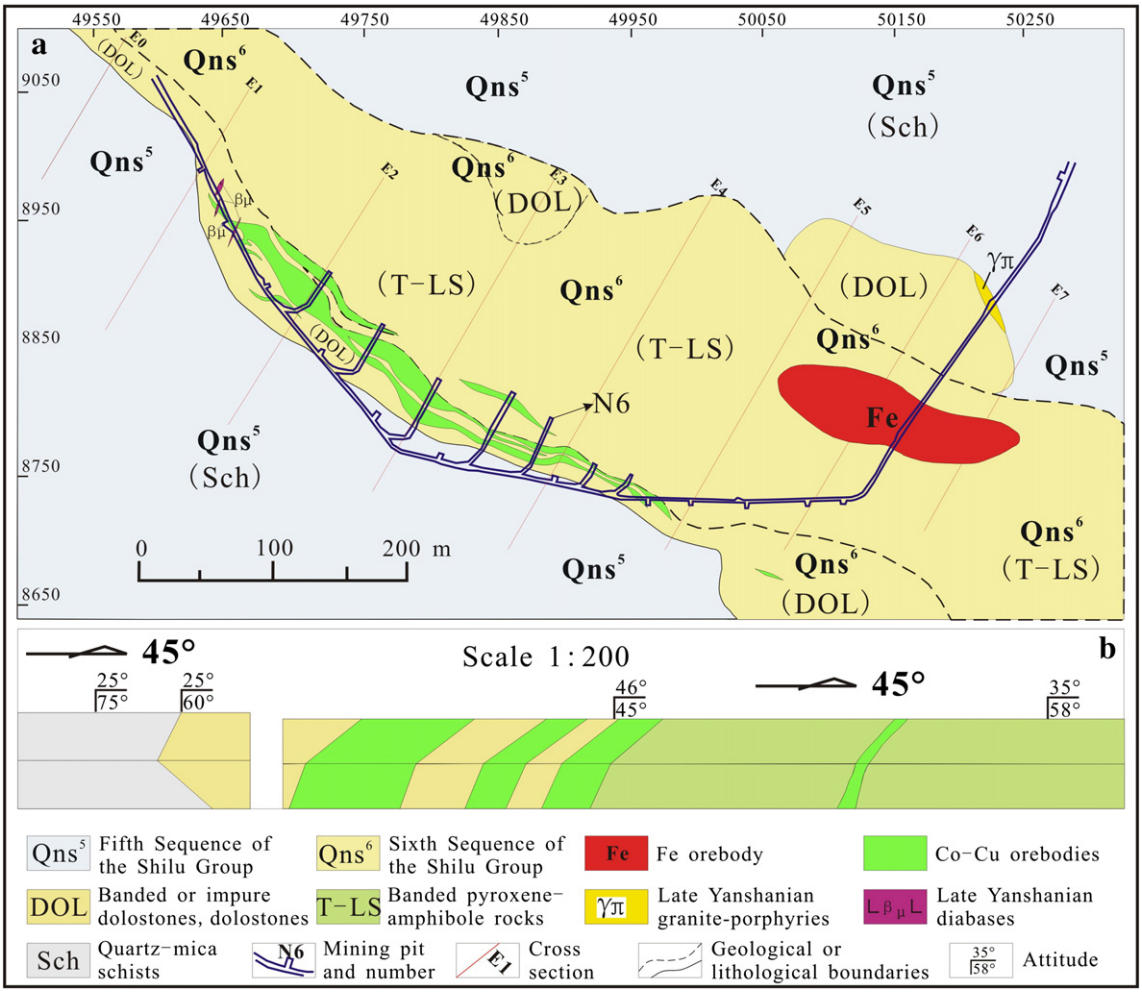

Fig. 6. Geological map (a) and cross section (b) at elevation −150 m below the Beiyi Fe orebody (see Fig. 2a) mainly showing distribution of the Co–Cu orebodies and their relationship to the Shilu Group host rocks. Panel b is from mining pit N6 in (a).

loss on ignition (LOI; 43.65–46.77 wt.%), which together comprise more than 94 wt.% of the total analyses (Appendix A1; *volatile-inclusive*). Relatively, sample ZSL6-29 is high in SiO_2, Al_2O_3 and K_2O contents, likely indicating an involvement of argillaceous source rocks, confirmed by mica (sericite, biotite) observed under microscope (Xu et al., 2009).

The pyroxene–amphibole-rich rocks have an average ∑REE of ~125 ppm (ranging from 79 to 175 ppm; Appendix A2), relatively lower than the PAAS (Post Archean Australian Shale of Taylor and McLennan, 1985). The PAAS-normalized REY patterns (Fig. 9a) show a general LREE depletion relative to relatively flat HREE (La/Yb_{PAAS} =0.17–1.00 and Gd/Yb_{PAAS} = 1.02–1.67). Except for sample ZSL6–7 with a positive Eu anomaly (δEu_{PAAS} = 1.37), most samples lack significant Eu (δEu_{PAAS} = 0.88–1.12) and Ce (δCe_{PAAS} = 0.93–1.13) anomalies. They also yield a weakly positive Gd anomaly and a chondrite-like (~28; Bau and Dulski, 1999) Y/Ho ratio (~27; Appendix A2). Compared to the PAAS, these samples have variable degrees of depletion in large ion lithophile elements (LILEs) including Rb, Sr, U and Pb, but are enriched in Ba (Fig. 10a). Except for Zr and Hf, the high field strength elements (HFSEs) are depleted. However, the average Zr and Hf values (~202 ppm and ~5.2 ppm, respectively) are comparable to that of UCC (upper continental crust; Rudnick and Gao, 2003). Transition metal elements (TME) including Cr, Co, Ni, V and Sc (Appendix A2) are lower than that of the PAAS but similar to those of the worldwide TTG (trondhjemite–tonalite–granodiorite), granites and felsic volcanic rocks of various ages (cf. Condie, 1993). Compared to the pyroxene–amphibole-rich rocks, the banded or impure dolostones have lower ∑REE (5.7–23.5 ppm; Appendix A2). The convex-upward PAAS-normalized REY patterns (Fig. 9b) are characterized by La/Yb_{PAAS} (0.75–1.01), La/Sm_{PAAS} (0.30–0.83) and Gd/Yb_{PAAS} (1.30–3.89). They also contain weakly to strongly positive Eu (δEu_{PAAS} = 1.13–1.57), weakly positive Pr (δPr_{PAAS} = 1.04–1.16), and moderately negative to zero Ce (δCe_{PAAS} =0.69–0.98) anomalies. Except for sample F8-12 with a slightly suprachondritic Y/Ho ratio (29), the Y/Ho ratios for other two samples are 44 and 45, respectively, approaching that of modern seawater (>44; Spier et al., 2007). In addition, all samples which show variable depletion in most of trace elements, especially the HFSEs (Zr, Hf, Nb, Ta, and Ti), and relatively enrichment in LILEs (Ba, U and Sr), relative to the PAAS

Fig. 5. Thin-section photomicrographs and field photographs of aspects of the Shilu district, showing texture, structure and mineral assemblage of the quartz itabirites (i.e. the Fe-rich ores or oxide BIF facies) and the Fe oxide-sulfide-bearing Brt-rich ores. (a) Microplaty Hem crystals present as deformed penniform or pisolitic matrixes surrounding Mag porphyroblasts. Arrows represents sinistral-shear sense. (b) A local enlargement of panel a, in which microplaty Hem aggregations show subtle folding. (c) Hem crystals with interlocking texture after replacement of Mag. Note the relic Mag crystals at the lower right corner. (d) Trellis-texture Mrt crystals as pseudomorphous Hem after replacement of Mag. (e) Mag as σ-type porphyroblasts displaying sinistral-shear sense (see arrows). Note numerous microplaty Hem crystals as tails of the Mag porphyroblasts. (f) Hem-rich bands alternating with Qtz-rich bands with identical strikes to the first foliation S1. Note the relic Mag porphyroblasts. (g) Drill-hole cores showing the same petrographical features as panel f. (h) Fe oxide (Hem, Mag)-sulfide (Py)-bearing Brt-rich ores, doubly polarized light. Note Brt crystals are characteristic of two approximately perpendicular sets of cleavage, whereas microplaty Hem crystals occur along these cleavages. Images (a) to (e) are reflected-light photomicrographs. Images (g) and (h) are from drill-hole ZK1011, and images (a) to (f) from the Beiyi Fe orebody at elevation +60 m. Hem = hematite, Mag = magnetite, Qtz = quartz, Brt = barite, Py = pyrite, and Mrt = martite.

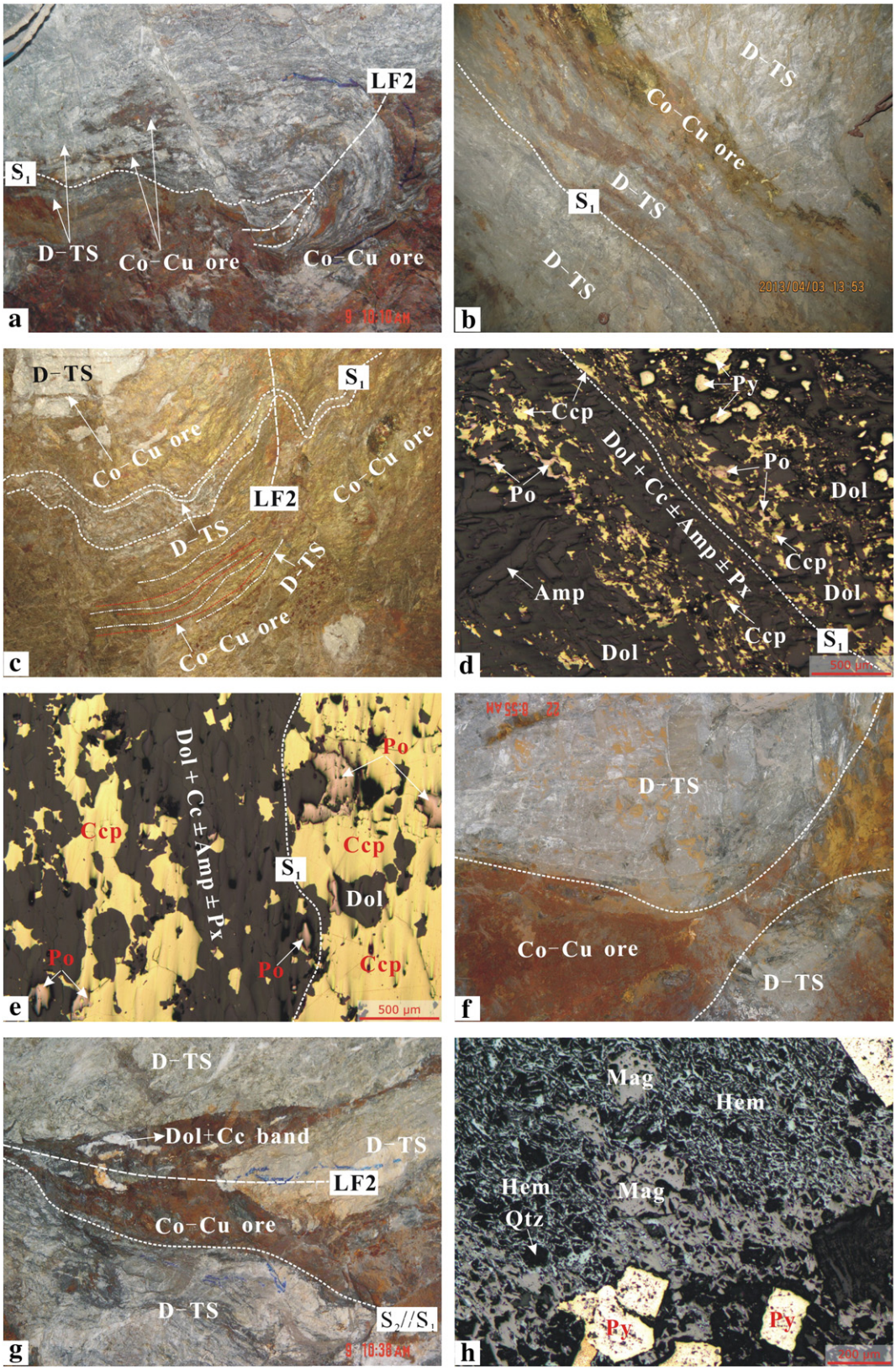

Fig. 7. Field photographs and photomicrographs illustrating occurrence and structural deformation of the Co–Cu ores (i.e. the sulfide–carbonate–silicate BIF facies) from Fig. 6, and their correlations with host rocks and Fe ores. (a) Stratiform-like ores showing banded structure and intrafolial shear folding (LF2) in the D-TS. (b) Banded ores interlayered with the D-TS. (c) Stratiform-like ores showing synchronous shearing (LF2) to the D-TS. Note the alternating presence of the D-TS bands with the ore bands. (d) Stratiform-like ores showing alternating sulfide-rich (Ccp + Po + Py) bands with Dol + Cc ± Amp ± Px bands, reflected-light photomicrograph. (e) Same as (d), but the sulfide-rich bands mainly comprise Ccp and Po. (f) Ores as pinch-and-well boudinages in the D-TS. (g) Strongly reworked, lentoid ores in the D-TS. Note the relic of rootless fold reflected by the discontinuous Dol + Cc band. (h) Oxide BIF facies locally intercalated with the Co–Cu ores, reflected light. S1 in (a) to (e) and (g) represents the first schistosity, and S2 in (g) is the second schistosity. $S_2//S_1$ in (g) indicates S_2 is approximately parallel to S_1. LF2 in (a), (c) and (g) show second fold axis. D-TS = banded or impure dolostones, Dol = dolomite, Cc = calcite, Qtz = quartz, Amp = amphibole, Px = pyroxene, Py = pyrite, Po = pyrrhotite, Ccp = chalcopyrite, Hem = hematite, Mag = magnetite.

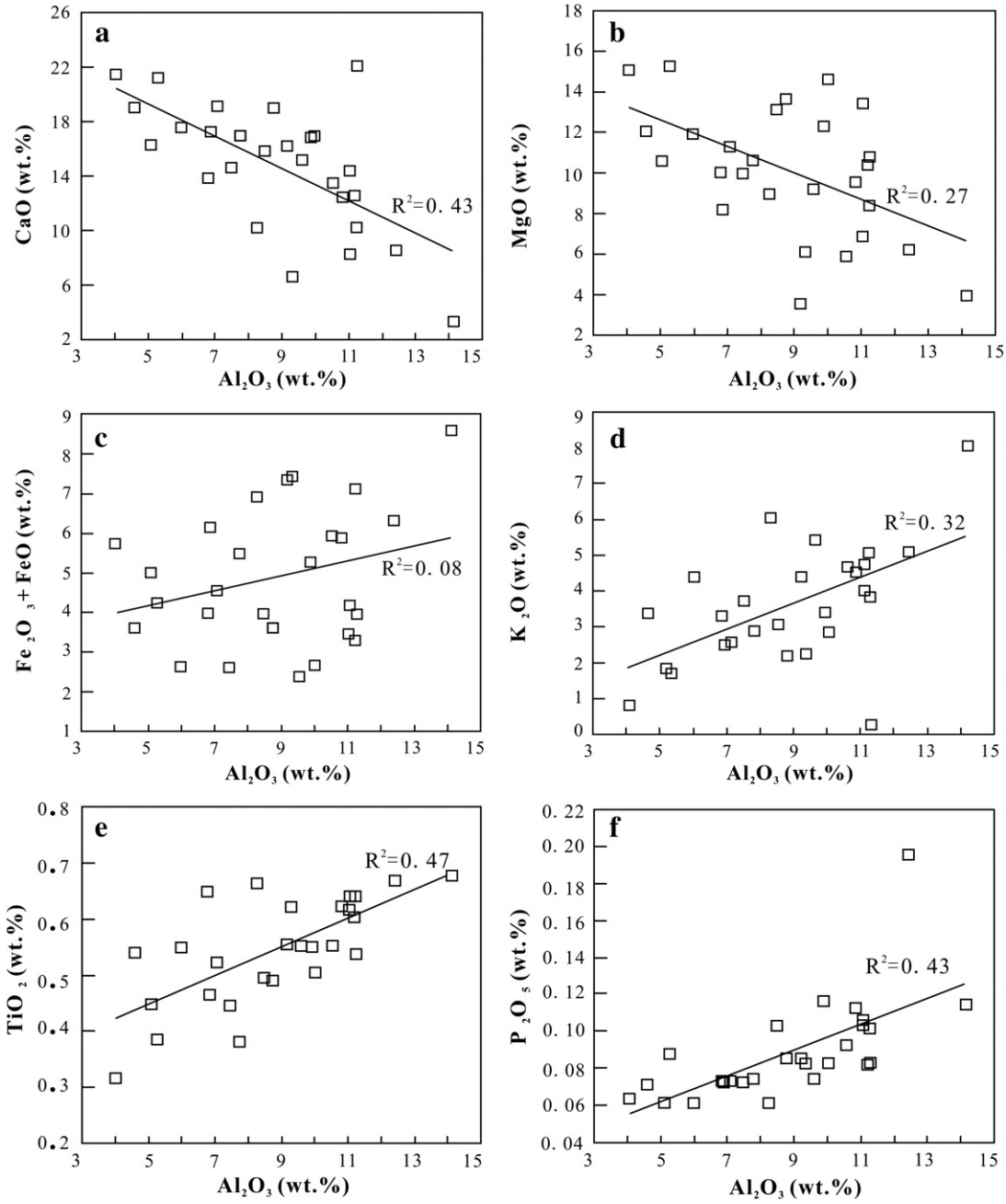

Fig. 8. Variant diagrams of Al_2O_3 with major oxides for the pyroxene–amphibole-rich rocks.

(Fig. 10b), are comparable to the Paleoproterozoic dolomitic itabirites and dolomite-rich bands of Spier et al. (2007).

5.1.2. Quartz- and amphibolitic itabirites

The quartz itabirites contain extremely high Fe_2O_3 (~64–84 wt.%) but low FeO (0.81–17.73 wt.%) and SiO_2 (10.16–29.15 wt.%) contents (Appendix A3; *volatile free*). Other major oxide contents are very low, generally below 2 wt.%. Except for sample BY-113 (0.77), most samples have $Fe^{3+}/(Fe^{3+}+Fe^{2+})$ ratios ranging from 0.95 to 0.99 (Appendix A3), indicating a high degree of oxidation. It is consistent with the generally martitization of magnetite (Figs. 5 and 6). Compared to the quartz itabirites, the amphibolitic itabirites (Appendix A3) are relatively low in Fe_2O_3 (~16–51 wt.%) but high and variable in SiO_2 (28.6–58.3 wt.%), Al_2O_3 (0.58–8.95 wt.%), FeO (1.85–15.22 wt.%) and other oxides TiO_2 (0.07–0.65 wt.%), MgO (0.12–3.52 wt.%), CaO (3.07–16.47 wt.%) and K_2O (0.03–3.40 wt.%). Because of a higher magnetite content (Xu et al., 2013), this type of itabirites also have relatively low $Fe^{3+}/(Fe^{3+}+Fe^{2+})$ ratios (0.69–0.93; Appendix A3), relative to the quartz itabirites. Moreover, there are negative correlation of SiO_2 with Fe_{tot} ($R^2 = 0.83$) and positive correlation of Al_2O_3 with TiO_2 ($R^2 = 0.65$) for all the quartz- ($R^2 = 0.98$ and 0.53, respectively) and amphibolitic ($R^2 = 0.48$ and 0.63, respectively) itabirites (Fig. 11a, b).

The $\sum$REE concentrations for the quartz itabirites are relatively low and range from 4.8 to 44.4 ppm (Appendix A4). The PAAS-normalized REY patterns (Fig. 9c), which reflect a large depletion in LREE relative to MREE ($La/Sm_{PAAS} = 0.15–0.73$) and HREE ($La/Yb_{PAAS} = 0.13–0.62$), and a weakly to strongly positive Ce anomaly ($\delta Ce_{PAAS} = 1.01–2.41$), are sorted into two groups. The less abundant Group I (Fig. 9c) contains slightly higher $\sum$REE (20.8–44.4 ppm), lower Y/Ho ratio (24–26) and no strong Eu anomalies ($\delta Eu_{PAAS} = 0.86–0.94$), which is comparable to most the pyroxene–amphibole-rich rock samples (Fig. 9a). In contrast, the predominant Group II (Fig. 9c) displays lower $\sum$REE (4.8–

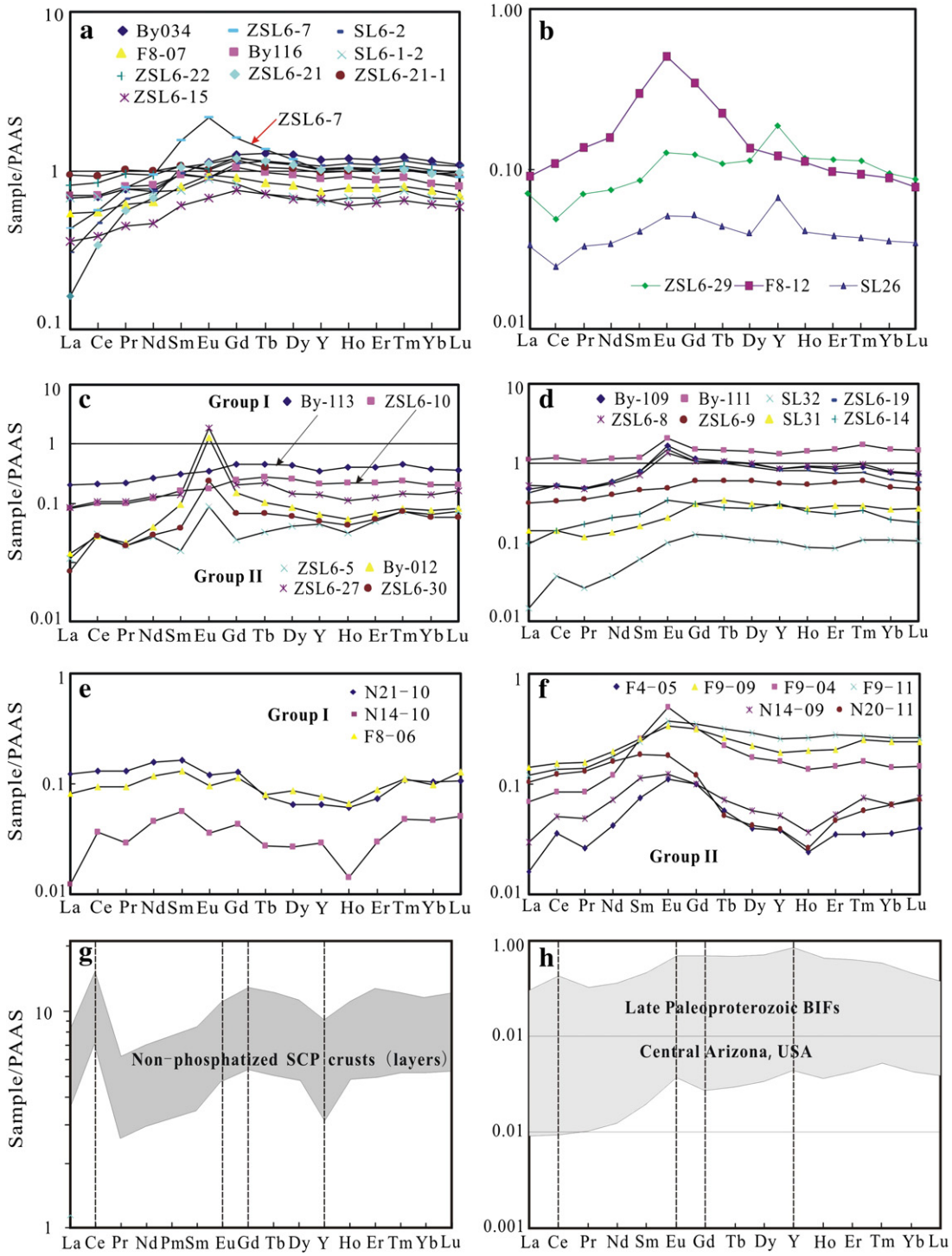

Fig. 9. PAAS-normalized REY spectra for the pyroxene–amphibole-rich rocks (a), banded or impure dolostones (b), quartz itabirites (c), amphibolitic itabirites (d), and Co–Cu ores (e and f). For comparison, this figure also compiles the REE + Y compositions of the marine hydrogenetic, nonphosphatized Fe–Mn crusts or crustal layers from the Central Pacific Ocean (g), and the late Paleoproterozoic BIFs related to submarine hydrothermal VMS deposits from Central Arizona, USA (h).
Panel g is after Bau et al. (1996). Panel h is after Slack et al. (2007). PAAS-normalized values after Taylor and McLennan (1985).

22.3 ppm), larger Y/Ho ratio (31–39) and strongly positive Eu anomalies (δEu_{PAAS} = 4.59–11.07). Group II also has high but variable Ba (up to 145,900 ppm), Sr (up to 3829 ppm), Cu (up to 515 ppm) and V (up to 1293 ppm) contents, and low but variable concentrations of Sc (0.10–0.82 ppm), Co (333–507 ppm), Mn (10–83 ppm), Zr (~2–54 ppm), and Hf (generally <2 ppm), relative to Group I (Appendix A4 and Fig. 10c, d). Compared to the quartz itabirites, the amphibolitic itabirites have high but variable $\sum$REE concentrations (7.3–216 ppm; Appendix A4). The PAAS-normalized REY patterns with the no Eu and Ce anomalies to strongly positive Eu and Ce anomalies (δEu_{PAAS} = 0.91–1.76 and δCe_{PAAS} = 0.99–1.90, respectively), and Y/Ho ratios of ranging from 25 to 34 (Fig. 9d), also display a large LREE depletion relative to MREE (La/Sm_{PAAS} = 0.24–0.96) and HREE (La/Yb_{PAAS} = 0.14–0.74). However, the amphibolitic itabirites have relatively higher though variable Mn (up to 5820 ppm), Rb (10–80 ppm), Zr (32–247 ppm), Nb (up to 13 ppm), Th (up to 11 ppm) and Cr (up to 53 ppm), and relatively lower Co, when compared with the quartz itabirites (Appendix A4 and Fig. 10e). The PAAS-normalized trace-element spider diagrams demonstrate that

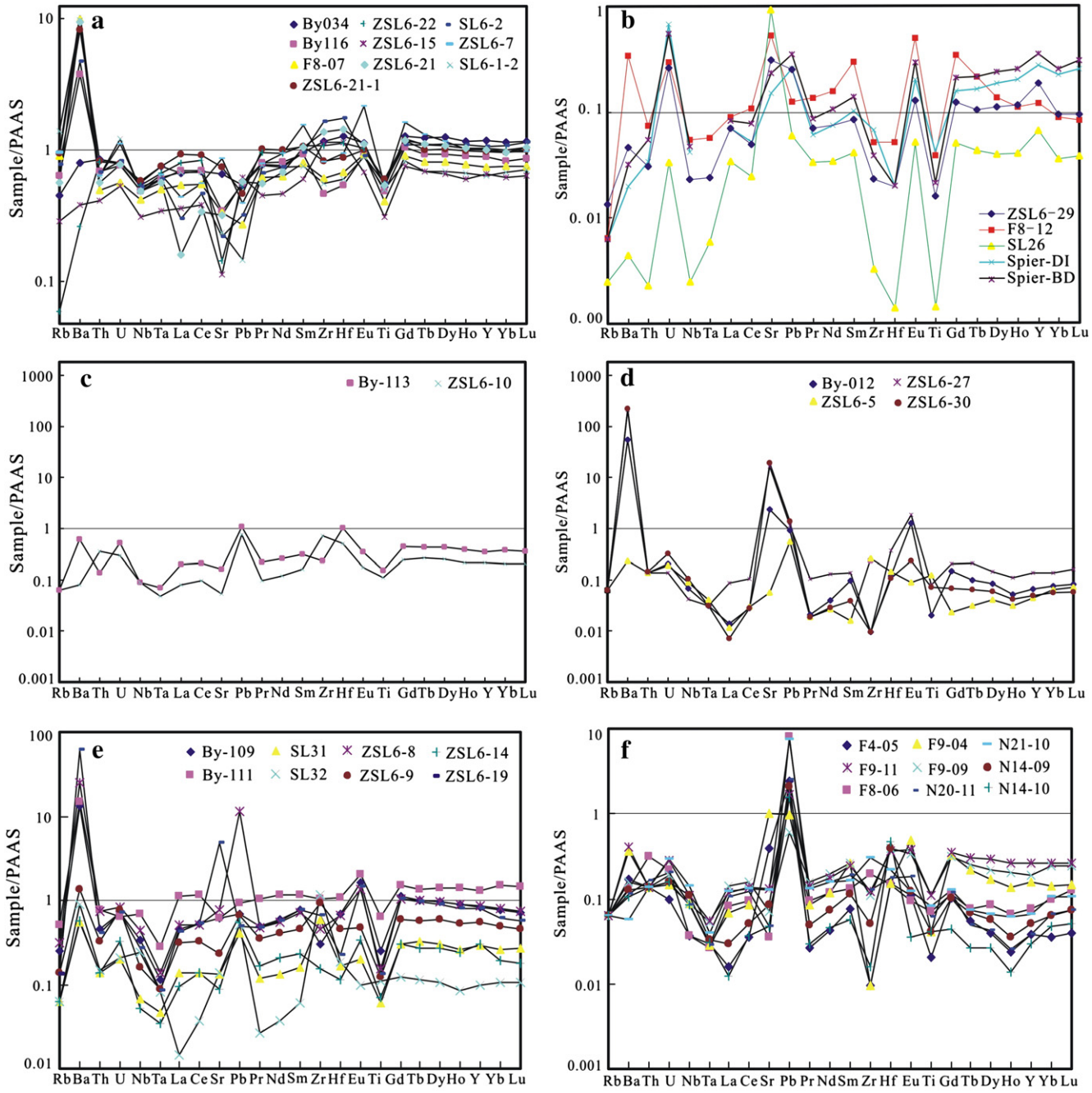

Fig. 10. PAAS-normalized multi-element plots for the pyroxene–amphibole-rich rocks (a), banded or impure dolostones (b), quartz itabirites (c and d), amphibolitic itabirites (e), and Co–Cu ores (f). Panel b also shows a comparison with those of the dolomitic itabirites (sample Spier DI) and therein dolomite-rich bands (sample Spier BDI) of Spier et al. (2007). PAAS-normalized values after Taylor and McLennan (1985).

this type of itabirite is generally depleted in Th, Nb, Ta, and Ti but enriched in Ba and Pb (Fig. 10e).

5.1.3. Co–Cu ores

Compared to their main host rocks, the banded or impure dolostones (Appendix A1), the Co–Cu ores (Appendix A5; *volatile-free*) have higher though variable contents of SiO_2 (9.7–69.5 wt.%, precluding sample F4-05), Al_2O_3 (0.59–2.83 wt.%), TiO_2 (0.03–0.13 wt.%), K_2O (0.02–0.26 wt.%), Na_2O (0.09–0.21 wt.%) and P_2O_5 (0.04–0.38 wt.%), and lower contents of MgO (0.16–22.21 wt.%), CaO (0.23–32.31 wt.%), MnO (0.01–0. 16 wt.%) and LOI (8.28–30.06 wt.%). The high but variable Fe_{tot} contents (~8.8–84.3 wt.%) yield variable $Fe^{3+}/(Fe^{3+} + Fe^{2+})$ ratios of 51 to 98 (Appendix A5). There is also a negative correlation of SiO_2 with Fe_{tot} ($R^2 = 0.69$) and a positive correlation of Al_2O_3 with TiO_2 ($R^2 = 0.55$; Fig. 11a, b).

The REE contents in the Co–Cu ore samples range from 6.1 to 31.6 ppm (Appendix A6), much lower than the PAAS but close to those of the quartz itabirites and the banded or impure dolostones. These samples (Appendix A6) also show weakly to strongly positive Ce ($\delta Ce_{PAAS} = 1.04–1.95$) anomalies and an enrichment in MREE relative to LREE ($La/Sm_{PAAS} = 0.21–0.75$). Based on the REE parameters, the analyzed samples can be subdivided into two groups. Group I, represented by samples F8-06, N14-10 and N21-10 (Fig. 9e), is characterized by relatively low $\sum$REE (6.1 to 24.1 ppm), moderately negative Eu anomalies ($\delta Eu_{PAAS} = 0.72–0.83$), highly variable La/Yb_{PAAS} (0.26–1.18) values, and relatively flat HREE patterns ($Gd/Yb_{PAAS} = 0.92–1.22$). Group II (Fig. 9f) is characterized by relatively high $\sum$REE

(6.5–31.6 ppm), positive Eu anomalies (δEu_{PAAS} = 1.15–1.71) and strong LREE depletion (La/Yb_{PAAS} = 0.45–0.58) relative to HREE (Gd/Yb_{PAAS} = 1.32–2.80) excluding sample N20-11 with La/Yb_{PAAS} = 1.60. The upward convex-type PAAS-normalized REE patterns are similar to those for some samples from the quartz- (Group II) and amphibolitic itabirites, and the banded or impure dolostones (Fig. 9b–d). In addition, some of the

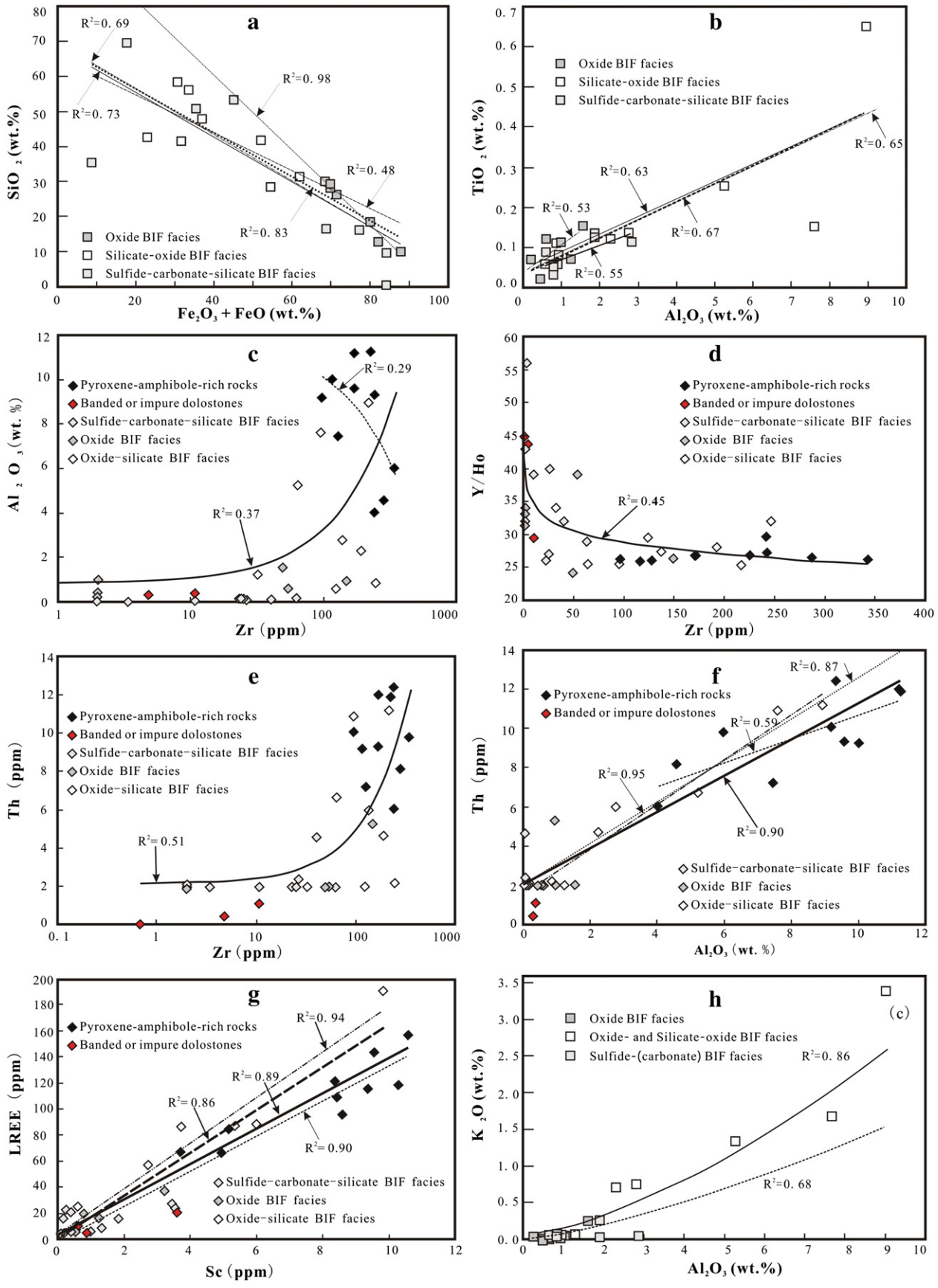

Co–Cu ore samples have a Y/Ho ratio between 39 and 56 (average of 45) close to the modern seawater value (Spier et al., 2007), whereas other samples have Y/Ho ratios between 26 and 32 (Appendix A6), close to those of chondrite and most crust components (26–28; Nozaki et al., 1997). The PAAS-normalized trace-element spider diagrams of the Co–Cu ores (Fig. 10f) reflect a remarkable enrichment in Pb with abundances of up to 162 ppm, higher than the itabirites, the banded or impure dolostones and the pyroxene–amphibole-rich rocks. A slight enrichment in Ba and U, and a slight depletion in Sr, Ta, Zr and Ti, are also clear (Fig. 10f). Additionally, other trace elements indicate variable degrees of depletion or enrichment (Fig. 10f). However, most trace elements (Appendix A6), except for Cu, Co, Ni, Pb, Zn, Ag and As, are lower in abundance relative to that of the PAAS, but akin to those of the quartz itabirites and the banded or impure dolostones (Appendices A2 and A4; Fig. 10b–d).

5.2. Sm–Nd isotopes results

The initial values of Sm–Nd isotopic components were calculated, based on the suggested depositional age of ca. 850 Ma for the Shilu Group (Xu et al., 2009). To reduce the effect of Sm/Nd fractionation, the calculation formula for two-stage Nd depleted mantle model age (T_{2DM}) was adopted from Li and McCulloch (1996). The measured Sm–Nd isotopic compositions including those cited from Zhang et al. (1992) and the calculated $\varepsilon_{Nd}(t)$ values and T_{2DM} ages are presented in Appendix A7.

Initial $^{143}Nd/^{144}Nd$ ratios (at 850 Ma) are 0.511152–0.511295 for the pyroxene–amphibole-rich rocks, 0.511109–0.511183 for the banded or impure dolostones, and 0.511192–0.511276 for the quartz itabirites, respectively (Appendix A7). Accordingly, the T_{2DM} ages and ε_{Nd}(850 Ma) values range from 1.90 to 2.13 Ga (average of 2.00 Ga) and from −4.80 to −7.61 (average of −5.99) for the pyroxene–amphibole-rich rocks, from 2.08 to 2.20 Ga (average of 2.12 Ga) and from −7.00 to −8.46 (average of −7.49) for the banded or impure dolostones, and from 1.93 Ma to 2.07 Ga (average of 2.01 Ga) and from −5.19 to −6.83 (average of −6.10) for the quartz itabirites, respectively. The average T_{2DM} ages and $\varepsilon_{Nd}(t)$ values for all the analyzed samples are 2.02 Ga and −6.27, respectively.

6. Data interpretation and discussion

6.1. BIF facies classification: implication for possible source(s)

A banded iron-formation is defined as a marine chemical sediment, typically thinly bedded or laminated, whose principal chemical feature is an anomalously high content of iron (generally ≥15 wt.% Fe), commonly but not necessarily containing layers of chert (James, 1954; Klein, 2005; Trendall, 1983). The term “itabirite” is extensively used in Brazil and denotes a metamorphosed iron-formation composed mainly of Fe-oxides (hematite, magnetite, martite) and quartz, with minor mica and other accessory minerals (Klein and Ladeira, 2000). On the basis of the geological, petrographical, mineralogical and geochemical investigation (Xu et al., 2013 and this study) and the iron formation facies classification of James (1954), the Shilu ore district appears to comprise three types of BIF facies: oxide BIF facies (with interbedded jaspilite bands), silicate–oxide BIF facies, and sulfide–carbonate–silicate BIF facies.

The oxide BIF facies, represented by the quartz itabirites or Fe-rich ores, is characterized by high Fe_{tot} content (69–88 wt.%; Appendix A3) and mainly contains hematite and quartz with minor magnetite, barite, garnet and anhydrite. Geological investigation also shows local presence of jaspilites in this type of BIF facies. Microbands, defined by alternating micrometer to millimeter-scale hematite-rich bands with the equal-scale quartz-rich bands, are well developed in this type BIF facies (Figs. 5, 6), where they have been interpreted as chemical varves or annual layers of sedimentation (Trendall, 2002), or as the result of episodic density flows (Krapež et al., 2003; Lascelles, 2007; Pickard et al., 2004). The silicate–oxide BIF facies, typically represented by the amphibolitic itabirites or Fe-poor ores, contains Fe_{tot} contents of 22 to 63 wt.% (Appendix A3) implying a mixture of Fe-rich calc-silicate and oxide in varying proportions. Unlike some of the Archean–Paleoproterozoic BIFs, such as the Hamersley Range of Western Australia and the Transvaal Supergroup of South Africa that have a general lack of metamorphism and deformation (Klein, 2005), the silicate–oxide BIF facies has a complicated mineralogy from intensive post-depositional processes including polymetamorphism and/or hydrothermal alteration (Xu et al., 2013). This BIF facies mainly comprises magnetite and hematite together with calc-silicate (garnet, pyroxene, amphibole and epidote), quartz and minor chlorite. Moreover, these minerals often occur as macrobands, mesobands and microbands at various scales (Xu et al., 2013), in which the latter are also very similar to fine laminations and/or microbanding in most Archean BIFs (e.g., Trendall, 2002). Trendall (2002) proposed that the mesoband sequence resulted from gross compaction and diagenesis of an originally continuous succession of relatively thick annual layers of precipitate. However, Hamade et al. (2003) interpreted mesobands as representing conditions that fluctuate between dominantly hydrothermal and continental control on a stable continental shelf. This interpretation is consistent with the presence of ooliths or spherolites in this type of BIF facies (Xu et al., 2013), which has been recognized as a primary lithology considered to be evidence of shallow marine, coastal shelf sedimentation (Pirajno et al., 2009). The sulfide–carbonate–silicate BIF facies or Co–Cu ores, underlies the silicate–oxide- and oxide BIF facies, and occurs as layers intercalated mainly with the banded or impure dolostones, subordinately with the pyroxene–amphibole-rich rocks or phyllites. This suggests a mixture of Fe-rich sulfide, carbonate and (calc-)silicate in varying proportions. The identification of this type of BIF facies corresponds to the rare presence of siderite at the bottom of the Fe ores (SCISTCAS, 1986), and a high but variable FeO_{tot} content (18–85 wt.%, excluding sample F9-04; Appendix A5). Mineralogically, this mixed BIF facies mainly contaINS Co- and Cu-bearing minerals (pyrite, pyrrhotite and chalcopyrite) together with dolomite, calcite, amphibole, pyroxene, sericite and quartz, which form alternating macro- to microbands (Fig. 7a–e).

The well-developed bandings at various scales in the Shilu BIFs ranging from coarse macrobands (meters in thickness) to mesobands (centimeter-thick units) to millimeter and submillimeter layers imply that the principal source of Fe, Si, Co and Cu was from deep ocean hydrothermal fluids admixed with seawaters (e.g., Klein, 2005; Trendall, 2002). The results of Pecoits et al. (2009) on the Dales Gorge BIFs in the Hamersley Province of Western Australia, however, indicated that the chemical components of BIFs were likely derived from both hydrothermal exhalations and weathering solutions derived from terrestrial sources. Hamade et al. (2003) also proposed that the sources of silica and iron were decoupled during BIF deposition, silica being dominantly derived from weathering of continental landmass whereas the iron had a hydrothermal origin. The presence of quartz detritus in both the oxide- and silicate–oxide BIF facies, as well as in the interbedded host rocks (Fig. 4a, b and Xu et al., 2013), likely indicates a contribution of terrigenous clastic components to the precursor sediments. Silicate minerals in the Shilu silicate–oxide BIF facies could be formed from

Fig. 11. Variation diagrams of Fe_2O_3 + FeO with SiO_2 (a), Al_2O_3 with TiO_2 (b), Zr with Al_2O_3 (c), Y/Ho (d) and Th (e), Al_2O_3 with Th (f), Sc with LREE (g), and Al_2O_3 with K_2O (h) for the Shilu BIFs of various facies and interbedded host rocks. $R^2 = 0.73$ in (a), $R^2 = 0.67$ in (b), $R^2 = 0.37$ in (c), $R^2 = 0.45$ in (d), $R^2 = 0.51$ in (e), $R^2 = 0.87$ and $R^2 = 0.90$ in (f), $R^2 = 0.86$ and $R^2 = 0.89$ in (g), and $R^2 = 0.68$ in (h) are for all the BIF facies and/or interbedded host rocks. $R^2 = 0.83$ in (a), $R^2 = 0.65$ in (b), $R^2 = 0.90$ in (f), $R^2 = 0.94$ in (g), and $R^2 = 0.86$ in (h) for both the oxide- and silicate–oxide BIF facies, $R^2 = 0.98$ in (a) and $R^2 = 0.53$ in (b) for the oxide BIF facies, $R^2 = 0.48$ in (a), $R^2 = 0.63$ in (b), and $R^2 = 0.95$ in (f) for the silicate–oxide BIF facies, $R^2 = 0.69$ in (a) and $R^2 = 0.55$ in (b) for the sulfide–carbonate–silicate BIF facies, and $R^2 = 0.29$ in (c), $R^2 = 0.59$ in (f), and $R^2 = 0.90$ in (g) for the pyroxene–amphibole-rich rocks, respectively.

terrigenous or volcanic components (e.g., Spier et al., 2007), although other authors interpreted the BIF facies as a silicate BIF formed by primary sedimentation (e.g., Klein and Ladeira, 2000; Veríssimo et al., 2002) or as a product of hydrothermal metasomatism of an original chert BIF by carbonate (e.g., Beukes et al., 2003). Locally, oolitic, granular and colloidal textures have been preserved in the Shilu silicate–oxide- and oxide BIF facies (Xu et al., 2013 and this study). Klein (2005) considered the development of oolitic or granular iron formations (GIFs) to be the result of a declining chemical density stratification due to reduced hydrothermal input. Similarly, Spier et al. (2007) suggested that the formation of BIFs could be related to the changes in the chemistry of seawater and in the input of terrigenous components due to sea-level fluctuations caused by marine transgression–regressions. The characteristics of ores as well as the petrographical and mineralogical signatures (Xu et al., 2013 and this study) reveal that the Shilu district is similar to the Fe-ore deposits hosted by the Minas Supergroup, Quadrilátero Ferrífero, Minas Gerais of Brazil (Dorr, 1969; Klein and Ladeira, 2000; Spier et al., 2003, 2007) in Fe-ore types (hematite-dominated), Fe-ore textures (from weakly oriented granoblastic to strongly oriented lepidoblastic/mylonitic), quartz- and amphibolitic itabirites and interbedded host rocks (metamorphosed siliciclastic and carbonate facies), and ore-controlled structures (folding and related shearing). Therefore, the precursor precipitates to the Shilu BIF facies most likely had been intercalated or mixed with variable amounts of detritus in a seawater environment (e.g., Spier et al., 2007). This is consistent with the diagram of Al_2O_3 vs. SiO_2 (Fig. 12a) in which most the Shilu BIF facies samples and the interbedded banded or impure dolostone samples plot in the hydrothermal field, whereas most of the interbedded pyroxene–amphibole-rich rock samples lie in the hydrogenous field.

6.2. Detrital input into the BIF facies and interbedded host rocks

Pure chemical sediments are enriched in Mn and Fe, but addition of Al-rich and Ti-rich detrital or volcanic material to hydrothermal/hydrogenous sediments decreases the Fe/Ti ratio and increases the proportion of Al with respect to the hydrothermal/hydrogenous elements Fe, Mn, Co and Cu, etc. (Barrett, 1981). The positive correlation of Al_2O_3 with TiO_2 for all the Shilu BIF facies and pyroxene–amphibole-rich rocks (Figs. 8e and 11b) has been interpreted to be the result of the incorporation of a detrital component (fine tuffaceous material) to the chemical precipitates, including some Archean to Neoproterozoic BIFs in the world (Basta et al., 2011 and references therein). The relative proportions of hydrothermal/hydrogenous and detrital sediments are illustrated in Fig. 12b, where both the oxide- and the sulfide–carbonate–silicate BIF facies samples plot towards the East Pacific Rise (EPR) metalliferous sediment end-member, whereas both the silicate–oxide BIF facies and the banded or impure dolostone samples plot on the mixing curve between the EPR metalliferous and the terrigenous sediment end-members. This suggests a contribution of sea floor-derived, metalliferous hydrothermal fluids to the oxide- and sulfide–carbonate–silicate facies BIFs, and an increasing proportion of terrigenous components to the silicate–oxide facies BIFs and the banded or impure dolostones. The higher Pb, Cu, Co, Ni and As contents but lower Sr, Ba and Mn, and HFSE concentrations in the sulfide–carbonate–silicate BIF facies, relative to these in the other BIF facies (Appendices A4 and A6; Fig. 10c–f), suggest essentially detritus-free precipitation (Frei and Polat, 2007). In contrast, the higher abundances of Al_2O_3, TiO_2, Zr, Nb, Th, Sc and Cr in the silicate–oxide BIF facies, relative to these in the oxide- and silicate–oxide facies ones (Appendices A3 to A6), are consistent with incorporation of higher amounts of clastic components (Arora et al., 1995; Gnaneshwar Rao and Naqvi, 1995; Manikyamba et al., 1993). Despite a predominant composition of MgO, CaO and LOI, and an extremely low concentration of Al, Cr, Co, Ni and HFSEs, minor input of terrigenous components into the precursors of the banded or impure dolostones can explain the elevated SiO_2 (up to 5.28 wt.%) and Sc (3.61 ppm) contents (Appendices A1, A2). The most significant is that the pyroxene–amphibole-rich rock samples plot close to the modern terrigenous sediment end-member, but clearly show a distribution trend to the EPR metalliferous sediment end-member along the mixing curve (Fig. 12b). This suggests that a continuous gradation from the source rocks to mixed chemical–detrital and pure chemical sediments is consistent with the hypothesis of two decoupled sources (e.g., Hamade et al., 2003; Krapež et al., 2003; Pecoits et al., 2009) during the sedimentation of the Shilu BIF facies and interbedded host rocks. These features therefore confirm that both the hydrothermal input and dilution of Al_2O_3-rich and TiO_2-rich clastic or volcanic materials were of importance for origins of the Shilu BIF facies.

Because terrestrial material (i.e., felsic and basaltic crust) has a constant Y/Ho ratio of ~26, Bolhar et al. (2004) proposed that smaller admixtures of any contaminant to chemical sediments precipitated from seawater would depress seawater-like superchondritic Y/Ho ratios (>44), and that co-variation would arise between Y/Ho and abundances of insoluble elements (e.g., Zr). The pyroxene–amphibole-rich rocks have a Y/Ho ratio of ~27, comparable to both the crustal and chondritic values (~28; Bau and Dulski, 1999). However, the Shilu BIF facies and interbedded banded or impure dolostone samples (Appendices A2, A4

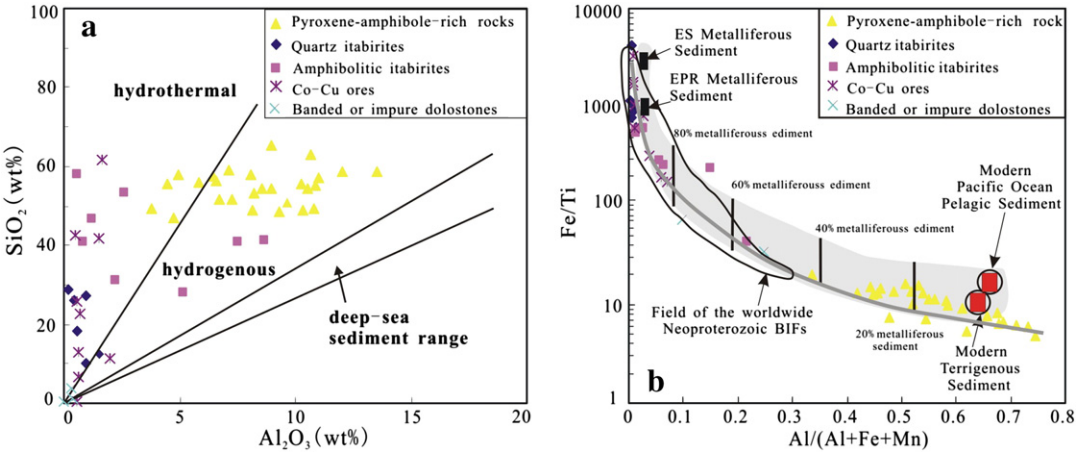

Fig. 12. Plots of Al_2O_3 vs. SiO_2 (a) and Al/(Al + Fe + Mn) vs. Fe/Ti (b) for all the Shilu BIFs of various facies and interbedded host rocks. The gray zone in panel b represent ideal mixing between metalliferous sediment and terrigenous sediment, and between metalliferous sediment and Pacific Ocean pelagic sediment (after Mukherjee, 2008). Likewise, a thick, gray curve representing mixing between metalliferous sediment and the Shilu host rocks of the pyroxene–amphibole-rich rocks is showed. Field of the worldwide Neoproterozoic BIFs (cf. Mukherjee, 2008 and references therein) are shown with a black outline. EPR = East Pacific Rise, RS = Rea Sea. For detailed explanation see the context.
Panel a is after Wonder et al. (1988). Panel b is after Boström (1973) and Mukherjee (2008).

and A6) either are both lower and higher than the crustal and chondritic values. This suggests a variable input of detrital contaminant to their precursor precipitates. The correlations of Zr with Al_2O_3, Th and Y/Ho, and of Al_2O_3 with Th (Fig. 11c–f) also confirm the presence of two end-member components, i.e. one with high Y/Ho and extremely low to insignificant Zr, Al and Th, and the other with low Y/Ho and high Zr, Al and Th, which are responsible for precursor sediments to the Shilu BIF facies, identical to the plot of Al/(Al + Fe + Mn) vs. Fe/Ti (Fig. 12b). Because hydrothermal solutions have a near chondritic Y/Ho ratio (Bau and Dulski, 1999 and references therein), it is possible that the Shilu BIFs and interbedded host rocks were deposited from solutions containing variable components of hydrothermal fluid, seawater and freshwater carrying detritus. This is supported by the fact that the Shilu BIFs and banded or impure dolostone samples with relatively high Y/Ho (generally ≥29 and up to 56) also contain relatively low Zr (<65 ppm) and Al_2O_3 concentrations (Appendices A1–A6).

6.3. Detrital components from a chemically evolved crust?

The strongly positive correlations of Sc (typically used for tracing continent-derived detrital components) with LREE ($R^2 = 0.89$ for all the analyzed samples, 0.86 for all the BIF facies samples, and 0.90 for all the interbedded host rock samples in the Fig. 11g) suggest co-sedimentation of a chemically evolved silicate component with the Shilu BIFs of various facies (cf. Frei and Polat, 2007). It accords with the positive correlations of Al_2O_3 with TiO_2 ($R^2 = 0.67$) and K_2O ($R^2 = 0.68$), and negative correlation of Fe_{tot} with SiO_2 ($R^2 = 0.73$; Fig. 11a, b and h). The weak correlation of Sc with SiO_2 as well as the lack correlations of Pr/Sm_{PAAS} with Rb/Sc and Y/Ho (*not shown*) for all the Shilu BIF facies samples, argues against the significance of variable land-derived REE-sources to explain the LREE/MREE variability observed in the Shilu BIF facies. It is compatible with a correlation of Fe_{tot} with Co + Cu + Ni (Fig. 13a) which in turn confirms that the Fe-rich source did effectively contribute trace elements Co, Ni and Cu to the Shilu BIFs, because those elements are characteristically enriched in mid-ocean ridge fluids (Frei and Polat, 2007). Additional evidence indicates the presence of barite-rich zones as 1–10 m thick, lenticular horizons grading laterally into the ferriferous phyllites and the oxide BIF facies in the Shilu ore district (SCISTCAS, 1986; Xu et al., 2009). This characteristic lenticular geometry has been thought to reflect formation as mounds around hydrothermal vents and as gravity-flow deposits in sea-floor swales downslope from submarine exhalative events (Poole, 1988). Our thin section observations also reveal that barite from the barite-rich zones occurs as granular to platy aggregation coexistent with acicular, hematite-rich Fe-oxides and pyrite (Fig. 5h), implying a common source for both the elements Fe and Ba. The origin of barite in BIFs is interpreted to be the result of precipitation when a reduced, Ba-bearing hydrothermal fluid mixed with an oxidized, sulfate-bearing seawater, as in VHMS deposits (Huston and Logan, 2004). Nijman et al. (1998) argued that most sulfates as anhydrite which has been observed in the Shilu district (SCISTCAS, 1986) precipitated originally as barite from low-*T* hydrothermal emanations analogous to white smokers. Because the tectonically active marine basin near a continental margin has been proposed for deposition of the stratiform barite deposits (Maynard and Okita, 1991), the Fe–(Si)–Ba element assemblage observed in the Shilu BIFs can be considered to be the result of association with volcanogenic hydrothermal fluids.

The application of Sm–Nd isotope to sedimentary rocks, including chemical precipitates has proven to be a powerful tool for characterizing both provenance and the tectonic evolution of the sedimentary basin and its hinterland (McLennan et al., 1990, 1993, 1995). Halverson et al. (2010) found that the pre-Sturtian (ca. 750 Ma) fine-grained sedimentary rocks in Australia are characterized by a significant positive excursion in $\varepsilon_{Nd}(t)$ values of shales, from −12 to near 0. Barovich and Foden (2000) considered this anomaly as recording eruption and weathering of early- to mid-Neoproterozoic continental flood basalts, presumably related to rifting of the eastern margin of the Australian craton during Rodinian fragmentation. Similarly, Li and McCulloch (1996) confirmed a dramatic decrease in T_{DM} ages from 1.8 Ga to 1.3 Ga (−10 to +0.6 $\varepsilon_{Nd}(t)$) in the mid-Neoproterozoic and early

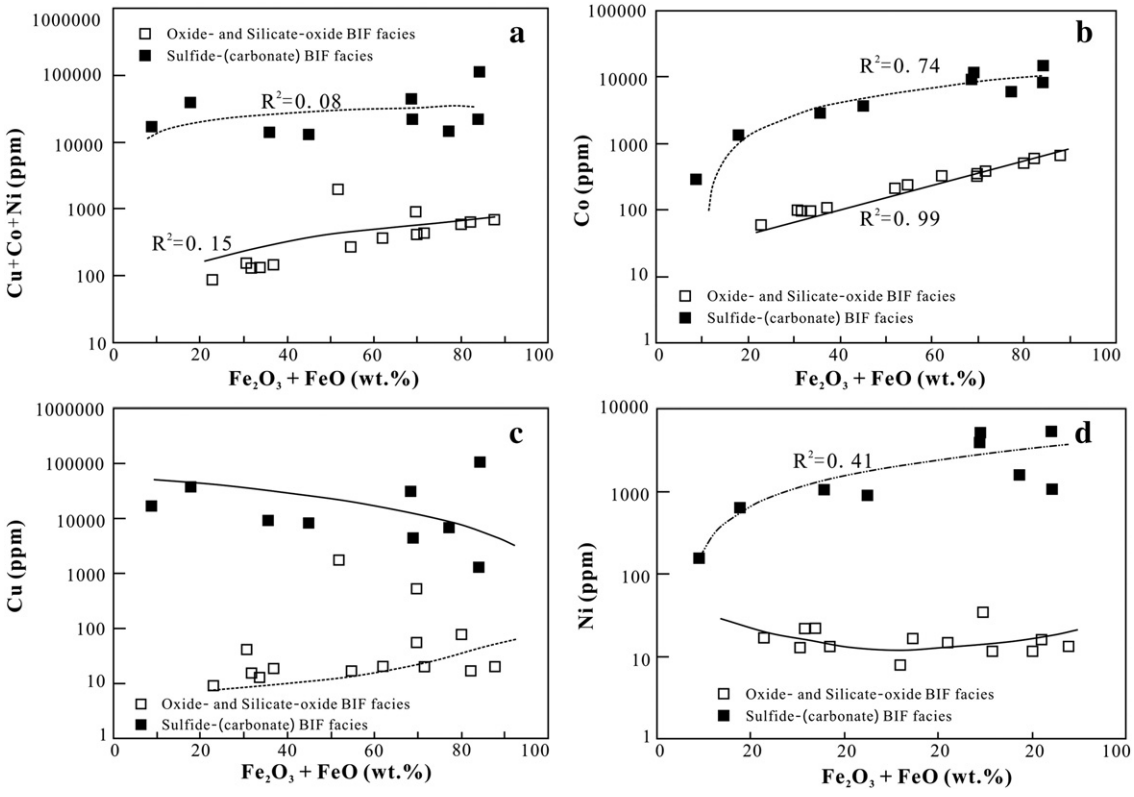

Fig. 13. Variant diagrams of Fe_2O_3 + FeO with Co + Cu + Ni (a), Co (b), Cu (c) and Ni (d), for all the Shilu BIFs of various facies. For detailed explanation see the context.

Sinian (900–770 Ma) sedimentary rocks from the southern margin of the Yangtze Block (smYB), and suggested a large increase in the proportion of juvenile mantle-derived materials from the provenance of those sediments. Miller and O'Nions (1985) concluded that most of the Nd in the Isua, Fig Tree, Hamersley, Negaunee–Biwabik, and Urucum BIFs was supplied by continental weathering based on the very negative ε_{Nd} values. Jacobsen and Pimentel-Klose (1988a, 1988b) and Derry and Jacobsen (1988) further reported Nd isotopic variations in Precambrian chemical sediments including BIFs and related clastic sediments, and suggested a trend of increasingly ε_{Nd} values with age from Proterozoic to Archean. They attributed this to the secular Nd isotopic variations of Precambrian seawater which were controlled by the relative magnitude of enriched continental components introduced principally in the dissolved load of rivers and depleted mantle components from submarine hydrothermal activity. Both the Shilu BIFs and interbedded host rocks, including the banded or impure dolostones, have a relatively constant T_{DM} age of ca. 2.0 Ga and an approximately uniform $\varepsilon_{Nd}(t)$ value of approximately −8.5 to −4.8 (Appendix A7). These $\varepsilon_{Nd}(t)$ values are comparable not only to most the Neoproterozoic BIFs (Fig. 14a; Derry and Jacobsen, 1988) but also to the Neoproterozoic to Early Paleozoic and present-day marine carbonates (Halverson et al., 2010 and references therein). Consequently, the negative ε_{Nd} values and T_{DM} ages (Appendix A7) from this study are interpreted to reflect a dominantly evolved crustal Nd source of Paleoproterozoic age to the precursor sediments in the Shilu BIFs and interbedded host rocks.

The wide range of Th/Sc ratios from 0.03 to 21 for the Shilu BIFs and interbedded host rocks implies that relative proportions of the various lithologies from active margin settings are highly variable and not necessarily fully homogenized during transport (i.e., more local sources and/or less sedimentary recycling), with the full range of mafic to felsic compositions being potential source rocks (McLennan et al., 1990). On a plot of Zr/Sc vs. Th/Sc (Fig. 14b) most of samples from this study plot approximately along the mixing line between andesite and upper crust but are dominated by an UCC composition. The $\varepsilon_{Nd}(t)$ vs. Th/Sc diagram (Fig. 14c) further suggests that the interbedded host rocks have a geochemical signature dominated by a felsic component with only minor mafic inputs. This is consistent with the fact that the pyroxene–amphibole-rich rocks contain UCC-like Zr and Hf, and felsic igneous rock-like transition metal element abundances (e.g., Cr, Co, Ni, V and Sc; Condie, 1993). The relatively lower but variable $\sum$REE abundances and relatively higher but variable CaO and MgO contents (Fig. 9a), relative to that of PAAS, as well as the weak negative correlation of Zr with Al_2O_3 ($R^2 = 0.29$ in Fig. 11c) and weak positive correlations of Al_2O_3 with K_2O ($R^2 = 0.32$ in Fig. 8d) and TiO_2 ($R^2 = 0.32$ in Fig. 8e), also suggest that the source of the pyroxene–amphibole-rich rocks likely contains a Ca–Mg-rich component comprising carbonates and/or

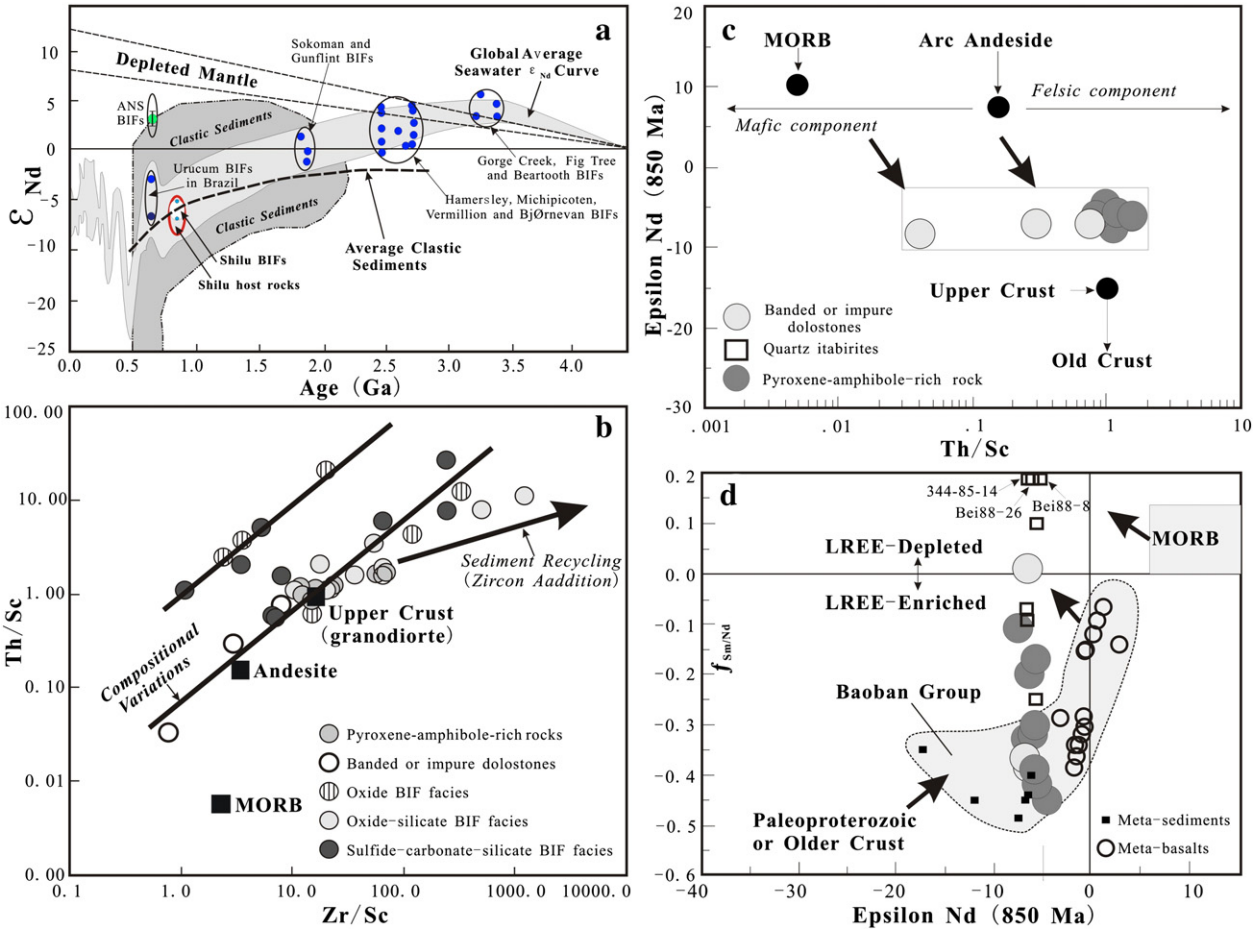

Fig. 14. Sm–Nd isotopic and trace elements characteristics of the Shilu oxide BIF facies and interbedded host rocks of pyroxene–amphibole-rich rocks and banded or impure dolostones. (a) ε_{Nd} vs. age (Ma), (b) Zr/Sc vs. Th/Sc, (c) Th/Sc vs. ε_{Nd}(850 Ma), and (d) ε_{Nd}(850 Ma) vs. fractionation factor ($f_{Sm/Nd}$). Arrows in panels c and d indicate general mixing trends for the Shilu oxide BIF facies and interbedded host rocks. Symbols in panel d also can be found in panel c. For detailed explanation see the context.
Panel a, which shows global average seawater ε_{Nd} curve for Precambrian BIFs is modified from Jacobsen and Pimentel-Klose (1988a). Except for ANS (Arabian–Nubian Shield) BIFs in Wadi Sawawin of NW Saudi Arabia from Mukherjee (2008), other Precambrian BIFs are from Jacobsen and Pimentel-Klose (1988a). Panel a also indicates Nd isotopic variations in clastic sediment and its average ε_{Nd} evolution curve, after Derry and Jacobsen (1990). Panel b is after McLennan et al. (1990) and shows that the protoliths to the Shilu host rocks of pyroxene–amphibole-rich rocks were sourced predominantly from an UCC composition. Panels c and d are after McLennan et al. (1993, 1995). Panel d also indicates a comparison in source area with the Paleo- to Mesoproterozoic Baoban Group underlying the Shilu Group in Hainan Island, and the field of Baoban Group at ca. 0.85 Ga is after Xu et al. (2001a, 2001b).

mafic rocks (Condie, 1993). Because only sedimentary rocks derived from the forearc region plot close to the andesite and (or) MORB fields (McLennan et al., 1993), these features suggest that our analyzed samples contain a mixture of upper crust or relatively older basement detritus and arc-derived detritus. Nevertheless, the $\varepsilon_{Nd}(t)$ vs. $f_{Sm/Nd}$ plot (Fig. 14d) suggests an extra LREE-depleted source, possibly MORB. Fig. 14b also indicates that a few samples from the sulfide–carbonate–silicate- and oxide BIF facies show a secondary trend subparallel to, but deviated from the mixing line between andesite and upper crust. This implies a small variation in trace element compositions, though the erosion and weathering of the predominant provenances introduced essentially all trace elements to most of our studied samples. The anomalous samples also have low HSFE contents and are highly enriched either in Fe and Ba or Mn (Appendices A4 and A5), which are comparable Fe–Mn–Ba deposits from the Northern Afar Rift in Ethiopia (Bonatti et al., 1972), consistent with a submarine hydrothermal fluid source.

The metasedimentary rocks and intercalated metabasalts with arc affinities (Xu et al., 2001a,b) in the Paleo- to Mesoproterozoic Baoban Group underlying the Shilu Group (Fig. 1b, c) have $\varepsilon_{Nd}(t = 850\ Ma)$ values ranging from −17.5 to +5.8 and T_{DM} ages from 2.9 Ga to 1.4 Ga (Fig. 14d). These values suggest not only the existence of a Paleoproterozoic or older crystalline basement in Hainan Island (Li et al., 2008; Xu et al., 2007a,b; Zhang et al., 1997) but also an input of depleted mantle-derived materials into the provenances of the Baoban Group. Because normal seawater is characterized by LREE depletion (Bolhar et al., 2004) and seafloor-derived hydrothermal fluids have a depleted-mantle ε_{Nd} value, our obtained $\varepsilon_{Nd}(t)$ values and trace element characteristics suggest that the Shilu BIFs are the result of mixing of submarine hydrothermal fluids with detrital components predominantly from an unknown, Paleoproterozoic or older crust and a minor component from the underlying Baoban Group, in a seawater environment.

6.4. Contamination and post-depositional processes

The Shilu BIF facies and interbedded host rocks generally show upward-convex PAAS-normalized REY patterns depicted by LREE depletion relative to MREE and HREE, zero Ce and Gd anomalies to strongly positive Ce and Gd anomalies, and negative La anomalies, except for two banded or impure dolostone samples ZSL6-29 and SL26 with strong enrichment in La ($\delta Ce_{SN} < 1$ and $\delta Pr_{SN} \approx 1$) and Y (Y/Ho ratios of 44 and 45, respectively), and strong depletion in Ce (Appendices A2, A4 and A6; Fig. 9a–f). Most of the analyzed samples also contain zero to distinctly positive Eu anomalies, with the exception of three sulfide–carbonate–silicate BIF facies samples (Group I) with moderately negative Eu anomalies (Appendix A6). In addition, MREE are enriched relative to the HREE ($Sm/Yb_{SN} = 1.03–3.34$) in most of the sulfide–carbonate–silicate BIF facies and interbedded host rocks, and a few silicate–oxide- and rare oxide BIF facies samples (Appendices A2, A4 and A6). Therefore, the majority of samples analyzed in this study have a deviation in PAAS-normalized REY pattern from the normal seawater and its proxies (i.e. chemical sediments), because the latter typically indicate LREE and MREE depletion relative to HREE, positive La, Gd and Y anomalies, and negative Ce anomalies (Bolhar et al., 2004). Consequently, the effects of contamination and/or post-depositional processes such as diagenesis, metamorphism and alteration on the REE + Y distribution in our studied samples need to be assessed carefully before interpreting chemical peculiarities of the precipitating waters and thus the depositional setting and origin.

The most critical sources of contamination are continent-derived detrital material, notably clay minerals, Fe–Mn oxides and sulfides (Frimmel, 2009). The geochemical and Nd isotopic features of the banded or impure dolostones (Appendices A1, A2 and A7) suggest contamination by detrital materials. However, their seawater-like PAAS-normalized REY patterns, except for sample F8-12 with no Ce anomaly (Fig. 9b), are in contrast to the flat, uniform shale-normalized patterns for the contaminated marine carbonate by shale components (Frimmel, 2009). Likewise, the generally subparallel trace element patterns for the Shilu BIFs (Figs. 9c–f and 10) suggest that contamination by detrital materials would not severely modify their REE + Y distributions, though the geochemical and Nd isotopic compositions account for a variable input of clastic or volcanic materials into their source region(s) (Figs. 11, 12 and 14). These are consistent with a weakly positive correlation of Zr with REE ($R^2 = 0.28$) for all the BIF facies samples (Fig. 15a). The absence of, or weak correlations of Zr with redox-sensitive elements (e.g., Eu, Fe, Mn and Ba) for the Shilu BIFs (Fig. 15b, c) also shows that detrital contributions to redox-sensitive elements are minor (e.g., Huang et al., 2011). A contribution of Mn from a continental source, likely as dissolved or suspended loads to the BIFs is possible, because there are moderately positive correlation of Mn with Th ($R^2 = 0.58$) for all the Shilu BIF facies, and moderately negative correlations of Mn with Fe for both the oxide- and silicate–oxide- ($R^2 = 0.47$) and the sulfide–carbonate–silicate ($R^2 = 0.53$) BIF facies (Fig. 15d, e).

The preservation of abundant primary textures and the generally greenschist facies metamorphism of the Shilu Group (Yao et al., 1999; Xu et al., 2009, 2013 and this study) suggest that the influence of post-depositional processes on the REE + Y composition of chemical sediments likely is minor (Bau, 1993; Bau and Dulski, 1996). However, intense hydrothermal alteration can lead to variable Eu enrichments or deficiencies (Bolhar et al., 2004), depending on the redox state of the hydrothermal fluid and its total sulfur activity (Frimmel, 2009). For most of our analyzed samples, the upward-convex PAAS-normalized REE patterns (Fig. 9a–f), with low La/Sm_{PAAS} (0.15–0.96) and high Gd/Lu_{PAAS} ratios (mostly between 1.04 and 2.55), and positive Eu anomalies (δEu mostly between 1.12 and 11.07) (Appendices A4 and A6), are typical of high-*T* (temperature) hydrothermal fluids derived from either crustal or oceanic environments (Torres-Ruiz, 2006 and references therein). The metasomatic replacement of marine carbonates by high-*T* (>200°–250 °C), acid and reducing, crustal hydrothermal fluids can result in a largely negative $\delta^{13}C_{V\text{-}PDB}$ value and a low $\delta^{18}O_{V\text{-}SMOW}$ value in metasomatic products (Torres-Ruiz, 2006). However, the $\delta^{13}C_{V\text{-}PDB}$ values (between −5.40 and +2.5‰; Xu et al., 2009) for the Shilu BIF facies and interbedded host rocks are in the range of Neoproterozoic marine carbonates (Halverson et al., 2010), comparable to the $\delta^{13}C$ values of carbonates (+0.83 to −7.0‰) for Neoproterozoic Rapitan-type BIFs associated with "Snowball Earth" (Klein and Ladeira, 2004). Especially, the banded or impure dolostones have a positive $\delta^{13}C_{V\text{-}PDB}$ value ranging from +0.6 to +2.5‰, matching with that of global 850–900 Ma (middle Tonian) carbonates (Purohit et al., 2012). Their $\delta^{18}O_{V\text{-}PDB}$ values (−12.0 to −7.3‰; Xu et al., 2009) could also be primary, because the Proterozoic carbonates have $\delta^{18}O_{V\text{-}PDB}$ values ranging from −10 to −5‰ (Banner and Hanson, 1990). Therefore, the depletion in C isotope can be considered to be the result of significantly submarine hydrothermal input (e.g., Klein and Ladeira, 2004).

However, all the Shilu BIF facies and the pyroxene–amphibole-rich rocks display a distinctly lower $\delta^{18}O_{V\text{-}SMOW}$ value (+4.7 to +12.5‰; Xu et al., 2009) than typical Neoproterozoic dolostones (Halverson et al., 2010). This is likely the result of diagenetic alteration as O-isotope compositions are often more susceptible to diagenesis than C-isotope compositions due to the greater abundance of oxygen atoms over carbon atoms in meteorically derived diagenetic fluids (Ling et al., 2007). Alternatively, the depletions of ^{18}O in the Shilu BIFs and interbedded host rocks are considered to be the result of hydrothermal alteration related to regional metamorphism or granitic intrusions leading to rock recrystallization and mass exchange. However, a highly oxidizing hydrothermal fluid, which most likely formed the altered and/or metamorphosed calc-silicate minerals garnet (andradite–grossular series), pyroxene (diopside–hedenbergite series), amphibole (actinolite–tremolite series) and epidote in the Shilu district (unpublished data), is inconsistent with the high-*T*, acid and reducing, crustal fluids

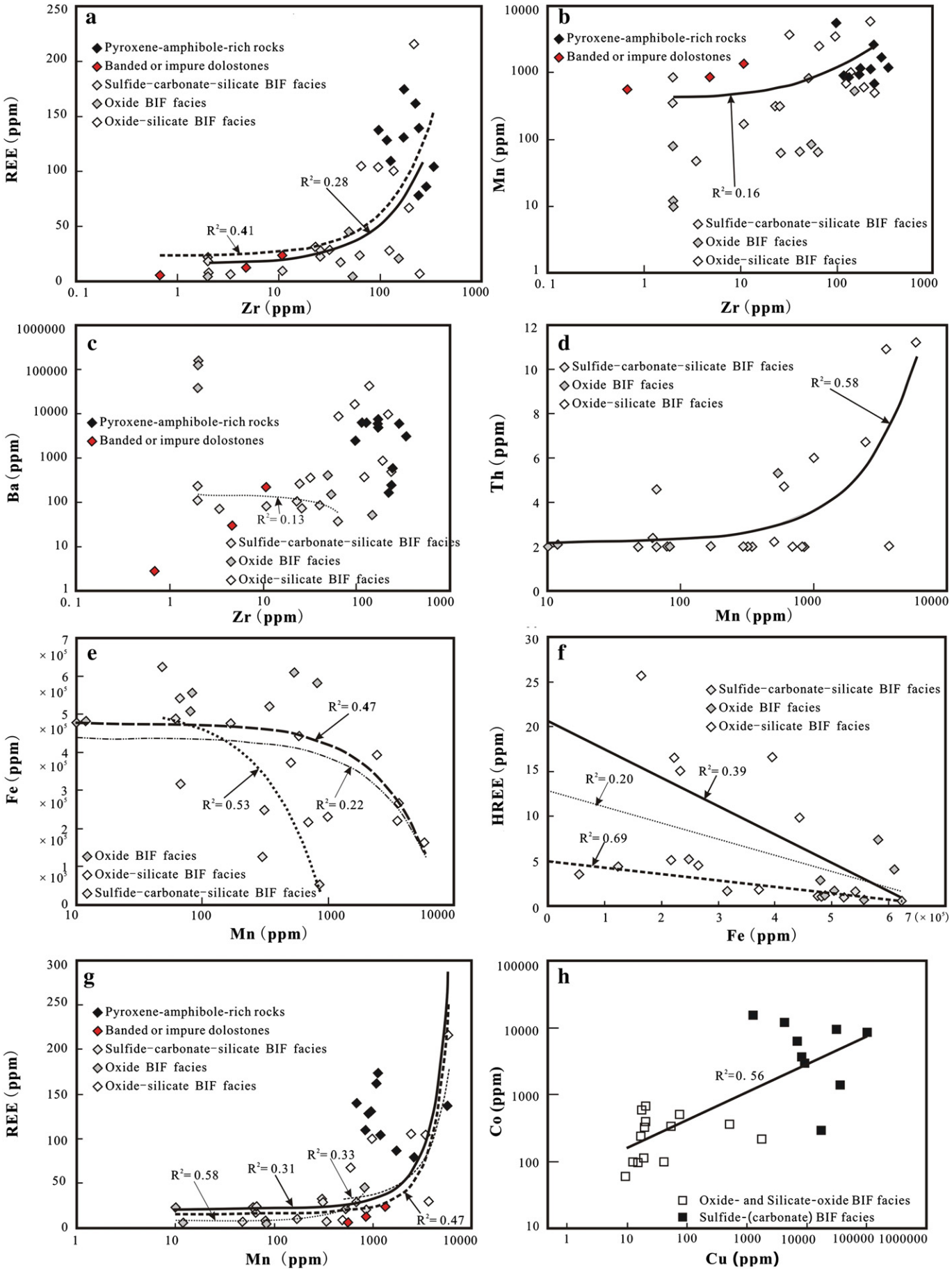
a
Pyroxene-amphibole-rich rocks
Banded or impure dolostones
Sulfide-carbonate-silicate BIF facies
Oxide BIF facies
Oxide-silicate BIF facies
R²= 0.28
R²= 0.41
REE (ppm)
Zr (ppm)
b
Pyroxene-amphibole-rich rocks
Banded or impure dolostones
R²= 0.16
Sulfide-carbonate-silicate BIF facies
Oxide BIF facies
Oxide-silicate BIF facies
Mn (ppm)
Zr (ppm)
c
Pyroxene-amphibole-rich rocks
Banded or impure dolostones
R²= 0.13
Sulfide-carbonate-silicate BIF facies
Oxide BIF facies
Oxide-silicate BIF facies
Ba (ppm)
Zr (ppm)
d
Sulfide-carbonate-silicate BIF facies
Oxide BIF facies
Oxide-silicate BIF facies
R²= 0.58
Th (ppm)
Mn (ppm)
e
R²= 0.47
R²= 0.53
R²= 0.22
Oxide BIF facies
Oxide-silicate BIF facies
Sulfide-carbonate-silicate BIF facies
Fe (ppm)
Mn (ppm)
f
Sulfide-carbonate-silicate BIF facies
Oxide BIF facies
Oxide-silicate BIF facies
R²= 0.20
R²= 0.39
R²= 0.69
HREE (ppm)
Fe (ppm)
g
Pyroxene-amphibole-rich rocks
Banded or impure dolostones
Sulfide-carbonate-silicate BIF facies
Oxide BIF facies
Oxide-silicate BIF facies
R²= 0.58
R²= 0.31
R²= 0.33
R²= 0.47
REE (ppm)
Mn (ppm)
h
R²=0. 56
Oxide- and Silicate-oxide BIF facies
Sulfide-(carbonate) BIF facies
Co (ppm)
Cu (ppm)

for C and O isotope fractionations in metasomatic rocks (e.g., Torres-Ruiz, 2006). Textural relations in the Shilu oxide- and silicate–oxide BIF facies (Figs. 5, 6) also reveal that magnetite preceded the formation of hematite, implying a post-depositional hydrothermal replacement origin for the Shilu hematite-rich Fe ores due to partial or full martitization of magnetite. Magnetite, the main mineral in iron formations, only forms at low-*T* under reduced redox conditions and low sulfur levels (Huston and Logan, 2004). In contrast, the transformation of magnetite into martite/hematite is commonly ascribed to the influx of high pH and/or oxidizing fluids during later hydrothermal alteration (Webb et al., 2003). Therefore, magnetite as the predominant primary Fe-oxide mineral in the Shilu BIFs reflects a reducing (f_{O_2} below the hematite/magnetite buffer; Bau and Dulski, 1996), highly acidic hydrothermal fluid for the BIF sedimentation (Beukes et al., 2008; Klein, 2005). This is consistent with a low $Fe^{3+}/(Fe^{3+} + Fe^{2+})$ ratio for the silicate–oxide BIF facies (Appendix A3), due to elevated abundance of magnetite with $Fe^{3+}/(Fe^{3+} + Fe^{2+})$ ratio of 0.67 (Klein, 2005). The Eu^{3+}/Eu^{2+} redox potential in aqueous solutions depends mainly on *T* and to a lesser extent on pressure, pH and REE speciation (e.g., Bau, 1991), which explains the positive Eu anomalies typically found in acidic, reducing hydrothermal fluids. Therefore, the positive Eu_{SN} anomalies in most the Shilu BIF facies samples can be recognized as a primary feature of PAAS-normalized REY patterns (Fig. 9a–f) which records interaction of hydrothermal plume particles with seawater, whereas variable Eu anomalies may reflect fluctuations of the mixing ratios of high-*T* and low-*T* hydrothermal fluids (Bau and Dulski, 1996).

6.5. Chemical peculiarities of the precipitating waters

The majority of the PAAS-normalized REY patterns from this study show positive Eu, Ce and Gd anomalies, and LREE depletion relative to HREE (Fig. 9a–f), and consequently can be distinguished from the almost flat PAAS-normalized REY pattern with slight uniform LREE depletion and no anomalies for modern lake and river waters (Bolhar and Van Kranendonk, 2007; Caron et al., 2010; Frimmel, 2009). The generally positive Ce anomalies in the majority of samples from this study also contrast with the commonly negative Ce anomalies of estuarine waters which represent the physical link between freshwater pathways and the open marine environment (Bolhar and Van Kranendonk, 2007). It therefore appears that the Shilu BIFs and interbedded host rocks were not formed in an estuarine setting. The slight MREE enrichment relative to the HREE and LREE which is shown by an upward-convex PAAS-normalized REY pattern for some samples (Fig. 9a–f) may reflect a stronger "river signature", or an "acidic lake signature", as has been reported for some modern rivers (the dissolved river loads or colloidal pool; Elderfield et al., 1990) and low-pH acidic lakes (Johannesson and Zhou, 1999). The positive Gd anomalies observed in the Shilu samples also seems impossible do not allow for differentiation between lacustrine and marine deposition, because positive Gd anomalies were found to be a prevalent feature in freshwater environments (Bolhar and Van Kranendonk, 2007) or may be generated during REY sorption (Bau et al., 1996). A relatively flat, shale-normalized REE pattern with very prominent positive Eu anomaly, however, has been reported in MOR (mid-ocean ridge) hydrothermal fluids (Derry and Jacobsen, 1990). The lacustrine sediments are also conspicuous in having virtually flat, unfractionated PAAS-normalized REY patterns, and no elemental anomalies (Bolhar and Van Kranendonk, 2007). Thus a shallow-water, lacustrine or lagoonal environment under freshwater influence (e.g., Caron et al., 2010) can be ruled out for deposition of the Shilu BIFs and interbedded host rocks. It is consistent with the fact that most the Shilu BIFs contain a Pr/Sm_{SN} ratio of 0.22 to 0.79 (Appendices A4 and A6) and that the banded or impure dolostones typically show REY seawater signature (Fig. 9b).

The development of zero to positive Ce anomalies in samples from this study has also been reported not only in marine hydrogenetic Fe–Mn oxide crusts and nodules (Bau et al., 1996; Bonatti et al., 1972; Toth, 1980) but also in Neoproterozoic hydrogenetic marine manganese formations (Gutzmer and Beukes, 1998) and carbonates (Frimmel, 2009), and Precambrian BIFs with or without associated deep-ocean volcanogenic massive sulfide (VMS) deposits (Derry and Jacobsen, 1990; Frei et al., 2008; Fryer, 1977; Kato et al., 1996; Planavsky et al., 2010; Slack et al., 2007). The anomalous Ce behavior has been linked either to preferential incorporation of Ce from seawater into Ce^{IV} compounds (e.g., Fe–Mn oxyhydroxides) after oxygenation of the then atmosphere (Bau, 1999; Bau and Dulski, 1996) or to reductive dissolution of settling Fe–Mn particles in a deeper suboxic and anoxic water column (German et al., 1991) or to diagenetic processes and redox cycling similar to modern reducing environment (Derry and Jacobsen, 1990; Fryer, 1977). The relatively uniform zero to positive Ce anomalies in the Shilu BIF facies (Appendices A4 and A6), unlike the variable negative or positive Ce anomalies in Precambrian BIFs (Derry and Jacobsen, 1990; Fryer, 1977), suggest that our observed Ce anomaly may be primary and that the effect of diagenetic redox changes on Ce behavior was insignificant. The PAAS-normalized REY patterns (Fig. 9a and c–f), excluding the banded or impure dolostones, are similar to those of marine hydrogenetic, nonphosphatized Fe–Mn crusts or crustal layers from the Central Pacific Ocean (Fig. 9g), because the latter also show LREE depletion, negative Y anomalies, positive Eu and Gd anomalies, and in most cases, Ce. However, the Shilu BIFs and interbedded host rocks are distinguishable from these Fe–Mn crusts, as the latter not only have extremely high MnO contents (up to 33 wt.% Mn) but also contain a considerably lower Y/Ho ratio (between 25 and 17) than seawater or common igneous and clastic rocks (Bau et al., 1996). The observed anomalous Ce behavior in this study therefore did not result from oxidation on marine hydrogenetic Fe–Mn crust. Finally, the oxide shuttle model of Planavsky et al. (2010) which has been put forward to explain the anomalous Ce behavior in the late Paleoproterozoic BIFs with high MnO contents and high LREE/HREE ratios also could not be applied to our observed REY patterns.

Slack et al. (2007) proposed a model to interpret the presence of moderate positive to small negative Ce anomalies in the late Paleoproterozoic BIFs related to submarine hydrothermal VMS deposits. They suggested that the redox state of the deep ocean at that time was at a transitional, suboxic state with low dissolved O_2 concentrations but no H_2S, which allows continued adsorption/desorption of REE, including oxidative Ce scavenging mediated by the Fe oxyhydroxide surfaces and the formation of positive Ce anomalies in BIFs. The similarities in PAAS-normalized REY pattern between the late Paleoproterozoic and the Shilu BIFs (Fig. 9c–f and h) implies that this model seems plausible to explain our obtained Ce anomalies. However, magnetite as a predominant, primary iron oxide and the occurrence of metal sulfides (pyrite, pyrrhotite, chalcopyrite) below the oxide- and oxide–silicate BIF facies suggest that the redox state of the then deep ocean should be transitional from euxinic (anoxic, sulfidic) to anoxic but Fe^{2+}-rich conditions (e.g., Canfield, 1998). We also observed that the magnetite-rich oxide facies is intercalated locally with the sulfide–carbonate–silicate BIF facies (Fig. 7h). Nevertheless, the moderately negative correlations of Fe with HREE (Fig. 15f) for both the sulfide–carbonate–silicate ($R^2 = 0.69$) and the oxide- and oxide–silicate ($R^2 = 0.39$) BIFs cannot be fully explained by preferential adsorption of HREE into hydrothermally-derived ferrous oxyhydroxides and/or ferrous–cobaltiferous–cupriferous sulfohydrates.

Fig. 15. Variant diagrams of Zr vs. REE (a), Mn (b) and Ba (c), Mn vs. Th (d) and Fe (e), Fe vs. HREE (f), Mn vs. REE (g), and Cu vs. Co for the Shilu BIFs of various facies and interbedded host rocks. $R^2 = 0.41$ in (a) and $R^2 = 0.31$ in (g) are for all the analyzed samples, $R^2 = 0.28$ in (a), $R^2 = 0.16$ in (b), $R^2 = 0.58$ in (d), $R^2 = 0.22$ in (e), $R^2 = 0.20$ in (f), $R^2 = 0.47$ in (g), and $R^2 = 0.56$ in (h) for all the BIF facies, $R^2 = 0.47$ in (e), and $R^2 = 0.39$ in (f) for both the oxide- and silicate–oxide BIF facies, $R^2 = 0.58$ in (g) for the oxide BIF facies, $R^2 = 0.33$ in (g) for the silicate–oxide BIF facies, $R^2 = 0.13$ in (c), $R^2 = 0.53$ in (e), and $R^2 = 0.69$ in (f) for the sulfide–carbonate–silicate BIF facies, respectively.

Therefore, a hydrogenous component (e.g., Fe–Mn particles) which is suggested by the correlations of Zr with Y/Ho and REE, and of Mn with Th and REE (Figs. 11d and 15a, d, and g) was another control over the trivalent REY patterns. In summary, we invoke a submarine hydrothermal vent/plume origin for all the Shilu BIF facies, but suggest that the ferrous oxyhydroxides and/or ferrous–cobaltiferous–cupriferous sulfohydrates formed under euxinic to anoxic Fe^{2+}-rich conditions after oxygenation of the then deep ocean removed from the plume/vent, and then accumulated on the sea floor in a shallow marine, coastal environment, where Fe^{2+} was oxidized in clastic-starved setting (e.g., Rasmussen et al., 2012) and mixed or intercalated with terrigenous materials, resulting in our observed REY patterns.

6.6. Comparison with other BIFs and related Cu–Co deposits

BIFs between 3.2 Ga and 1.8 Ga are classified as either Algoma- or Superior-types (Huston and Logan, 2004). Algoma-type BIFs are generally small in size and associated with contemporaneous volcanic suites, whereas Superior-type BIFs (Hamersley-type in Australia) are laterally extensive, generally in a shelf environment with no volcanic association (Gross, 1980). The source of Fe and Si in these BIFs is typically attributed to: (a) anoxic weathering on continents, (b) volcanic exhalations from submarine volcanoes, (c) hydrothermal vent activity on the ocean floor within their depositional basins, or (d) hydrothermal leaching of the pre-existing sediments or deep ocean source (Adekoya, 1998; Khalil and El-Shazly, 2012). However, either the seafloor volcanic exhalative model or the hydrothermal vent model related to mantle plumes or hot spots would require that the BIFs (Algoma-type) should be intercalated with tholeiitic basalts (Adekoya, 1998; Isley and Abbott, 1999; Khalil and El-Shazly, 2012), which is not the case with the Shilu BIFs. Because the Shilu Group host rocks are a dominantly submarine siliciclastic and carbonate sedimentary succession, two principal possibilities exist, namely the hydrogeneous–sedimentary processes (Holland, 1973; James and Sims, 1973) and the hydrothermal exhalative processes (Gross, 1991; Kimberley, 1989), which have been proposed for the origin of and very large accumulations of Fe in the Superior-type BIFs, could be considered to interpret the formation of the Shilu BIFs (Xu et al., 2013). The geochemical and Nd isotopic features, in line with the petrographical evidences, strongly support the seafloor-derived, acidic and reducing hydrothermal solutions as a predominant source for the Shilu BIFs, though a variable input from weathered landmass is required. The Shilu BIFs also contain relatively high though variable abundances of Cu, Co, Zn, and/or As, Pb, Ni, V and Ba, and relatively low though variable of Zr content, when compared with the worldwide Superior-type BIFs (Adekoya, 1998; Horstmann and Hälbich, 1995). Together with the Fe–Co–Cu association, these imply that submarine volcanism likely is a source of the Shilu BIFs which were formed partly by volcanic exhalations and partly by hydrothermal leaching caused by seawater–hot lava interactions (Adekoya, 1998). Therefore, any model developed to explain the origin of the Shilu BIFs must consider their geochemical and Sm–Nd isotopic characteristics.

The Neoproterozoic BIFs also can be subdivided into Algoma and Rapitan-types (James, 1992), based on their intimate association with either volcanic or glaciogenic rocks (e.g., tillites, cap dolostones and diamictites). However, Young (2002) suggested that all the Neoproterozoic Rapitan-type BIFs associated with glaciogenic deposits favor deposition in a rift environment, although two schools have emerged to explain the types of BIFs. Many workers (e.g., Adekoya, 1998; Eyles and Januszczak, 2004; Freitas et al., 2011; Young, 2002) have also proposed a rift-related hydrothermal model to explain the occurrence of the Neoproterotozic Rapitan-type BIFs in isolated or restricted rift basins related to the breakup of Rodinia after 750 Ma. In contrast with the majority of the Neoproterozoic BIFs (Basta et al., 2011 and references therein), the Shilu district contains no evidence of either contemporaneous glaciation or volcanic rocks. Consequently, neither volcanic activity nor snowball earth condition could explain the buildup of dissolved Fe, Co and Cu for the Shilu district. On the other hand, the Shilu BIFs seems comparable to the Neoproterozoic Rapitan-type BIFs in both geochemical and Nd and C isotopic components. For example, the Neoproterozoic (ca. 750–700 Ma) BIFs in the eastern part of the Adelaide Geosyncline of South Australia are similar to the Shilu BIFs not only in PAAS-normalized REY patterns characterized by high though variable $\sum$REE contents and LREE depletion relative to HREE but also in almost negative $\delta^{13}C_{PDB}$ values (-5.5 to $+0.9$‰) for associated carbonates (Lottermoser and Ashley, 2000). It implies that hydrothermal exhalations added significant amounts of Fe and other metals to the then seawater, and that the Shilu BIFs of various facies were the result of chemical precipitation of dissolved Fe (and Co and Cu) during a postglacial, transgressive period and formed in a near-coastal environment under significant terrestrial influences (Lottermoser and Ashley, 2000). The characteristic Fe–Co–Cu association and older depositional age (ca. 1.0 to 0.83 Ga), unlike those in the Adelaide BIF, however, suggest that the Shilu BIFs are not Rapitan-type, in contrast, their formation should be prior to global glaciation.

The Neoproterozoic or temporally similar BIF-type deposits with associated stratabound or stratiform Cu and Cu–Co–Zn–Ni ore deposits have been reported in the Jingtieshan, Gansu Province of North China (Sun et al., 1998) and the Sykesville District, Maryland Piedmont (Candela et al., 1989). The Jingtieshan Fe–Si–Ba and Cu mineralization in North China, which is hosted by a suite of rift-type marine sediments of the Neoproterozoic Jingtieshan Formation comprising fine-grained clastic sedimentary rocks, andesitic basalts and carbonate rocks, is characterized by the upper Fe orebodies dominated by specularite and jasper with lesser amounts of magnetite, hematite, siderite, and barite, and the lower Cu orebodies composed of pyrite and chalcopyrite occurring as disseminated and stockwork mineralization (Sun et al., 1998). Sun et al. (1998) suggested that the Jingtieshan deposit belongs to Lake Superior-type and that the Fe orebodies formed from hydrothermal exhalative and chemical sedimentary processes on the floor of an ocean basin, and with the Cu mineralization formed by hydrothermal filling and replacement at the base of and within the iron formation. This genetic model seems feasible for the Shilu Fe–Co–Cu mineralization, however, it is not compatible with all the characteristic features including the Fe–Co–Cu association, hematite–quartz-dominated Fe ores and banded- or massive dominated Co–Cu ores in the Shilu district. The Cu–Co–Zn–Ni sulfide mineralization in the Sykesville district, likely related to the subduction a spreading center proximal to continental crust, occurs within the late Neoproterozoic to early Paleozoic (?) BIFs and chiefly consists of chalcopyrite with small amounts of siegenite, sphalerite, cobaltiferous pyrite, and bornite (Candela et al., 1989). Because the Fe-oxide (magnetite-dominated) + sulfide mineralizing zone occurs near the contact between ultramafic rocks of a sedimentary origin on the sea floor and metasediments of the melange, Candela et al. (1989) proposed that Co and Ni were derived from the ultramafic rocks during the highest temperature stage of a sea-floor hydrothermal event; Cu and Zn likely leached from underlying oceanic basalts; Fe from both; and sulfur (S) probably from basalts and seawaters. Despite a similar metal association of Fe–Cu–Co–Ni to the Sykesville district, the absence of mineralization-related ultramafic rocks and high Zn chromite, and the presence of As-rich Co–Cu ores, as well as the spatial correlation between Fe oxide- and Co–Cu mineralizations and the positive correlation of Cu with Co for all the Shilu BIF facies (Fig. 15h) strongly argue against the Shilu Fe–Co–Cu ore district being a "sedimentary–volcanogenic", Outokumpu-type deposit (cf. Peltola, 1977).

We also undertake a comparison in Co–Cu mineralization between the Shilu district and the Zambian Copperbelt of Africa to constrain origin of the Shilu Co–Cu ores. The Zambian Copperbelt occurs within a rift-related, Neproterozoic metasedimentary sequence of greenschist facies which unconformably overlies granites and other rocks of the basement complex, and is characterized by disseminated sulfide ores chiefly comprising chalcopyrite, bornite, and chalcocite with ore-grade

carrollite, cobaltiferous pyrite, and cobalt pentlandite in some deposits (Annels et al., 1983; Selley et al., 2005; Sweeney et al., 1986). Various genetic models such as epigenetic–magmatic to syn-sedimentary, diagenetic, and epigenetic–syn-orogenic have been proposed for the source of metals, origin and physiochemical nature of transporting fluids, sulfide precipitation mechanisms, and timing of mineralization in the Zambian Copper belt (El Desouky et al., 2010 and references therein). Because the distribution, geometry, and size of the sulfide ores are fundamentally controlled by synrift, subbasin fault architecture and by the availability of both in situ and mobile reductants, the distributions of which were probably also linked to basin structures, Selley et al. (2005) interpreted the Cu–Co sulfide ore formation as a result of multistage mineralization, which included diagenetic to late diagenetic, late diagenetic to early orogenic, and postmetamorphic vein-type due to metasomatism. Likewise, El Desouky et al. (2009, 2010) proposed two main hypogene mineralization models, namely an early diagenetic, typical stratiform hydrothermal model for the first Cu–Co stage and a multistage syn-orogenic stratiform to stratabound hydrothermal model for the second stage, to delineate the formation of the Luiswishi and Kamoto sediment-hosted stratiform Cu–Co ore deposits in the Katangan Copperbelt, central African. However, the characteristic features of banded or massive Co–Cu ores and the fact of the occurrence of the Fe oxide BIF facies, which are absent from the Zambian Copperbelt, suggest the origin of the Shilu district is not related to diagenetic processes. This is supported by the fact that the Shilu Co–Cu sulfides have $\delta^{34}S_{CDT}$ values ranging from +11.1 to 17.5‰ (average +15.97‰; Xu et al., 2009), comparable to a mean $\delta^{34}S$ value of +17.5‰ ± 3‰ for Neoproterozoic seawater at the time of deposition of the Shilu Group, but distinctly different from those of the Zambian Copperbelt (El Desouky et al., 2010; Sweeney et al., 1986). Nevertheless, the previous study (Xu et al., 2013) has indicated that the tectonic, metamorphic and hydrothermal reworking which most likely was related to the multistage orogenies in South China has significantly modified the Shilu district resulting in enrichment and upgrading of Fe- and Co–Cu ores and secondary mineralization. A similar phenomena also has been described and explained in some Co–Cu–Au ore deposits related to BIFs in the Werner Lake of Canada (Pan and Therens, 2000) and the Idaho cobalt belt of northwestern United States (Nold, 1990).

6.7. Origin and depositional setting

Many researchers have discovered that some deep-ocean volcanogenic massive sulfide (VMS) deposits have associated chemical sediments including BIFs (e.g., Bekker et al., 2010; Huston et al., 2010; Rasmussen et al., 2012; Slack et al., 2007). The occurrences of BIFs surrounding VMS systems confirm that the hydrothermal systems which generate VMS deposits emit large volumes of dissolved Fe and other metals Cu and Co into the deep ocean (Rasmussen et al., 2012) and that there is a strong correlation between mantle plume activity and the deposition of BIFs related to VMS deposits (Bekker et al., 2010; Isley and Abbott, 1999). Despite an absence of volcanic association in the Shilu Group, Lu (1988) and Fang et al. (1992) reported the possible presence of bimodal volcanic rocks in the Shilu district, including spilites and tholeiites which show affinities to OIB- and N-MORB-type basalts (Fang et al., 1992). The analogous magmatism has been found in modern rifting tectonic settings, e.g., in Red Sea–Afar region (Bonatti et al., 1972). If this is the case, the origin of the Shilu BIFs could be linked to mantle superplume volcanism (Isley and Abbott, 1999). This suggestion might have been supported by the fact that the Rodinia break-up due to mantle activity at ca. 860–800 Ma is marked by widespread rift-type bimodal magmatism in South China (e.g., Li et al., 1999, 2002c, 2003, 2010; Shu et al., 2011; Wang and Li, 2003). Because of the absence of associated VMS deposits and also a possible presence of the coeval rift-type volcanics, we propose that the precursors to the Shilu BIFs had been derived from a distal or deeper seafloor source which likely was related to the Rodinia break-up due to mantle activity in South China. The sea floor-derived hydrothermal fluids that brought Fe, Si, Co and Cu onto a shallow marine, restricted or sheltered basin near the rifted continental margin mixed with detrital components from seawater and fresh water carrying continental landmass, which finally led to the deposition of the Shilu BIFs.

However, the present petrographical and mineralogical observations as well as the previous results (Xu et al., 2013) demonstrates that the ores in the Shilu district are zoned from bottom to top: banded sulfide (cobaltiferous pyrite/pyrrhotite + chalcopyrite)-dominated Co–Cu ores with disseminated, stockwork and brecciated sulfide mineralization → banded Fe oxide (magnetite, hematite)–calc-silicate (garnet, epidote, amphibole, pyroxene) ores → banded (hematite + quartz) Fe oxide-ores with veinlet sulfide mineralization. Moreover, as shown by Fig. 13, there are hyperbolic trends in Co, Cu, Ni, and Fe components for the Shilu BIFs. These trends in composition have likely been caused either by a different source region with respect to hydrothermal fluids and terrigenous components or by fluctuation in redox state in the same or similar source area components. Current models on the origin of BIFs suggest that pulsed output from distal mid-ocean-ridge settings or hotspots was the major source of Fe, Si and the metals Co, Cu and Ni (e.g., Jacobsen and Pimentel-Klose, 1988a,b; Morris and Horwitz, 1983), likely supplemented by normal continental drainage (e.g., Canfield, 1998). Linked to the geochemical and Sm–Nd isotopic characteristics as well as the suggested depositional setting, the compositional trends for the Shilu BIFs can be ascribed to both the change in hydrothermal fluid components due to periodic pulses of the submarine hydrothermal plume fluids and variable input of detrital components, and the fluctuation in redox state, resulting in alternating deposition of the Fe oxide-rich layers with the metal sulfide-rich layers. Thus the presence of the zoned ores suggests that the deep ocean mainly providing metalliferous hydrothermal fluids for the precursors to the Shilu BIFs in the continental shelves might have shown a fluctuation in redox state (Anbar and Knoll, 2002; Planavsky et al., 2011) from original euxinic (anoxic and sulphidic) condition for deposition of the sulfide–carbonate–silicate facies BIFs in basinal bottom section to terminal ferruginous (anoxic and Fe^{2+}-rich) condition for the oxide- and oxide–silicate facies ones in basinal upper section.

7. Conclusions

Based on the geological and petrographical investigation as well as the geochemical and isotopic analysis, three facies types of metamorphosed BIFs have been identified in the Shilu Fe–Co–Cu ore district. These include: the oxide-, the silicate–oxide- and the sulfide–carbonate–silicate BIF facies. The oxide BIF facies, i.e. the quartz itabirites or Fe-rich ores, is high in Fe_{tot} (FeO + Fe_2O_3; more than 69 wt.%), and comprises alternating hematite-rich microbands with quartz-rich microbands. The silicate–oxide BIF facies, i.e. the amphibolitic itabirites or Fe-poor ores, is relatively low in Fe_{tot} (22–63 wt.%) and comprise alternating centimeter- to a few tens meter-scale Fe oxide (hematite, magnetite)-rich bands with millimeter- to centimeter-scale calc-silicate (garnet, pyroxene, amphibole, epidote)-rich bands. The sulfide–carbonate–silicate BIF facies, i.e., the Co–Cu ores, has a Fe_{tot} content generally ranging from 17 to 85 wt.% and shows alternating metal sulfide (cobaltiferous pyrite/pyrrhotite, chalcopyrite) macro- to microbands mainly with equal-scale dolomite + calcite ± amphibole ± pyroxene, minor with sericite + quartz bands. These BIF facies, which are intercalated within the low- to medium-grade, dominantly submarine metamorphosed siliciclastic and carbonate sedimentary succession of the Neoproterozoic Shilu Group, are characterized by the blastooolitic, blastopelletoid and blastocolloidal structures, and blastopsammitic and cryptocrystalline to microcrystalline textures, which most likely represent primary sedimentation.

Major- and trace element (including REE), and Sm–Nd isotopic geochemical data have been used to evaluate the source areas and to reconstruct the depositional settings of the Shilu metamorphosed BIFs. We propose that the precursors to the Shilu BIFs have been derived

predominantly from seafloor-derived, pulsed high- to low-*T* (temperature) hydrothermal plume/vent fluids which likely were associated with the break-up of the Rodinian supercontinent due to mantle superplume activity in South China. Variable input of detrital components largely from an unknown, Paleoproterozoic or older crystalline basement with lesser input from Paleo- to Mesoproterozoic arc-related rocks is required. In line with the facies zonation from the lower sulfide–carbonate–silicate BIF facies to the upper oxide–silicate- and oxide BIF facies, a shallow marine, sheltered or restricted basin near the rifted continental margin is considered for deposition of the Shilu BIFs and interbedded host rocks. In such the basin, seafloor-derived, periodically upwelling metalliferous hydrothermal vent fluids formed under anoxic but sulfidic to anoxic but Fe^{2+}-rich conditions variably mixed with terrigenous detrital components and then were oxidized by oxygenized water, which finally led to alternating deposition of the Shilu BIFs, from basinal bottom to upper sections.

Acknowledgments

This paper is financially co-supported by the State Key Fundamental Program (2012CB416806) and GIGCAS 135 Project Y234141A07. We would like to thank Prof. Guo Fengfang from Hainan Mining Cooperation Limited Company and Prof. Liu Zhaolu from Hainan Bureau of Geology for their support during the regional geological survey. A particular thank is given to Prof. David Huston and another anonymous reviewer as well as to editors Profs. Franco Pirajno, Zhaocong Zhang and Jianwei Li, for their constructive suggestions to improve the quality of this paper.

Appendix A

Appendix A1
Major element contents (wt.%) of both the pyroxene–amphibole rocks and banded or impure dolostones in the Shilu Fe–Co–Cu ore district, Hainan Province of South China.

Sample	Lithology	SiO_2	TiO_2	Al_2O_3	Fe_2O_3	FeO	MnO	MgO	CaO	Na_2O	K_2O	P_2O_5	Total	LOI	Fe_{tot}
SL6-1-2	Pyroxene–amphibole-rich rocks	52.16	0.51	10.01	2.67		0.10	14.63	16.89	0.08	2.87	0.08	100.00	3.08	2.67
SL6-2		56.55	0.55	5.98	2.64		0.13	11.96	17.60	0.13	4.39	0.06	100.00	1.88	2.64
ZSL6-7		57.28	0.55	9.58	2.39		0.11	9.21	15.20	0.21	5.41	0.07	100.00	5.90	2.39
ZSL6-21		56.40	0.54	4.59	3.61		0.19	12.04	19.05	0.15	3.35	0.07	100.00	1.73	3.61
ZSL6-15		51.86	0.32	4.03	5.73		0.32	15.07	21.51	0.30	0.81	0.06	100.00	5.24	5.73
ZSL6-21-1		56.25	0.60	11.20	3.32		0.12	10.40	12.55	0.42	5.05	0.08	100.00	2.23	3.32
ZSL6-22		50.81	0.54	11.26	3.96		0.12	10.79	22.08	0.09	0.26	0.08	100.00	3.55	3.96
BY-034		67.25	0.62	9.32	7.43		0.08	6.10	6.63	0.24	2.25	0.08	100.00	3.45	7.43
BY-116		57.84	0.56	9.18	7.33		0.70	3.56	16.23	0.12	4.39	0.09	100.00	6.43	7.33
F8-07		60.80	0.45	7.46	2.59		0.10	10.02	14.62	0.17	3.72	0.07	100.00	3.71	2.59
Si3[a]		53.70	0.52	7.06	2.35	2.19	0.15	11.33	19.14	0.92	2.56	0.07	100.00	4.26	4.55
Si7[a]		54.61	0.38	7.76	4.04	1.43	0.11	10.64	17.00	1.09	2.87	0.07	100.00	5.54	5.47
G-3[a]		51.50	0.39	5.28	1.18	3.07	0.17	15.26	21.21	0.15	1.71	0.09	100.00	8.80	4.24
412-38[a]		51.61	0.49	8.75	0.26	3.34	0.22	13.64	19.00	0.43	2.18	0.09	100.00	6.54	3.60
400-11[a]		51.80	0.64	11.06	3.08	1.10	0.10	13.44	14.30	0.36	4.02	0.11	100.00	5.94	4.18
400-18[a]		51.22	0.55	9.88	1.91	3.32	0.25	12.31	16.83	0.23	3.38	0.12	100.00	5.21	5.23
HbO52[a]		58.65	0.66	8.26	1.56	5.34	0.18	8.94	10.14	0.13	6.06	0.06	100.00	1.05	6.90
Hb52-1[a]		57.81	0.64	11.22	1.73	5.39	0.24	8.38	10.19	0.45	3.85	0.10	100.00	0.88	7.12
G13[a]		58.01	0.47	6.87	4.26	1.88	0.18	8.21	17.23	0.32	2.50	0.07	100.00	2.55	6.15
Si4[a]		59.98	0.65	6.80	2.23	1.76	0.15	10.08	13.82	1.15	3.31	0.07	100.00	4.11	3.99
Si8[a]		58.63	0.45	5.08	2.87	2.14	0.12	10.54	16.30	1.97	1.83	0.06	100.00	1.91	5.01
355-204[a]		60.02	0.67	12.41	3.26	3.03	0.16	6.25	8.59	0.31	5.10	0.20	100.00	1.80	6.29
400-10[a]		60.89	0.68	14.13	1.30	7.26	0.12	3.96	3.29	0.23	8.03	0.11	100.00	5.00	8.56
Si5[a]		56.45	0.55	10.53	1.35	4.57	0.40	5.89	13.52	1.95	4.69	0.09	100.00	1.49	5.92
412-74[a]		54.38	0.49	8.47	0.90	3.09	0.24	13.13	15.75	0.36	3.09	0.10	100.00	3.43	3.99
Hb0522[a]		55.32	0.62	10.82	1.23	4.65	0.29	9.54	12.44	0.45	4.53	0.11	100.00	1.66	5.88
400-13[a]		64.46	0.62	11.05	1.31	2.16	0.14	6.88	8.23	0.30	4.75	0.10	100.00	4.06	3.46
SL26	Banded or impure dolostones	0.36	0.00	<0.001	0.24		0.07	22.51	30.21	0.06	0.00	0.03	100.25	46.77	0.24
ZSL6-29		3.93	0.02	0.32	0.61		0.12	21.27	29.70	0.02	0.03	0.10	99.78	43.66	0.61
F8-12		1.19	0.04	0.40	2.65		0.18	22.08	29.17	0.02	0.01	0.03	99.42	43.65	2.65
ZSL6-32		5.28	0.06	1.25	1.56		0.23	19.89	29.59	<0.2	0.03	0.09	99.55	41.57	1.56

Fe_{tot} expressed as Fe_2O_3 + FeO.
[a]Sample from SCISTCAS (1986).

Appendix A2
Trace- and REE element contents (ppm) of both the pyroxene–amphibole-rich rocks and banded or impure dolostones in the Shilu Fe–Co–Cu ore district, Hainan Province of South China.

Sample	By034	By116	F8-07	SL6-1-2	ZSL6-15	ZSL6-21-1	ZSL6-22	SL6-2	ZSL6-7	ZSL6-21	ZSL6-29	F8-12	SL26
Lithology	Pyroxene–amphibole-rich rocks										Banded or impure dolostones		
Sc	10.30	8.37	8.60	9.37	3.72	10.59	9.55	5.18	8.44	4.95	0.60	3.61	0.90
Ti	3106	2878	2412	2954	1839	3566	3278	3284	3149	3184	95	228	9
V	58.80	56.40	53.15	68.78	46.09	70.39	65.49	36.01	47.37	39.44	7.85	7.30	7.51
Cr	33.86	32.47	26.44	35.60	13.12	40.82	37.15	21.72	29.16	17.86	5.88	5.60	3.00
Mn	683	5748	867	903	2634	1137	1099	1203	958	1720	863	1346	561

Appendix A2 (*continued*)

Sample	By034	By116	F8-07	SL6-1-2	ZSL6-15	ZSL6-21-1	ZSL6-22	SL6-2	ZSL6-7	ZSL6-21	ZSL6-29	F8-12	SL26
Lithology	Pyroxene–amphibole-rich rocks										Banded or impure dolostones		
Co	10.34	9.93	20.45	6.89	17.14	13.96	11.49	10.14	26.27	38.73	1.12	12.02	0.89
Ni	16.84	15.29	18.21	11.56	10.72	10.96	10.53	12.62	15.16	51.63	6.01	15.98	5.62
Cu	229.10	4.83	31.54	7.75	1182	19.49	92.32	3.13	84.40	21.87	0.50	153.20	7.12
Zn	14.95	27.85	26.31	32.30	41.09	30.72	25.38	42.49	22.33	30.95	25.16	21.28	9.94
Ga	12.04	11.51	10.57	11.58	6.90	12.46	20.92	4.92	11.37	4.43	0.60	1.73	0.08
Ge	6.10	0.60	2.59	1.78	2.15	1.72	2.20	1.84	3.02	2.50	0.13	0.13	0.01
Rb	72.38	102.10	144.60	221.20	45.91	151.60	9.45	123.90	151.90	90.19	2.15	1.02	0.40
Sr	130.70	68.60	66.23	46.95	22.71	147.60	28.74	44.07	173.20	63.47	61.76	105.60	185.10
Y	31.82	23.76	20.08	17.23	17.83	26.35	27.80	28.55	27.16	27.17	5.02	3.23	1.79
Zr	242.30	96.75	128.40	117.00	241.70	171.90	225.40	342.70	170.50	286.90	4.78	10.87	0.68
Nb	10.75	9.20	7.99	9.25	5.90	11.13	10.31	9.90	9.58	9.23	0.44	1.04	0.05
Ba	516	2433	6440	6271	248	5322	170	3040	7121	6107	30.25	225	2.88
La	25.35	26.45	20.59	25.62	13.72	35.39	30.44	11.46	16.52	6.10	2.68	3.37	1.28
Ce	54.96	55.69	43.51	54.50	30.68	73.13	67.05	37.38	44.29	26.97	3.90	8.59	1.96
Pr	6.80	7.04	5.42	6.69	3.94	8.90	8.38	5.83	6.94	4.93	0.62	1.19	0.30
Nd	24.49	26.04	20.21	23.57	14.85	31.77	30.15	23.64	30.07	21.56	2.38	5.04	1.10
Sm	5.37	5.21	4.44	4.24	3.38	5.95	6.00	5.33	8.68	5.86	0.48	1.65	0.23
Eu	1.24	1.00	1.03	0.97	0.74	1.11	1.13	1.00	2.38	1.22	0.14	0.55	0.06
Gd	5.96	4.90	4.23	3.85	3.53	5.53	5.69	5.18	7.59	5.58	0.58	1.61	0.24
Tb	0.99	0.75	0.65	0.55	0.55	0.80	0.88	0.88	1.05	0.88	0.08	0.17	0.03
Dy	5.87	4.36	3.80	3.21	3.07	4.78	5.08	5.19	5.43	5.10	0.52	0.64	0.18
Ho	1.17	0.90	0.77	0.67	0.60	0.98	1.04	1.09	1.02	1.03	0.12	0.11	0.04
Er	3.36	2.49	2.23	1.91	1.77	2.83	2.95	3.10	2.81	2.86	0.32	0.27	0.11
Tm	0.48	0.36	0.32	0.30	0.26	0.41	0.43	0.46	0.41	0.40	0.05	0.04	0.02
Yb	3.19	2.29	2.11	1.90	1.72	2.69	2.81	3.03	2.71	2.70	0.26	0.25	0.10
Lu	0.46	0.34	0.30	0.28	0.26	0.40	0.42	0.46	0.39	0.42	0.04	0.03	0.02
Hf	6.36	2.69	3.36	3.01	5.72	4.38	5.64	8.73	4.71	7.23	0.10	0.26	0.01
Ta	0.90	0.72	0.60	0.74	0.41	0.90	0.80	0.72	0.77	0.68	0.03	0.07	0.01
Pb	10.72	11.16	5.39	2.92	12.37	9.31	10.79	6.34	7.85	11.46	5.03	2.49	1.20
Th	12.44	10.07	7.20	9.23	6.01	12.03	11.90	9.81	9.34	8.18	0.45	1.08	0.03
U	2.46	2.37	1.74	3.76	1.65	2.45	2.47	2.55	3.44	2.38	0.81	0.91	0.10
Rb/Sc	7.03	12.20	16.81	23.61	12.34	14.32	0.99	23.92	18.00	18.22	3.58	0.28	0.44
Th/Sc	1.21	1.20	0.84	0.99	1.62	1.14	1.25	1.89	1.11	1.65	0.75	0.30	0.03
δEu_{PAAS}	1.02	0.92	1.10	1.12	1.00	0.90	0.90	0.88	1.37	0.99	1.24	1.57	1.13
δCe_{PAAS}	0.96	0.93	0.94	0.95	0.96	0.94	0.96	1.05	0.95	1.13	0.69	0.98	0.73
La/Yb_{PAAS}	0.58	0.85	0.72	1.00	0.59	0.97	0.80	0.28	0.45	0.17	0.75	1.01	0.95
La/Sm_{PAAS}	0.70	0.75	0.68	0.89	0.60	0.88	0.75	0.32	0.28	0.15	0.83	0.30	0.83
Gd/Yb_{PAAS}	1.11	1.28	1.19	1.21	1.22	1.22	1.20	1.02	1.67	1.23	1.30	3.89	1.43
Pr/Sm_{PAAS}	0.80	0.86	0.77	1.00	0.74	0.95	0.89	0.69	0.51	0.53	0.83	0.46	0.82
Sm/Yb_{PAAS}	0.84	1.14	1.05	1.12	0.98	1.11	1.07	0.88	1.60	1.09	0.90	3.34	1.15
Gd*	1.07	1.09	1.09	1.12	1.11	1.12	1.08	1.02	1.13	1.07	0.98	0.97	0.97
Pr*	1.06	1.06	1.05	1.07	1.06	1.06	1.07	1.12	1.09	1.17	1.16	1.04	1.15
Y/Ho	27.17	26.28	26.08	25.91	29.72	26.83	26.81	26.19	26.73	26.51	43.66	29.60	44.78
∑REE	139.69	137.82	109.60	128.25	79.07	174.66	162.45	104.02	130.29	85.59	12.15	23.51	5.65

Y content is not included in ∑REE. $(Eu/Eu^*)_{PAAS} = (Eu/Eu_{PAAS}) / ((Sm/Sm_{PAAS}) \times (Gd/Gd_{PAAS}))^{1/2}$, $(Ce/Ce^*)_{PAAS}$ and $(Pr/Pr^*)_{PAAS}$ calculated by similar way. $Gd^* = Gd_{PAAS} / (0.33 \times Sm_{PAAS} + 0.67 \times Tb_{PAAS})$ after Frimmel (2009).

Appendix A3
Major element contents (wt.%) of both the quartz- and amphibolitic itabirites in the Shilu Fe–Co–Cu ore district, Hainan Province of South China.

Sample	Lithology	SiO_2	TiO_2	Al_2O_3	Fe_2O_3	FeO	MnO	MgO	CaO	Na_2O	K_2O	P_2O_5	Total	LOI	Fe_{tot}	$Fe^{\#}$
BY-012	Quartz itabirites	26.27	0.02	0.44	68.60	2.98	0.01	0.37	1.11	0.13	0.03	0.03	100.00	1.19	71.58	0.95
By-113		12.85	0.15	1.56	64.34	17.73	0.11	0.75	1.99	0.15	0.26	0.10	100.00	1.14	82.07	0.77
ZSL6-5		18.40	0.12	0.61	78.77	1.28	0.01	0.06	0.51	0.10	0.04	0.09	100.00	0.15	80.05	0.98
ZSL6-10		10.16	0.11	0.96	84.10	3.67	0.07	0.16	0.52	0.14	0.05	0.04	100.00	0.50	87.78	0.95
ZSL6-27		28.08	0.08	0.98	69.00	0.81	0.01	0.08	0.70	0.14	0.05	0.06	100.00	0.51	69.81	0.99
ZSL6-30		29.15	0.07	0.20	67.50	2.20	0.02	0.09	0.52	0.12	0.04	0.08	100.00	0.35	69.70	0.97
By-109	Amphibolitic itabirites	28.59	0.25	5.24	39.50	15.22	0.38	1.48	7.76	0.15	1.35	0.07	100.00	1.75	54.72	0.70
By-111		42.67	0.65	8.95	16.30	6.58	1.18	3.52	16.47	0.18	3.40	0.11	100.00	3.30	22.88	0.69
SL-31		58.34	0.06	0.58	28.78	1.85	0.11	0.12	9.83	0.10	0.03	0.19	100.00	1.41	30.64	0.93
SL-32		41.78	0.11	0.87	37.38	14.56	0.07	0.24	4.74	0.09	0.03	0.13	100.00	0.91	51.93	0.70
ZSL6-8		41.37	0.15	7.61	29.47	2.19	0.72	1.12	15.48	0.14	1.68	0.06	100.00	1.26	31.66	0.92
ZSL6-9		31.18	0.12	2.26	50.80	11.23	0.08	0.37	3.07	0.12	0.72	0.04	100.00	0.67	62.03	0.80
ZSL6-14		47.83	0.07	1.24	28.22	8.79	0.71	0.81	12.13	0.10	0.08	0.02	100.00	1.86	37.01	0.74
ZSL6-19		56.13	0.14	2.77	28.06	5.62	0.17	1.54	4.56	0.12	0.76	0.16	100.00	1.67	33.67	0.82

$Fe^{\#} = Fe^{3+} / (Fe^{3+} + Fe^{2+})$.

Appendix A4

Trace- and REE element contents (ppm) of both the quartz- and amphibolitic itabirites in the Shilu Fe–Co–Cu ore district, Hainan Province of South China.

Sample	By-113	ZSL6-10	By-012	ZSL6-5	ZSL6-27	ZSL6-30	By-109	By-111	SL31	SL32	ZSL6-8	ZSL6-9	ZSL6-14	ZSL6-19
Lithology	Quartz itabirites						Amphibolitic itabirites							
Sc	3.22	1.23	0.55	0.16	0.82	0.10	6.00	9.84	0.25	0.20	5.35	2.74	0.59	3.73
Y	9.49	5.78	1.77	1.21	3.68	1.32	22.60	34.90	7.74	2.69	22.90	15.00	8.19	21.80
La	7.60	3.05	0.53	0.44	3.26	0.27	17.60	42.30	5.26	0.55	19.50	12.00	3.60	16.00
Ce	16.90	7.80	2.25	2.38	8.42	2.23	41.60	93.30	11.00	2.95	40.40	26.00	11.20	41.60
Pr	1.94	0.85	0.19	0.17	0.93	0.17	4.24	9.28	1.03	0.23	4.13	3.03	1.48	4.13
Nd	8.40	3.83	1.27	0.84	4.11	0.92	18.70	36.53	4.20	1.19	17.56	12.84	6.58	18.29
Sm	1.76	0.91	0.54	0.09	0.77	0.22	4.39	6.51	0.89	0.34	3.95	2.53	1.28	4.36
Eu	0.39	0.19	1.40	0.10	2.04	0.26	1.81	2.25	0.22	0.11	1.47	0.52	0.38	1.62
Gd	2.12	1.18	0.71	0.11	0.97	0.32	5.27	7.06	1.42	0.58	4.94	2.81	1.41	4.97
Tb	0.35	0.21	0.08	0.03	0.17	0.05	0.82	1.10	0.26	0.09	0.81	0.46	0.21	0.76
Dy	2.06	1.19	0.40	0.19	0.68	0.28	4.52	6.55	1.43	0.50	4.60	2.77	1.25	4.18
Ho	0.39	0.22	0.05	0.03	0.11	0.04	0.89	1.38	0.26	0.08	0.90	0.53	0.24	0.80
Er	1.14	0.62	0.19	0.14	0.35	0.15	2.40	4.17	0.81	0.24	2.51	1.59	0.65	2.13
Tm	0.18	0.09	0.03	0.03	0.06	0.03	0.35	0.68	0.11	0.04	0.39	0.24	0.10	0.31
Yb	1.06	0.57	0.21	0.18	0.39	0.16	2.14	4.19	0.73	0.30	2.20	1.39	0.54	1.71
Lu	0.16	0.09	0.04	0.03	0.07	0.03	0.31	0.62	0.12	0.05	0.32	0.20	0.08	0.25
Hf	5.10	2.55	0.61	0.72	1.87	0.54	3.42	5.33	0.83	0.94	3.32	2.26	0.56	1.10
Ta	0.08	0.06	0.04	0.05	0.04	0.04	0.14	0.33	0.06	0.10	0.17	0.11	0.04	0.10
Ag	0.07	0.03	0.02	0.04	0.02	0.03	0.03	0.05	0.05	0.06	0.09	0.12	0.04	0.02
Th	2.00	5.30	2.00	2.00	2.00	2.10	6.70	11.20	2.00	2.20	10.90	4.70	2.00	6.00
U	1.62	0.93	0.63	0.58	0.42	1.00	2.25	1.96	0.61	0.64	2.57	2.35	1.00	2.25
Pb	21.60	15.10	18.70	11.20	22.60	27.40	14.00	18.40	8.00	10.20	224.50	13.40	10.80	10.00
Zn	4.00	4.00	4.00	4.00	4.00	4.00	5.50	11.90	4.00	5.00	5.60	4.00	7.80	8.00
Cu	16.90	20.10	20.40	74.10	55.20	514.50	17.00	9.30	40.80	1751.00	15.30	20.00	18.80	12.70
Cr	22.00	19.70	18.20	22.60	15.50	13.80	33.70	52.20	26.40	27.50	52.70	33.10	17.40	38.90
Co	594	661	389	507	333	351	240	60	100	214	96	327	111	97
Ni	16.10	13.00	11.50	11.50	27.20	34.20	16.50	17.10	12.70	7.60	21.50	14.30	13.20	22.00
V	46.9	31.2	320	42.5	1194	1293	195	139	12.80	13.70	220	76.6	29.8	434
As	5.70	5.05	10.20	17.00	3.50	3.25	12.20	8.35	0.00	24.80	0.00	13.00	42.30	5.65
Rb	10.00	10.00	10.00	10.00	10.00	10.00	40.60	80.20	10.00	10.00	49.20	21.70	10.00	21.20
Sr	32.30	10.80	475.50	11.40	3260	3829	122.90	124.70	26.50	28.00	154.60	46.70	17.60	951.50
Ba	403	51.7	35,905	153	135,269	145,895	8500	9746	362	576	16,020	880	371	40,275
Mn	822	541	80	83	10	12	2448	5817	689	502	3502	593	3685	993
Nb	1.70	1.70	1.30	1.70	0.80	2.00	6.50	12.90	1.30	4.60	8.40	3.00	1.00	5.20
Zr	49.70	150.20	2.00	54.20	2.00	2.00	64.20	217.10	124.20	246.50	96.00	192.70	32.30	137.20
Rb/Sc	3.11	8.13	18.18	62.50	12.20	100.00	6.77	8.15	40.00	50.00	9.20	7.92	16.95	5.68
Th/Sc	0.62	4.31	3.64	12.50	2.44	21.00	1.12	1.14	8.00	11.00	2.04	1.72	3.39	1.61
δEu_{PAAS}	0.94	0.86	10.62	4.62	11.07	4.59	1.76	1.55	0.93	1.12	1.55	0.91	1.31	1.62
δCe_{PAAS}	1.01	1.11	1.65	2.02	1.11	2.41	1.10	1.08	1.08	1.90	1.03	0.99	1.11	1.17
La/Yb_{PAAS}	0.53	0.39	0.19	0.18	0.62	0.13	0.61	0.74	0.53	0.14	0.65	0.64	0.50	0.69
La/Sm_{PAAS}	0.64	0.49	0.15	0.73	0.63	0.19	0.59	0.96	0.87	0.24	0.73	0.70	0.42	0.54
Gd/Lu_{PAAS}	1.25	1.22	1.84	0.32	1.26	1.16	1.57	1.04	1.13	1.19	1.43	1.29	1.70	1.85
Gd/Yb_{PAAS}	1.19	1.23	2.00	0.36	1.49	1.19	1.47	1.00	1.16	1.16	1.33	1.21	1.57	1.73
Pr/Sm_{PAAS}	0.70	0.59	0.22	1.18	0.77	0.49	0.61	0.90	0.73	0.43	0.66	0.76	0.74	0.60
Sm/Yb_{PAAS}	0.83	0.80	1.28	0.25	0.99	0.68	1.03	0.78	0.61	0.56	0.90	0.91	1.19	1.27
Gd*	1.10	1.05	1.49	0.87	1.06	1.16	1.16	1.12	1.08	1.25	1.12	1.10	1.15	1.15
Pr*	0.93	0.89	0.63	0.67	0.91	0.67	0.87	0.91	0.86	0.70	0.89	0.95	0.99	0.86
Y/Ho	24.15	26.39	34.04	39.03	33.15	31.43	25.48	25.31	29.54	32.02	25.47	28.09	33.98	27.35
$\sum$REE	44.44	20.80	7.87	4.76	22.32	5.11	105.04	215.91	27.74	7.25	103.67	66.90	28.99	101.08

Y content is not included in $\sum$REE. $(Eu/Eu^*)_{PAAS} = (Eu/Eu_{PAAS}) / ((Sm/Sm_{PAAS}) \times (Gd/Gd_{PAAS}))^{1/2}$, $(Ce/Ce^*)_{PAAS}$ calculated by similar way.
Calculated ratios of δEu_N and La/Yb_N based on normalization REE values of C1-Chondrite in Sun and McDonough (1989), $\delta Eu_N = Eu_N / (Sm_N + Gd_N)^{1/2}$.

Appendix A5

Major element contents (wt.%) of the Co–Cu ores in the Shilu Fe–Co–Cu ore district, Hainan Province of South China.

Sample	SiO_2	Al_2O_3	TiO_2	Fe_2O_3	FeO	CaO	MgO	K_2O	Na_2O	MnO	P_2O_5	Total	LOI	Fe_{total}	$Fe^{\#}$
F4-05	0.82	0.03	0.81	75.17	9.04	0.07	5.93	7.49	0.21	0.05	0.38	100.00	21.72	84.21	0.94
F8-06	53.46	0.09	0.59	42.75	2.26	0.01	0.23	0.31	0.13	0.05	0.13	100.00	20.18	45.01	0.97
F9-04	35.33	0.06	0.79	6.13	2.65	0.16	22.21	32.31	0.21	0.04	0.12	100.00	15.45	8.78	0.81
F9-09	69.43	0.12	1.86	12.74	5.08	0.05	6.18	4.31	0.09	0.02	0.10	100.00	8.28	17.82	0.82
F9-11	50.73	0.13	1.86	25.90	9.69	0.06	5.73	5.39	0.11	0.26	0.12	100.00	14.88	35.60	0.83
N14-09	16.46	0.05	0.79	40.40	28.55	0.04	8.35	5.06	0.18	0.06	0.06	100.00	15.29	68.95	0.72
N14-10	9.69	0.06	0.89	30.65	53.39	0.01	4.24	0.74	0.19	0.06	0.09	100.00	30.06	84.04	0.51
N20-11	29.79	0.08	0.93	33.70	34.88	0.01	0.16	0.23	0.13	0.05	0.04	100.00	21.02	68.57	0.63
N21-10	16.01	0.11	2.83	74.06	3.22	0.02	1.56	1.92	0.11	0.04	0.11	100.00	29.03	77.28	0.98

$Fe^{\#} = Fe^{3+} / (Fe^{3+} + Fe^{2+})$.

Appendix A6
Trace- and REE element contents (ppm) of the Co–Cu ores in the Shilu Fe–Co–Cu ore district, Hainan Province of South China.

Sample	F4-05	F9-04	F9-09	F9-11	N14-09	N20-11	N21-10	N14-10	F8-06
Sc	0.39	1.85	3.45	3.53	1.33	0.40	0.26	0.99	0.17
Y	1.02	4.32	5.18	6.97	1.39	1.04	1.75	0.79	2.05
La	0.61	2.60	5.35	4.55	1.12	3.95	4.70	0.47	3.07
Ce	2.84	6.72	12.40	10.80	4.05	9.84	10.50	2.95	7.57
Pr	0.230	0.744	1.382	1.229	0.432	1.154	1.148	0.256	0.835
Nd	1.345	3.826	6.281	5.671	2.325	5.121	5.063	1.465	3.739
Sm	0.421	1.448	1.451	1.361	0.631	1.044	0.925	0.313	0.731
Eu	0.122	0.544	0.370	0.414	0.134	0.200	0.132	0.039	0.105
Gd	0.474	1.521	1.496	1.640	0.471	0.563	0.600	0.204	0.531
Tb	0.044	0.173	0.202	0.242	0.055	0.040	0.059	0.021	0.062
Dy	0.187	0.809	1.033	1.372	0.269	0.197	0.307	0.126	0.404
Ho	0.024	0.136	0.200	0.261	0.036	0.026	0.061	0.014	0.065
Er	0.099	0.413	0.591	0.799	0.151	0.134	0.208	0.085	0.250
Tm	0.014	0.064	0.100	0.109	0.030	0.023	0.043	0.019	0.044
Yb	0.101	0.399	0.677	0.741	0.180	0.182	0.293	0.132	0.275
Lu	0.017	0.062	0.105	0.112	0.032	0.031	0.046	0.022	0.055
Hf	0.759	0.752	1.984	1.848	1.989	0.885	1.109	2.310	0.728
Ta	0.035	0.034	0.063	0.066	0.039	0.034	0.047	0.037	0.032
Ag	2.28	12.40	516	14.70	4.06	2.75	4.55	3.98	27.60
Th	2.0	2.0	2.0	2.0	2.0	2.4	2.0	2.0	4.6
U	0.31	0.45	0.59	0.88	0.49	0.62	0.92	0.49	0.68
Pb	49.1	19.2	12.1	34.2	41.6	51.0	150.4	30.8	161.9
Zn	351	228	34.2	11.5	5.3	17.0	10.8	4.0	41.1
Cu	102,986	16,878	37,034	9254	4228	30,877	6772	1294	8249
Cr	14.2	14.3	19.3	20.5	15.4	14.7	16.6	13.8	15.6
Co	8400	296	1366	2885	11,859	9286	6148	15,308	3599
Ni	1055	158	655	1098	5052	3837	1602	5354	886
V	5.0	5.0	15.0	20.3	5.0	6.8	6.8	5.0	5.0
As	5800	950	800	845	330	900	1320	680	1000
Rb	10.0	10.0	10.0	10.0	10.0	10.0	10.0	10.0	10.0
Sr	78.7	203	13.9	26.7	16.8	9.6	25.6	9.4	7.2
Ba	110	240	103	263	83	73	37	69	86
Mn	343	853	302	312	169	62	66	48	66
Nb	0.7	1.7	1.7	2.1	2.1	1.6	2.7	1.6	0.7
Zr	2.0	2.0	23.1	25.2	10.8	26.5	63.2	3.4	40.5
Rb/Sc	25.64	5.41	2.90	2.83	7.52	25.00	38.46	10.10	58.82
Th/Sc	5.13	1.08	0.58	0.57	1.50	6.00	7.69	2.02	27.06
δEu_{PAAS}	1.27	1.71	1.17	1.29	1.15	1.22	0.83	0.72	0.79
δCe_{PAAS}	1.74	1.11	1.04	1.05	1.33	1.06	1.04	1.95	1.08
La/Yb_{PAAS}	0.45	0.48	0.58	0.45	0.46	1.60	1.18	0.26	0.82
La/Sm_{PAAS}	0.21	0.26	0.54	0.49	0.26	0.56	0.75	0.22	0.75
Gd/Lu_{PAAS}	2.55	2.24	1.30	1.34	1.35	1.66	1.19	0.85	0.88
Gd/Yb_{PAAS}	2.80	2.27	1.32	1.32	1.56	1.84	1.22	0.92	1.15
Pr/Sm_{PAAS}	0.35	0.33	0.60	0.57	0.43	0.70	0.79	0.52	0.72
Sm/Yb_{PAAS}	2.08	1.81	1.07	0.92	1.75	2.87	1.58	1.19	1.33
Gd*	1.60	1.37	1.22	1.20	1.18	1.24	1.21	1.18	1.16
Pr*	0.67	0.84	0.90	0.90	0.81	0.93	0.90	0.71	0.90
Y/Ho	43	32	26	27	39	40	29	56	32
∑REE	6.53	19.46	31.64	29.30	9.92	22.51	24.09	6.12	17.74

Appendix A7
Sm–Nd isotopic data for the pyroxene–amphibole-rich rocks, banded or impure dolostones, and quartz itabirites in the Shilu Fe–Co–Cu ore deposit, Hainan Province of South China.

sample	Lithology	Sm (ppm)	Nd (ppm)	$^{147}Sm/^{144}Nd$	$^{143}Nd/^{144}Nd$	$\pm 2\sigma$	$s_{Sm/Nd}$	T_{DM2} (Ga)	$(^{143}Nd/^{144}Nd)_i$	$\varepsilon_{Nd}(0)$	$\varepsilon_{Nd}(t)$
BY034	Pyroxene–amphibole-rich rocks	5.37	24.49	0.1326	0.511934	0.000009	−0.33	2.06	0.511195	−13.4	−6.78
F8-07		4.44	20.21	0.1329	0.511986	0.000009	−0.32	1.98	0.511245	−12.7	−5.79
F9-08		5.63	21.69	0.1570	0.512088	0.000008	−0.20	2.03	0.511213	−10.7	−6.43
SL6-1-2		4.24	23.57	0.1087	0.511902	0.000008	−0.45	1.90	0.511296	−14.4	−4.80
ZSL6-15		3.38	14.85	0.1376	0.512013	0.000007	−0.30	1.98	0.511245	−12.2	−5.79
ZSL6-21-1		5.95	31.77	0.1132	0.511892	0.000009	−0.42	1.96	0.511261	−14.5	−5.48
ZSL6-22		6.00	30.15	0.1204	0.511930	0.000008	−0.39	1.96	0.511259	−13.8	−5.53
ZSL6-7		8.68	30.07	0.1745	0.512125	0.000008	−0.11	2.13	0.511152	−10.0	−7.61
ZSL6-21		5.86	21.56	0.1642	0.512164	0.000007	−0.17	1.98	0.511248	−9.3	−5.73
F8-12	Banded or impure dolostones	1.65	5.04	0.1981	0.512288	0.000014	0.01	2.08	0.511183	−6.8	−7.00
ZSL6-29		0.48	2.38	0.1220	0.511862	0.000013	−0.38	2.08	0.511182	−15.1	−7.02
SL26		0.23	1.10	0.1251	0.511806	0.000017	−0.36	2.20	0.511109	−16.2	−8.46
*Qiongfeng-1	Quartz itabirites	0.25	0.81	0.1831	0.512213	0.000024	−0.07	2.07	0.511192	−8.3	−6.83
*Qiongfeng-2		0.37	1.24	0.1797	0.512196	0.000017	−0.09	2.06	0.511194	−8.6	−6.79
*344-85-14		0.33	0.45	0.4467	0.513695	0.000022	1.27	2.05	0.511205	20.6	−6.58
*Bei88-29		0.54	1.50	0.2172	0.512466	0.000013	0.10	1.97	0.511255	−3.4	−5.60
*Bei88-26		0.15	0.23	0.3910	0.513412	0.000020	0.99	2.00	0.511232	15.1	−6.04
*Bei88-8		0.14	0.34	0.2477	0.512657	0.000053	0.26	1.93	0.511276	0.4	−5.19
*Feng-4		0.60	2.51	0.1477	0.512074	0.000021	−0.25	1.98	0.511251	−11.0	−5.69

Sample with * from Zhang et al. (1992). $(^{143}Nd/^{144}Nd)_i$: initial Nd isotopic composition at 850 Ma.

References

Adekoya, J.A., 1998. The geology and geochemistry of the Maru Banded Iron-Formation, northwestern Nigeria. J. Afr. Earth Sci. 27, 241–257.

Alibert, C., McCulloch, M.T., 1993. Rare earth element and neodymium isotopic compositions of the banded iron-formations and associated shales from Hamersley, Western Australia. Geochim. Cosmochim. Acta 57, 187–204.

Anbar, A.D., 2008. Elements and evolution. Science 322, 1481–1483.

Anbar, A.D., Knoll, A.H., 2002. Proterozoic ocean chemistry and evolution: a bioinorganic bridge. Science 297, 1137–1142.

Annels, A.E., Vaughan, D.J., Craig, J.R., 1983. Conditions of ore mineral formation in certain Zambian copper belt deposits with special reference to the role of cobalt. Miner. Deposita 18, 71–88.

Arora, M., Govil, P.K., Charan, S.N., Uday Raj, B., Manikyamba, C., Chatterjee, A.K., Naqvi, S.M., 1995. Geochemistry and origin of Archean banded iron-formation from the Bababudan schist belt, India. Econ. Geol. 90, 2040–2057.

Babinski, M., Boggiani, P.C., Trindade, R.I.F., Fanning, C.M., 2013. Detrital zircon ages and geochronological constraints on the Neoproterozoic Puga diamictites and associated BIFs in the southern Paraguay Belt, Brazil. Gondwana Res. 23, 988–997.

Banner, J.L., Hanson, G.N., 1990. Calculations of simultaneous isotopic and trace element variations during water rock interaction with application to the carbonate diagenesis. Geochim. Cosmochim. Acta 54, 183–194.

Barovich, K.M., Foden, J., 2000. A Neoproterozoic flood basalt province in southerncentral Australia: geochemical and Nd isotope evidence from basin fill. Precambrian Res. 100, 21–234.

Barrett, T.J., 1981. Chemistry and mineralogy of Jurassic bedded chert overlying ophiolites in the North Apennines, Italy. Chem. Geol. 34, 289–317.

Basta, F.F., Maurice, A.E., Fontboté, L., Favarger, P.Y., 2011. Petrology and geochemistry of the banded iron formation (BIF) of Wadi Karim and Um Anab, Eastern Desert, Egypt: implications for the origin of Neoproterozoic BIF. Precambrian Res. 187, 277–292.

Bau, M., 1991. Rare earth element mobility during hydrothermal and metamorphic fluid–rock interaction and the significance of the oxidation state of europium. Chem. Geol. 93, 219–230.

Bau, M., 1993. Effects of syn-depositional and postdepositional processes on the rare-earth element distribution in Precambrian iron-formations. Eur. J. Mineral. 5, 257–267.

Bau, M., 1999. Scavenging of dissolved yttrium and rare earths by precipitating Fe oxyhydroxide: experimental evidence for Ce oxidation, Y–Ho fractionation, and lanthanide tetrad effect. Geochim. Cosmochim. Acta 63, 67–77.

Bau, M., Dulski, P., 1996. Distribution of yttrium and rare-earth elements in the Penge and Kuruman iron-formations, Transvaal Supergroup, South Africa. Precambrian Res. 79, 37–55.

Bau, M., Dulski, P., 1999. Comparing yttrium and rare earths in hydrothermal fluids from the Mid-Atlantic Ridge: implications for Y and REE behaviour during nearvent mixing and for the Y/Ho ratio of Proterozoic seawater. Chem. Geol. 155, 77–90.

Bau, M., Koschinsky, A., Dulski, P., Hein, J.R., 1996. Comparison of partitioning behaviours of yttrium, rare earth elements, and titanium between hydrogenetic marine ferromanganese crusts and seawater. Geochim. Cosmochim. Acta 60, 1709–1725.

Bekker, A., Slack, J.F., Planavsky, N., Krapež, B., Hofmann, A., Konhauser, K.O., Rouxel, O.J., 2010. Iron formation: the sedimentary product of a complex interplay among mantle, tectonic, oceanic, and biospheric processes. Econ. Geol. 105, 467–508.

Beukes, N.J., Gutzmer, J., 2008. Chapter I. Origin and paleoenvironmental significance of major iron formations at the Archean–Paleoproterozoic boundary. Rev. Econ. Geol. 15, 5–47.

Beukes, N.J., Gutzmer, J., Mukhopadhyay, J., 2003. The geology and genesis of high-grade hematite iron ore deposits. Appl. Earth Sci. 112, 18–25.

Beukes, N.J., Mukhopadhyay, J., Gutzmer, J., 2008. Genesis of high-grade iron ores of the Archean Iron Ore Group around Noamundi, India. Econ. Geol. 103, 365–386.

Bolhar, R., Van Kranendonk, M.J., 2007. A non-marine depositional setting for the northern Fortescue Group, Pilbara Craton, inferred from trace element geochemistry of stromatolitic carbonates. Precambrian Res. 155, 229–250.

Bolhar, R., Kamber, B.S., Moorbath, S., Fedo, C.M., Whitehouse, M.J., 2004. Characterisation of early Archaean chemical sediments by trace element signatures. Earth Planet. Sci. Lett. 222, 43–60.

Bonatti, E., Fisher, D.E., Joensuu, O., Rydell, H.S., Beyth, M., 1972. Iron–manganese–barium deposit from the Northern Afar Rift (Ethiopia). Econ. Geol. 67, 717–730.

Boström, K., 1973. Origin and fate of ferromanganoan active ridge sediments. Stockh. Contrib. Geol. 27 (2), 147–243.

Candela, P.A., Wylie, A.G., Burke, T.M., 1989. Genesis of the ultramafic rock-associated Fe–Cu–Co–Zn–Ni deposits of the Sykesville district, Maryland Piedmont. Econ. Geol. 84, 663–675.

Canfield, D.E., 1998. A new model for Proterozoic ocean chemistry. Nature 396, 450–453.

Caron, V., Ekomane, E., Mahieux, G., Moussango, P., Ndjeng, E., 2010. The Mintom Formation (new): sedimentology and geochemistry of a Neoproterozoic, Paralic succession in south-east Cameroon. J. Afr. Earth Sci. 57, 367–385.

Condie, K.C., 1993. Chemical composition and evolution of the upper continental crust: contrasting results from surface samples and shales. Chem. Geol. 104, 1–37.

Derry, L.A., Jacobsen, S.B., 1988. The Nd and Sr isotopic evolution of Proterozoic seawater. Geophys. Res. Lett. 15, 397–400.

Derry, L.A., Jacobsen, S.B., 1990. The chemical evolution of Precambrian seawater: evidence from REEs in banded iron formations. Geochim. Cosmochim. Acta 54, 2965–2977.

Dorr II, J.V.N., 1969. Physiographic, stratigraphic and structural development of the Quadrilátro Ferrfero, Minas Gerais, Brazil. USGS Prof. Paper, Washington, 641-A. (A1–A103 pp.).

Dymek, R.F., Klein, C., 1988. Chemistry, petrology and origin of banded iron-formation lithologies from the 3800 Ma Isua supracrustal belt, West Greenland. Precambrian Res. 39, 247–302.

El Desouky, H.A., Muchez, Ph., Cailteux, J., 2009. Two Cu–Co sulfide phases and contrasting fluid systems in the Katanga Copperbelt, Democratic Republic of Congo. Ore Geol. Rev. 36, 315–332.

El Desouky, H.A., Muchez, P., Boyce, A.J., Schneider, J., Cailteux, J.L.H., Dewaele, S., von Quadt, A., 2010. Genesis of sediment-hosted stratiform copper–cobalt mineralization at Luiswishi and Kamoto, Katanga Copperbelt (Democratic Republic of Congo). Miner. Deposita 45, 735–763.

Elderfield, H., Upstillgoddard, R., Sholkovitz, E.R., 1990. The rare-earth elements in rivers, estuaries, and coastal seas and their significance to the composition of ocean waters. Geochim. Cosmochim. Acta 54, 971–991.

Ewers, W.E., Morris, R.C., 1981. Studies on the Dales Gorge member of Brockman iron formation. Econ. Geol. 76, 1929–1953.

Eyles, N., Januszczak, N., 2004. 'Zipper-rift': a tectonic model for Neoproterozoic glaciations during the breakup of Rodinia after 750 Ma. Earth Sci. Rev. 65, 1–73.

Fang, Z., Zhao, J.X., McCulloch, M.T., 1992. Geochemical and Nd isotopic study of Paleozoic bimodal volcanics in Hainan Island, South China — implications of rifting tectonics and mantle reservoirs. Lithos 29, 127–139.

Feng, C.Y., Zhang, D.Q., Dang, X.Y., 2004. Cobalt resources of China and their exploitation and utilization. Miner. Depos. 23, 93–100 (in Chinese with English abstract).

Frei, R., Polat, A., 2007. Source heterogeneity for the major components of 3.7 Ga Banded Iron Formations (Isua Greenstone Belt, Western Greenland): tracing the nature of interacting water masses in BIF formation. Earth Planet. Sci. Lett. 253, 266–281.

Frei, R., Dahl, P.S., Duke, E.F., Frei, K.M., Hansen, T.R., Frandsson, M.M., Jensen, L.A., 2008. Trace element and isotopic characterization of Neoarchean and Paleoproterozoic iron formations in the Black Hills (South Dakota, USA): assessment of chemical change during 2.9–1.9 Ga deposition bracketing the 2.4–2.2 Ga first rise of atmospheric oxygen. Precambrian Res. 162, 441–474.

Freitas, B.T., Warren, L.V., Boggiani, P.C., De Almeida, R.P., Piacentini, T., 2011. Tectonosedimentary evolution of the Neoproterozoic BIF-bearing Jacadigo Group, SW-Brazil. Sediment. Geol. 238, 48–70.

Frimmel, H.E., 2009. Trace element distribution in Neoproterozoic carbonates as palaeoenvironmental indicator. Chem. Geol. 258, 338–353.

Fryer, B.J., 1977. Trace element geochemistry of the Sokoman Iron Formation. Can. J. Earth Sci. 14, 1598–1610.

German, C.R., Holliday, B.P., Elderfield, H., 1991. Redox cycling of rare earth elements in the suboxic zone of the Black Sea. Geochim. Cosmochim. Acta 55, 3553–3558.

Gnaneshwar Rao, T., Naqvi, S.M., 1995. Geochemistry, depositional environment and tectonic setting of the BIF's of the Late Archaean Chitradurga Schist Belt, India. Chem. Geol. 121, 217–243.

Graham, G., Hitzman, M.W., Zieg, J., 2012. Geologic setting, sedimentary architecture, and paragenesis of the Mesoproterozoic sediment-hosted Sheep Creek Cu–Co–Ag deposit, Helena Embayment, Montana. Econ. Geol. 107, 1115–1141.

Gross, G.A., 1980. A classification of iron formations based on depositional environments. Can. Mineral. 18, 215–222.

Gross, G.A., 1991. Genetic concepts for iron-formation and associated metalliferous sediments. Ecol. Monogr. 8, 51–81.

Gutzmer, J., Beukes, N.J., 1998. The manganese formation of the Neoproterozoic Penganga Group, India — revision of an enigma. Econ. Geol. 93, 1091–1102.

Halverson, G.P., Wade, B.P., Hurtgen, M.T., Barovich, K.M., 2010. Neoproterozoic chemostratigraphy. Precambrian Res. 182, 337–350.

Halverson, G.P., Poitrasson, F., Hoffman, P.F., Nédélec, A., Montel, J.-M., Kirby, J., 2011. Fe isotope and trace element geochemistry of the Neoproterozoic syn-glacial Rapitan iron formation. Earth Planet. Sci. Lett. 309, 100–112.

Hamade, T., Konhauser, K.O., Raiswell, R., Goldsmith, S., Morris, R.C., 2003. Using Ge/Si ratios to decouple iron and silica fluxes in Precambrian banded iron formations. Geology 31, 35–38.

HBGMR (Hainan Bureau of Geology and Mineral Resources), 1997. Lithostratigraphy of Hainan Province. Chinese University of Geosciences Press, Wuhan 125 (in Chinese).

Hoffman, P.F., Schrag, D.P., 2002. The snowball Earth hypothesis: testing the limits of global change. Terra Nova 14, 129–155.

Hoffman, P.F., Kaufman, A.J., Halverson, G.P., Schrag, D.P., 1998. A Neoproterozoic snowball Earth. Science 281, 1342–1346.

Holland, H.D., 1973. The oceans, a possible source of iron-formations. Econ. Geol. 68, 1169–1172.

Hong, J.L., Wang, J.C., He, S.M., 1981. Mineralogical genesis of Shilu iron ores. Acta Mineral. Sin. 2 (3), 145–152 (in Chinese with English abstract).

Horstmann, U.E., Hälbich, I.W., 1995. Chemical composition of banded iron-formations of the Griqualand West Sequence, Northern Cape Province, South Africa, in comparison with other Precambrian iron formations. Precambrian Res. 72, 109–145.

Huang, J., Chu, X.L., Jiang, G.Q., Feng, L.J., Chang, H.J., 2011. Hydrothermal origin of elevated iron, manganese and redox-sensitive trace elements in the c. 635 Ma Doushantuo cap carbonate. J. Geol. Soc. Lond. 168, 805–815.

Hurtgen, M.T., Arthur, M.A., Suits, N.S., Kaufman, A.J., 2002. The sulfur isotopic composition of Neoproterozoic seawater sulfate: implications for a snowball Earth? Earth Planet. Sci. Lett. 203 (1), 413–429.

Huston, D.L., Logan, G.A., 2004. Barite, BIFs and bugs: evidence for the evolution of the Earth's early hydrosphere. Earth Planet. Sci. Lett. 220, 41–55.

Huston, D.L., Pehrsson, S., Eglington, B.M., Zaw, K., 2010. The geology and metallogeny of volcanic-hosted massive sulfide deposits: variations through geologic time and with tectonic setting. Econ. Geol. 105, 571–591.

Ilyin, A.V., 2009. Neoproterozoic banded iron formations. Lithol. Miner. Resour. 44, 78–86.

Isley, A.E., Abbott, D.H., 1999. Plume-related mafic volcanism and the deposition of banded iron formation. J. Geophys. Res. 104, 15461–15477.

Jacobsen, S.B., Pimentel-Klose, M.R., 1988a. Nd isotopic variations in Precambrian banded iron formations. Geophys. Res. Lett. 15, 393–396.

Jacobsen, S.B., Pimentel-Klose, M.R., 1988b. A neodymium isotopic study of the Hamersley and Michipicoten banded iron-formations: the source of REE and iron in Archean oceans. Earth Planet. Sci. Lett. 87, 29–44.
James, H.L., 1954. Sedimentary facies of iron-formations. Econ. Geol. 49, 235–293.
James, H.L., 1992. Precambrian iron-formations: nature, origin, and mineralogic evolution from sedimentation to metamorphism. In: Wolf, K.H., Chilingarian, G.V. (Eds.), Diagensis III. Developments in Sedimentology, 47, pp. 543–589.
James, H.L., Sims, P.K., 1973. Precambrian iron-formations of the world: introduction. Econ. Geol. 68, 913–914.
Johannesson, K.H., Zhou, X.P., 1999. Origin of middle rare earth element enrichments in acid waters of a Canadian High Arctic lake. Geochim. Cosmochim. Acta 63 (1), 153–165.
Johnston, D.T., Poulton, S.W., Dehler, C., Porter, S., Husson, J., Canfield, D.E., Knoll, A.H., 2010. An emerging picture of Neoproterozoic ocean chemistry: insights from the Chuar Group, Grand Canyon, USA. Earth Planet. Sci. Lett. 290, 64–73.
Kato, Y., Kawakami, T., Kano, T., Kunugiza, K., Swamy, N.S., 1996. Rare-earth element geochemistry of banded Fe formations and associated amphibolite from the Sargur belts, south India. J. SE Asian Earth Sci. 14, 161–164.
Khalil, K.I., El-Shazly, A.K., 2012. Petrological and geochemical characteristics of Egyptian banded iron formations: review and new data from Wadi Kareim. Geochemistry 12, 105–126.
Kimberley, M.M., 1989. Exhalative origins of iron formations. Ore Geol. Rev. 5, 13–145.
Kirschvink, J., 1992. Late Proterozoic low-latitude global glaciation: the Snowball Earth. In: Schopf, J.W., Klein, C. (Eds.), The Proterozoic Biosphere. Cambridge University Press, pp. 51–52.
Klein, C., 2005. Some Precambrian banded iron-formations (BIFs) from around the world: their age, geologic setting, mineralogy, metamorphism, geochemistry, and origin. Am. Mineral. 90 (10), 1473–1499.
Klein, C., Beukes, N.J., 1993. Sedimentology and geochemistry of the glaciogenic late Proterozoic Rapitan Iron-Formation in Canada. Econ. Geol. 88 (3), 542–565.
Klein, C., Ladeira, E.A., 2000. Geochemistry and petrology of some Proterozoic banded iron-formations of the Quadrilátero Ferrífero, Minas Gerais, Brazil. Econ. Geol. 95 (2), 405–427.
Klein, C., Ladeira, E.A., 2004. Geochemistry and mineralogy of Neoproterozoic banded iron-formations and some selected, siliceous manganese formations from the Urucum district, Mato Grosso do Sul, Brazil. Econ. Geol. 99 (6), 1233–1244.
Klemm, D.D., 2000. The formation of Paleoproterozoic banded iron formations and their associated Fe and Mn deposits, with reference to the Griqualand West deposits, South Africa. J. Afr. Earth Sci. 30, 1–24.
Krapež, B., Barley, M.E., Pickard, A.L., 2003. Hydrothermal and resedimented origins of the precursor sediments to banded iron formation: sedimentological evidence from the Early Palaeoproterozoic Brockman Supersequence of Western Australia. Sedimentology 50, 979–1011.
Lascelles, D.F., 2007. Black smokers and density currents: a uniformitarian model for the genesis of banded iron-formations. Ore Geol. Rev. 32, 381–411.
Le Heron, D.P., Busfield, M.E., Le Ber, E., Kamona, A.F., 2013. Neoproterozoic ironstones in northern Namibia: biogenic precipitation and Cryogenian glaciation. Palaeo 369, 48–57.
Li, X.H., McCulloch, M.T., 1996. Secular variation in the Nd isotopic composition of Neoproterozoic sediments from the southern margin of the Yangtze Block: evidence for a Proterozoic continental collision in southeast China. Precambrian Res. 76, 67–76.
Li, Z.X., Li, X.H., Kinny, P.D., Wang, J., 1999. The breakup of Rodinia: did it start with a mantle plume beneath South China? Earth Planet. Sci. Lett. 173, 171–181.
Li, X.H., Li, Z.X., Zhou, H., Liu, Y., Kinny, P.D., 2002a. U–Pb zircon geochronology, geochemistry and Nd isotopic study of Neoproterozoic bimodal volcanic rocks in the Kangdian Rift of South China: implications for the initial rifting of Rodinia. Precambrian Res. 113, 135–154.
Li, X.H., Zhou, H.W., Ding, S.J., Chung, S.L., Liu, Y., Lee, C.Y., Ge, W.C., Zhang, Y.M., Zhang, R.J., 2002b. Geochemical and Sm–Nd isotopic characteristics of metabasites from central Hainan Island, South China and their tectonic significance. Island Arc 11 (3), 193–205.
Li, Z.X., Li, X.-H., Zhou, H.W., Kinny, P.D., 2002c. Grenvillian continental collision in south China: new SHRIMP U–Pb zircon results and implications for the configuration of Rodinia. Geology 30, 163–166.
Li, Z.X., Li, X.H., Kinny, P.D., Wang, J., Zhang, S., Zhou, H., 2003. Geochronology of Neoproterozoic syn-rift magmatism in the Yangtze Craton, South China and correlations with other continents: evidence for a mantle superplume that broke up Rodinia. Precambrian Res. 122, 85–109.
Li, X.H., Li, Z.X., Li, W.X., Wang, Y.J., 2006a. Initiation of the Indosinian orogeny in South China: evidence for a Permian magmatic arc on Hainan Island. J. Geol. 114, 341–353.
Li, X.H., Li, Z.X., Wingate, M.T.D., Chung, S.L., Liu, Y., Lin, G.C., Li, W.X., 2006b. Geochemistry of the 755 Ma Mundine Well dyke swarm, northwestern Australia: part of a Neoproterozoic mantle superplume beneath Rodinia? Precambrian Res. 146 (1–2), 1–15.
Li, Z.X., Li, X.H., Li, W.X., Ding, S.J., 2008. Was Cathaysia part of Proterozoic Laurentia? New data from Hainan Island, south China. Terra Nova 20 (2), 154–164.
Li, W.X., Li, X.H., Li, Z.X., 2010. Ca. 850 Ma bimodal volcanic rocks in northeastern Jiangxi Province, South China: initial extension during the breakup of Rodinia? Am. J. Sci. 310, 951–980.
Ling, H.F., Feng, H.Z., Pan, J.Y., Jiang, S.Y., Chen, Y.Q., Chen, X., 2007. Carbon isotope variation through the Neoproterozoic Doushantuo and Dengying Formations, South China: implications for chemostratigraphy and paleoenvironmental change. Palaeo 254, 158–174.
Lottermoser, B.G., Ashley, P.M., 2000. Geochemistry, petrology and origin of Neoproterozoic ironstones in the eastern part of the Adelaide Geosyncline, South Australia. Precambrian Res. 101, 49–67.
Lu, G.X., 1988. New discovery of volcanic rocks in ore-bearing rock series in the Shilu iron deposit on Hainan Island. Reg. Geol. China 15 (1), 53–56 (in Chinese with English abstract).
Ma, D.Q., Wang, X.D., Chen, Z.P., Xiao, Z.F., Zhang, W.C., Zhong, S.Z., 1997. New achievements on Baoban Group in Hainan Island. Reg. Geol. China 16 (2), 130–136 (in Chinese with English abstract).
Manikyamba, C., Balaram, V., Naqvi, S.M., 1993. Geochemical signatures of polygenetic origin of the banded iron formation (BIF) of Archean Sandur greenstone belt (schist belt), Karnataka nucleus, India. Precambrian Res. 61, 137–164.
Maynard, J.B., Okita, P.M., 1991. Bedded barite deposits in the United States, Canada, Germany, and China: two major types based on tectonic setting. Econ. Geol. 86, 364–376.
McLennan, S.M., Taylor, S.R., McCulloch, M.T., Maynard, J.B., 1990. Geochemical and Nd–Sr isotopic composition of deep-sea turbidites: crustal evolution and plate tectonic associations. Geochim. Cosmochim. Acta 54, 2015–2050.
McLennan, S.M., Hemming, S., McDanniel, D.K., Hanson, G.N., 1993. Geochemical approaches to sedimentation, provenance, and tectonics. In: Johnsson, M.J., Basu, A. (Eds.), Processes Controlling the Composition of Clastic Sediments. Geological Society of American Special Paper, 284, pp. 21–40.
McLennan, S.M., Hemming, S.R., Taylor, S.R., Eriksson, K.A., 1995. Early Proterozoic crustal evolution: geochemical and Nd–Pb isotopic evidences from metasedimentary rocks, southwestern North America. Geochim. Cosmochim. Acta 59, 1153–1177.
Metcalfe, I., Shergold, I.H., Li, Z.X., 1994. IGCP 321 Gondwana dispersion and Asian accretion: field-work on Hainan Island. Episodes 16 (4), 443–447.
Miller, R.G., O'Nions, R.K., 1985. Source of Precambrian chemical and clastic sediments. Nature 314, 325–330.
Morris, R.C., Horwitz, R.C., 1983. The origin of the iron formation rich Hamersely Group of Western Australia—deposition on a platform. Precambrian Res. 21, 273–297.
Mukherjee, S.K., 2008. Petrography, Age (U–Pb Zircon), Geochemical and Isotopic Studies of the Sawawin Banded Iron-formation (BIF), Northwestern Saudi Arabia: Implications for Understanding Neoproterozoic Climate Change. Ph.D. dissertation University of Texas at Dallas (137 pp.).
Nijman, W., de Bruijne, K., Valkering, M.E., 1998. Growth fault control of Early Archaean cherts, barite mounds and chert–barite veins, North Pole Dome, Eastern Pilbara, Western Australia. Precambrian Res. 88, 25–52.
Nold, J.L., 1990. The Idaho cobalt belt, northwestern United States—a metamorphosed Proterozoic exhalative ore district. Miner. Deposita 25 (3), 163–168.
Nozaki, Y., Zhang, J., Amakawa, H., 1997. The fractionation between Y and Ho in the marine environment. Earth Planet. Sci. Lett. 148, 329–340.
Och, L.M., Shields-Zhou, G.A., 2012. The Neoproterozoic oxygenation event: environmental perturbations and biogeochemical cycling. Earth Sci. Rev. 110, 26–57.
Pan, Y.M., Therens, C., 2000. The Werner Lake Co–Cu–Au deposit of the English River subprovince, Ontario, Canada: evidence for an exhalative origin and effects of granulite facies metamorphism. Econ. Geol. 95, 1635–1656.
Pecoits, E., Gingras, M., Aubet, N., Konhauser, K., 2008. Ediacaran in Uruguay: palaeoclimatic and palaeobiological implications. Sedimentology 55, 689–719.
Pecoits, E., Gingras, M.K., Barley, M.E., Kappler, A., Posth, N.R., Konhauser, K.O., 2009. Petrography and geochemistry of the Dales Gorge banded iron formation: paragenetic sequence, source and implications for palaeo-ocean chemistry. Precambrian Res. 172 (1–2), 163–187.
Peltola, E., 1977. Origin of Precambrian copper sulfides of the Outokumpu district, Finland. Econ. Geol. 73, 461–477.
Pickard, A.L., Barley, M.E., Krapež, B., 2004. Deep-marine depositional setting of banded iron formation: sedimentological evidence from interbedded clastic sedimentary rocks in the early Palaeoproterozoic Dales Gorge Member of Western Australia. Sediment. Geol. 170, 37–62.
Pirajno, F., Hocking, R.M., Reddy, S.M., Jones, A.J., 2009. A review of the geology and geodynamic evolution of the Palaeoproterozoic Earaheedy Basin, Western Australia. Earth Sci. Rev. 94, 39–77.
Planavsky, N., Bekker, A., Rouxel, O.J., Kamber, B., Hofmann, A., Knudsen, A., Lyons, T.W., 2010. Rare Earth Element and yttrium compositions of Archean and Paleoproterozoic Fe formations revisited: new perspectives on the significance and mechanisms of deposition. Geochim. Cosmochim. Acta 74, 6387–6405.
Planavsky, N.J., McGoldrick, P., Scott, C.T., Li, C., Reinhard, C.T., Kelly, A.E., Chu, X.L., Bekker, A., Love, G.D., Lyons, T.W., 2011. Widespread iron-rich conditions in the mid-Proterozoic ocean. Nature 477, 447–451.
Poole, F.G., 1988. Stratiform barite in Paleozoic rocks of the western United States. In: Zachrisson, E. (Ed.), Proceedings of the Seventh Quadrennial IAGOD Symposium. E. Schweizerbar'sche Verlagsbuchhandlung, Stuttgart, Germany, pp. 309–319.
Purohit, R., Papineau, D., Kröner, A., Sharma, K.K., Roy, A.B., 2012. Carbon isotope geochemistry and geochronological constraints of the Neoproterozoic Sirohi Group from northwest India. Precambrian Res. 220–221, 80–90.
Rasmussen, B., Fletcher, I.R., Bekker, A., Muhling, J.R., Gregory, C.J., Thorne, A.M., 2012. Deposition of 1.88-billion-year-old iron formations as a consequence of rapid crustal growth. Nature 484, 498–501.
Rudnick, R.L., Gao, S., 2003. Composition of the continental crust. In: Heinrich, D.H., Karl, K.T. (Eds.), The Crust. Treatise on Geochemistry, vol. 3. Elsevier, p. 64.
SCISTCAS (South China Iron-rich Scientific Team, Chinese Academy of Sciences), 1986. Geology and Geochemistry of the Shilu Fe Ore Deposit in Hainan Island. Science Press, Beijing 376 (in Chinese).
Selley, D., Broughton, D., Scott, R., Hitzman, M., Bull, S., Large, R., McGoldrick, P., Croaker, M., Pollington, N., Barra, F., 2005. A new look at the geology of the Zambian Copperbelt. Econ. Geol. 965–1000 (100th Anniversary Volume).
Shu, L.S., Faure, M., Yu, J.H., Jahn, B.-M., 2011. Geochronological and geochemical features of the Cathaysia block (South China): new evidence for the Neoproterozoic breakup of Rodinia. Precambrian Res. 187, 263–276.
Simonson, B.M., 1985. Sedimentological constraints on the origins of Precambrian iron-formations. Geol. Soc. Am. Bull. 96, 244–252.
Slack, J.F., Grenne, T., Bekker, A., Rouxel, O.J., Lindberg, P.A., 2007. Suboxic deep seawater in the late Paleoproterozoic: evidence from hematitic chert and Fe formation related

to seafloor-hydrothermal sulfide deposits, central Arizona, USA. Earth Planet. Sci. Lett. 255, 243–256.
Spier, C.A., de Oliveira, S.M.B., Rosière, C.A., 2003. Geology and geochemistry of the Águas Claras Quadrilátero Ferrífero, Minas Gerais, Brazil. Miner. Deposita 38, 751–774.
Spier, C.A., de Oliveira, S.M.B., Sial, A.N., Rios, F.J., 2007. Geochemistry and genesis of the banded iron formations of the Cauê Formation, Quadrilátero Ferrífero, Minas Gerais, Brazil. Precambrian Res. 152, 170–206.
Stern, R.J., Avigad, D., Miller, N.R., Beyth, M., 2006. Evidence for the snowball Earth hypothesis in the Arabian–Nubian Shield and the East African Orogen. J. Afr. Earth Sci. 44, 1–20.
Sun, S.-S., McDonugh, W.F., 1989. Chemical and isotopic systematics of oceanic basalt: implication for mantle composition and processes. In: Saunders, A.D., Norry, M.J. (Eds.), Magmatism in the Ocean Basins. Geological Society of Special Publication, 42, pp. 528–548.
Sun, H., Wu, J., Yu, P., Li, J., 1998. Geology, geochemistry and sulfur isotope composition of the Late Proterozoic Jingtieshan (Superior-type) hematite–jasper–barite iron ore deposits associated with stratabound Cu mineralization in the Gansu Province, China. Miner. Deposita 34 (1), 102–112.
Sweeney, M., Turner, P., Vaughan, D.J., 1986. Stable isotope and geochemical studies of the role of early diagenesis in ore formation, Konkola basin, Zambian Copper Belt. Econ. Geol. 81, 1838–1852.
Tang, J.F., Fu, H.Q., Yu, Z.Q., 1987. The stratigraphic horizon, type, and formation condition of Precambrian siliceous iron formation in south China. Ore Geol. 6, 1–10 (in Chinese).
Tapponnier, P., Lacassin, R., Leloup, P.H., Sharer, U., Zhong, D.L., Liu, X.C., Ji, S.C., Zhang, L.S., Zhong, J.Y., 1990. The Ailao Shan–Red River metamorphic belt: tertiary left-lateral shear between Indochina and south China. Nature 343, 431–437.
Taylor, S.R., McLennan, S.M., 1985. The Continental Crust: Its Composition and Evolution. Blackwell, Oxford 312.
Torres-Ruiz, J., 2006. Geochemical constraints on the genesis of the Marquesado iron ore deposits, Betic Cordillera, Spain: REE, C, O, and Sr isotope data. Econ. Geol. 101, 667–677.
Toth, J.R., 1980. Deposition of submarine crusts rich in manganese and iron. Geol. Soc. Am. Bull. 91, 44–54.
Trendall, A.F., 1983. Introduction. In: Trendall, A.F., Morris, R.C. (Eds.), Iron-Formation: Facts and Problems. Elsevier, Amsterdam, pp. 1–11.
Trendall, A.F., 2002. The significance of iron-formation in the Precambrian stratigraphic record. Int. Assoc. Sedimentol. Spec. Publ. 33, 33–66.
Veríssimo, C.U.V., Schrank, A., Pires, F.R.M., Hasui, Y., Zanardo, A., Parente, C.V., 2002. Geochemical Study of the Itabirite Iron Ores of the Alegria Mine—Quadrilátero Ferrífero, Minas Gerais, Brazil, Iron Ore 2002. Australasian Institute of Mining and Metallurgy, Perth 95–103.
Wang, H.Z., 1985. The research of quartz in Shilu iron deposits of Hainan Island and its significance. Earth Sci. 10 (2), 77–83 (in Chinese with English abstract).
Wang, H.Z., 1986. Chapter 5, the Proterozoic; Chapter 6, the Sinian system. In: Yang, Z.Y., Chen, Y.Q., Wang, H.Z. (Eds.), The Geology of China. Clarendon Press, Oxford, pp. 31–63.
Wang, J., Li, Z.X., 2003. History of Neoproterozoic rift basins in South China: implications for Rodinia break-up. Precambrian Res. 122 (1–4), 141–158.
Wang, J.C., Hong, J.L., He, S.M., 1978. Studies on genesis of diopside–hedenbergite series in the Shilu Fe ore deposit, Hainan Island. Miner. Depos. (Z1), 59–70 (in Chinese).
Wang, X.F., Ma, D.Q., Jiang, D.H. (Eds.), 1991. Geology of Hainan Island: the 1st, Stratum and Paleo-biology. Geology Publishing House, Beijing, pp. 7–32 (in Chinese).
Wang, Y.J., Fan, W.M., Zhang, G.W., Zhang, Y.H., 2013. Phanerozoic tectonics of the South China Block: key observations and controversies. Gondwana Res. 23, 1273–1305.
Webb, A.D., Dickens, G.R., Oliver, N.H.S., 2003. From banded iron-formation to iron ore: geochemical and mineralogical constraints from across the Hamersley Province, Western Australia. Chem. Geol. 197, 215–251.
Wonder, J.D., Spry, P.G., Windom, K.E., 1988. Geochemistry and origin of manganese-rich rocks related to iron-formation and sulfide deposits, western Georgia. Econ. Geol. 83, 1070–1081.
Xu, D.R., Fan, W.M., Liang, X.Q., Tang, H.F., 2001a. Characteristics of Proterozoic metamorphic basement in Hainan Island and its implications for crustal growth: Nd and Pb isotope constraints. Geol. J. China Univ. 7 (2), 146–157 (in Chinese with English abstract).
Xu, D.R., Lin, G., Liang, X.Q., Chen, G.H., Tang, H.F., 2001b. The records of the evolution of Precambrian lithosphere: the evidences of petrology and geochemistry of basic locks on Hainan Island. Acta Petrol. Sin. 17 (4), 598–608 (in Chinese with English abstract).
Xu, D.R., Ma, C., Li, P.C., Xia, B., Zhang, Y.Q., 2007a. U–Pb SHRIMP-dating of zircon domains from metaclastic sedimentary rocks in Hainan Island, South China, and its geological significance. Acta Geol. Sin. 81, 383–391 (in Chinese with English abstract).
Xu, D.R., Xia, B., Li, P.C., Chen, G.H., Ma, C., Zhang, Y.Q., 2007b. Protolith natures and U–Pb sensitive high mass-resolution ion microprobe (SHRIMP) zircon ages of the metabasites in Hainan Island, South China: implications for geodynamic evolution since the late Precambrian. Island Arc 16, 575–597.
Xu, D.R., Xiao, Y., Xia, B., Cai, R.J., Hou, W., Wang, L., Liu, Z.L., Zhao, B., 2009. Metallogenic Model and Ore Predicating of the Shilu Iron Ore Deposit in Hainan Province, China. Geology Publishing House, Beijing 331 (in Chinese).
Xu, D.R., Wang, Z.L., Cai, J.X., Wu, C.J., Bakun-Czubarow, N., Wang, L., Chen, H.Y., Baker, M.J., Kusiak, M.A., 2013. Geological characteristics and metallogenesis of the Shilu Fe-ore deposit in Hainan Province, South China. Ore Geol. Rev. 53, 318–342.
Yao, H.Z., Sheng, X.C., Zhang, R.J., 1999. Neoproterozoic sedimentary environment of Shilu area, Hainan Island, South China. Gondwana Res. 2, 563–566.
Yeo, G.M., 1981. The Late Proterozoic Rapitan glaciation in the northern Cordillera. In: Campbell, F.H.A. (Ed.), Proterozoic Basins of Canada. Geol. Surv. Can, Paper 81-10, pp. 25–46.
Young, G.M., 2002. Stratigraphic and tectonic settings of Proterozoic glaciogenic rocks and banded iron-formations: relevance to the snowball Earth debate. J. Afr. Earth Sci. 35, 451–466.
Yu, C.M., Lu, H.Z., 1983. An investigation into the genesis of the Shilu iron deposit with special reference to its fluid inclusions. Geochemistry 2 (2), 127–141.
Zeng, Q., Yuan, C., Guo, Z., Lin, J., Wu, W., Cai, D., Zhuang, S., Huang, H., Fu, C., Wu, T., Wang, W., Yun, P., 1992. Fundamental Geological Investigation of Sanya, Hainan Island. The Press of the China University of Geosciences, Wuhan (174 pp., in Chinese with English abstract).
Zhang, R.J., Ma, G.G., Hong, S.N., Yan, D.P., 1992. The Sm–Nd isotopic age of Shilu iron ore in Hainan Island and its implications. Sci. Geol. Sin. 21 (1), 38–43 (in Chinese with English abstract).
Zhang, Y.M., Zhang, R.J., Yao, H.Z., Ma, G.G., 1997. The Precambrian crustal tectonic evolution in Hainan Island. Earth Sci. J. China Univ. Geosci. 22 (4), 395–400 (in Chinese with English abstract).
Zhang, Q.R., Chu, X.L., Feng, L.J., 2011. Neoproterozoic glacial records in the Yangtze Region, China. In: Arnaud, E., Halverson, G.P., Shields-Zhou, G. (Eds.), The Geological Record of Neoproterozoic Glaciations. Geological Society, London, Memoirs, 36, pp. 357–366.
Zhao, J.S., Xia, B., Qiu, X.L., Zhao, B., Xu, D.R., Feng, Z.H., Li, Z.L., Shen, G.F., Hu, R.Z., Su, W.C., Qin, C.J., Qin, W.M., Fu, X., Hu, Z.G., 2008. Finding of melt inclusion in garnet from skarn of Shilu iron deposit, Hainan province. Acta Petrol. Sin. 24, 149–160 (in Chinese with English abstract).